A Nonequilibrium Finite-Rate Carbon Ablation Model For Radiating Earth Re-entry Flows

DISSERTATION

Christopher R. Alba, Captain, USAF

AFIT-ENY-DS-15-S-053

DEPARTMENT OF THE AIR FORCE
AIR UNIVERSITY

AIR FORCE INSTITUTE OF TECHNOLOGY

Wright-Patterson Air Force Base, Ohio

DISTRIBUTION STATEMENT A:

APPROVED FOR PUBLIC RELEASE; DISTRIBUTION UNLIMITED

AFIT-ENY-DS-15-S-053

A NONEQUILIBRIUM FINITE-RATE CARBON ABLATION MODEL FOR RADIATING
EARTH RE-ENTRY FLOWS

DISSERTATION

Presented to the Faculty

Graduate School of Engineering and Management

Air Force Institute of Technology

Air University

Air Education and Training Command

in Partial Fulfillment of the Requirements for the

Degree of Doctor of Philosophy

Christopher R. Alba, B.S., M.S.

Captain, USAF

September 2015

DISTRIBUTION STATEMENT A:

APPROVED FOR PUBLIC RELEASE; DISTRIBUTION UNLIMITED

AFIT-ENY-DS-15-S-053

A Nonequilibrium Finite-Rate Carbon Ablation Model For Radiating
Earth Re-entry Flows

Christopher R. Alba, B.S., M.S.
Captain, USAF

Committee Membership:

Robert B. Greendyke, Ph.D.
Chairman

Capt Brook I. Bentley, Ph.D.
Member

William F. Bailey, Ph.D.
Member

Graham V. Candler, Ph.D.
Member

ADEDEJI B. BADIRU, Ph.D.
Dean, Graduate School of Engineering
and Management

AFIT-ENY-DS-15-S-053

Abstract

Vehicles entering planetary atmospheres at high speed require an ablative heat shield in order to withstand the high thermal energy flux to the body. The interaction between the ablative products and the flow field is not well characterized. Numerical simulations were conducted to investigate the influence of carbon ablation on shock layer radiation. Data collected from experiments performed in the X-2 expansion tunnel at the University of Queensland was used to compare to the simulations. The model was a short half-cylinder made of isomolded graphite and was tested in 8.6 km/s Earth entry flow. The model surface was heated within a temperature range of 1770-3280 K. The radiation emitted from the CN violet bands was measured by ultraviolet spectrometry in a spectral range from 353-391 nm. This research develops a novel finite-rate surface kinetic model for determining the chemical state of an ablating boundary layer. The proposed ablation model accounts for competing surface reaction processes such as adsorption/desorption, Eley-Rideal mechanisms, oxidation, nitridation, and sublimation. The included oxidation mechanisms predict CO as the primary oxidized product at the considered surface temperatures, which is in agreement with experiment and theory. A previous model had incorrectly predicted CO_2 as the primary oxidized product for a majority of the tested surface temperatures. The ablative gas species predicted by this new surface model results in better agreement with experimental spectral measurements than predictions provided by legacy ablation models, and represents a significant improvement in current modeling capabilities for hypersonic nonequilibrium ablating re-entry flows.

To my wife,

for her unending love and support.

To my three sons,

who provide joy and happiness to my life everyday.

Acknowledgements

This dissertation was made possible with the help of many people. I would like to thank my family and friends who provided encouragement and support while I was working on my degree. I am grateful to my research advisor, Dr. Robert Greendyke, for his support and guidance throughout my time at AFIT. Thank you for giving me space to explore different research paths and providing timely direction. I express sincere gratitude to my doctoral committee members, Capt Brook Bentley, Dr. William Bailey, and Dr. Graham Candler, for their advice, knowledge, and comments on my dissertation.

The basis of this research was started by Dr. Candler from the University of Minnesota, Dr. Matthew MacLean of CUBRC Inc., and Dr. Jochen Marschall of SRI International. They were gracious enough to spend numerous hours helping me with the implementation and further development of the finite-rate ablation models. Their help was invaluable to the successful accomplishment of this work. Also, Dr. Heath Johnson and Dr. Matthew Bartkowicz from GoHypersonic, Inc. provided endless advice and debugging support. Many thanks are given to Dr. Ryan Gosse from the Air Force Research Laboratory for many helpful discussions providing research guidance and Dr. Aaron Brandis of the NASA Ames Research Center for his assistance in using NEQAIR. A huge thank you goes to Danielle St. Louis for her technical editing expertise and making me realize that I use way too many nominalizations!

The experimental work would not have been possible without the support of the Australian Research Council and the University of Queensland. Specifically, I'm indebted to Steven Lewis, Guerric De Crombrugghe de Looringhe, Dr. Troy Eichmann, Dr. Timothy McIntyre, and Dr. Richard Morgan for their assistance in operating the X-2 facility. I would also like to recognize Dr. Fabian Zander who assisted with the TCRP analysis. Getting the chance to work in a world-class hypersonic facility was

truly a rewarding experience.

Christopher R. Alba

Table of Contents

List of Figures

xiii

List of Tables

List of Symbols

A Nonequilibrium Finite-Rate Carbon Ablation Model For Radiating
Earth Re-entry Flows

I. Introduction

THE Air Force confronts an uncertain, dynamic future as it faces strategic policy changes, force structure overhauls, technological advancements, and severe resource constraints that in 2010 prompted the United States Air Force Chief Scientist to release his vision for future science and technology (S&T) investments. The "Technology Horizons" vision document lays the foundation for how the Air Force was going to maintain its technological advantage throughout the world. Within this document, the Chief Scientist identifies 30 Potential Capability Areas (PCAs) that can counter different potential threat environments and keep the United States at the technological forefront [2]. Among the potential threat environments the Air Force will likely encounter in the future is that of an anti-access/area-denial environment. One of the key technology areas that would enable the Air Force to operate in such an environment is that of hypersonic systems. In fact, four of the 30 PCAs identify hypersonic systems or technologies as being critical capabilities to ensure operational success, which are prompt theater-range ISR/strike systems, penetrating persistent long-range strike, high-speed penetrating cruise missile, and reusable airbreathing access-to-space launch [2].

The need to penetrate highly-defended adversary airspace to achieve desired effects will likely remain an enduring requirement past the intended vision time frame of 2030. The Air Force S&T leadership reinforced this vision, led by the Air Force Research Laboratory (AFRL) commander, by making long range precision strike an

increased emphasis technology area [3]. Investment areas include high-speed propulsion systems, high temperature materials and structures, and high-speed system integration and demonstration. The goal of long range precision strike is to develop a high-speed weapon or aircraft to engage high-value, time sensitive targets in anti-access/area-denial environments.

Development of hypersonic systems encompasses a multitude of scientific disciplines, but the design of a thermal protection system (TPS) is one of the most critical investment areas because its failure could result in a total loss of the vehicle. Because a TPS is a critical investment area, the Air Force had a joint program with the Defense Advanced Research Projects Agency (DARPA) called Falcon aimed at advancing capabilities for access to space and hypersonic flight [121, 122]. As part of the Falcon program, a series of hypersonic demonstration vehicles were developed, and specifically the vehicle designated as Hypersonic Technology Vehicle 2 (HTV-2) was supposed to demonstrate enabling technologies for future hypersonic re-entry operational systems [30]. The technologies to be evaluated were thermal protection systems, aerodynamic shapes, maneuverability, and long-range communication for hypersonic cruise and re-entry applications. The design of the external TPS proved to be one of the most challenging technology areas for the HTV-2 program. Unfortunately, the HTV-2 had two unsuccessful test flights that resulted in an incomplete evaluation of pertinent hypersonic technologies. Other high-speed programs such as the Space Shuttle, NASP, X-33, Genesis, X-37, and Hy-Fly also spent a considerable amount of effort designing effective TPS systems [86]. All of these vehicles utilized carbon-based materials for their critical high temperature aerodynamic, structural, and propulsion applications.

One of the reasons why a TPS is a challenging technology area is because a TPS is subjected to severe thermal and mechanical loads when exposed to hypersonic re-

entry environments and must be designed to prevent excessive heat from damaging the vehicle. The materials used for a TPS interact with the flow through various thermochemical and thermophysical processes such as ablation, spallation, thermal conduction, and radiative transport. In most flight regimes, radiation is ignored because the flow does not reach very high temperatures. However for hypersonic flows, strong shocks develop that lead to high temperatures around the vehicle. To accurately analyze the overall heat transfer in these flows, modeling of air chemistry effects and radiation from hot shock layers must be considered. Additionally, re-entry conditions can have thermal and chemical nonequilibrium within different regions of the flow and these relaxation processes must be accounted for as well. In recent years, computational fluid dynamics (CFD) capabilities have made great progress in simulating the effects of ablation and radiation. However, the degree of complexity and fidelity varies within different research codes in how to model ablation and radiation since the computational cost of implementing the most general theories is prohibitive and not practicable. In reality, all of these phenomena are highly coupled [14].

One consideration that is vital to developing a TPS is the accurate modeling of gas-surface interactions under hypersonic conditions, which remains to be a challenging and complex problem. Surface reactions both degrade TPS materials and contribute to aerothermal heating. It is crucial to have reliable predictive capabilities that can accurately compute the thermophysical environment surrounding the vehicle as well as the chemical kinetics occurring on the surface. However, detailed information regarding gas-surface interactions is lacking from experimental data and the ablation process is mainly characterized by recession rates or reaction efficiencies [28, 33, 60, 95, 114, 116, 135]. Therefore, numerical models used for the surface kinetic processes are of low fidelity and large safety factors are applied to TPS designs. For example, the prediction of the convective heat load on the Mars Science Laboratory developed
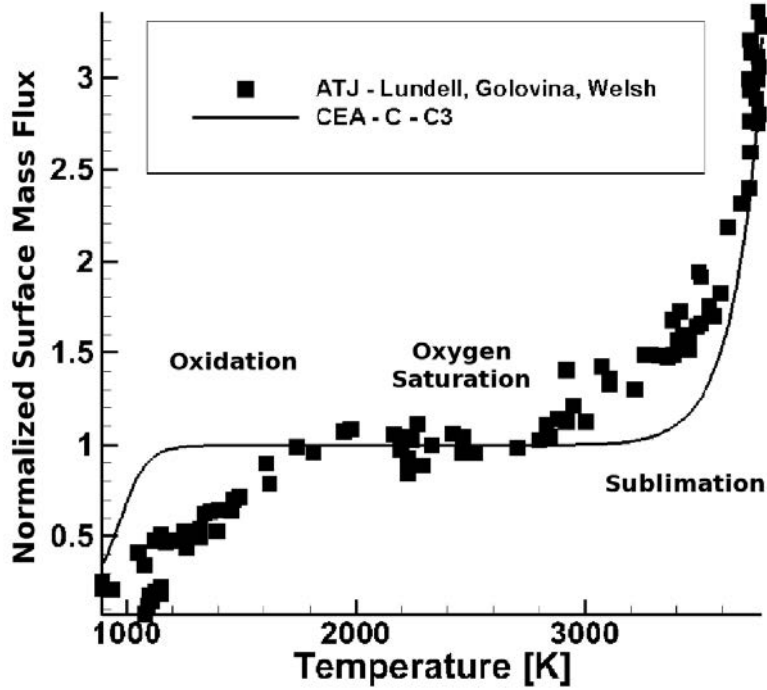
Figure 1. Surface mass flow rates from a collection of graphite ablation experiments as function of surface temperature at 1 atm. Adapted from Gosse et al. [36]

by NASA had a 60% uncertainty, which required a 40% increase in TPS thickness [18]. Additionally, for strongly radiating species like CN [118], the accurate modeling of species formation rates is critical for calculations of radiative heating. Greendyke and Hartung [38] noted that the radiative contribution to the overall heat transfer for blunt re-entry vehicles could be as high as 50% or more in high nonequilibrium flow environments.

To improve modeling efforts, the characterization of TPS materials must be fully understood. The fundamental material found in most carbon-based TPS is graphite, which, in hypersonic re-entry flows, can react due to oxidation, nitridation, and sublimation. The dominant mechanisms of graphite ablation over a range of surface temperatures at 1 atm are shown in Figure 1. Data from different graphite ablation experiments is compared to equilibrium ablation results predicted using the NASA Chemical Equilibrium with Applications (CEA) thermo-chemical database [70]. For

temperatures less than approximately 2000 K, the primary surface reaction is carbon oxidation. Between temperatures of approximately 2000 and 3000 K, the ablation rate plateaus indicating a diffusion-limited ablation regime. In this regime, all of the available oxygen at the surface is entirely consumed by the oxidation reactions. Above 3000 K, graphite sublimation is the dominant mechanism and ablation rates exponentially increase. Oxidation and nitridation are exothermic reactions that consume solid carbon and inject gas into the boundary layer. The coupling between the surface and the flow field is a non-linear process under hypersonic flight conditions, and the balance between catalytic and surface-participating reactions are often unclear [67]. A correct understanding and accurate modeling of all of these ablative phenomena play an integral part in the design of TPS for re-entry vehicles.

Ablation is typically modeled under the assumption that the surface and surrounding gas are in chemical equilibrium. Previous comparisons to experiments and flight data have shown that assumptions of equilibrium provide a conservative estimate of the heat fluxes on the surface of vehicles such as the Apollo capsule, Pioneer-Venus probes, Galileo entry probe, and Stardust return capsule [98, 49, 112]. For the Stardust return capsule that had an Earth entry velocity of 12 km/s, equilibrium surface recession was over predicted by 50% at some locations [112]. When the analysis was performed assuming nonequilibrium at the surface, peak ablation rates decreased by 39% and the total heat load decreased by 32%. The nonequilibrium surface recession was closer to the measured recession and was only over predicted by 11% [13]. Nonequilibrium had a significant effect on the prediction of the thermal and chemical environment surrounding the Stardust return capsule. For very high energy flows, a nonequilibrium treatment using finite-rate surface chemistry models is required.

Another challenge to TPS design is that there is no universally supported surface kinetic model for the air-carbon system. There is a vast amount of reference material

on the chemistry of a carbon surface [17, 16, 33, 106, 15, 89, 8, 48], and in fact, the first theory on surface adsorption of gases is attributed to Langmuir [51] back in 1918. There have been several attempts to model the surface chemical kinetics, but investigators have not reached a common opinion about what the main processes are on the carbon surface [136, 44, 14]. As a result, much uncertainty remains on this topic. Generally, experiments investigating these types of surface reactions will report loss coefficients describing the fraction of gas-surface collisions that remove species from the gas phase [37, 9, 66]. Usually these loss coefficients are curve-fit as functions of temperature, which can then be incorporated as a boundary condition into CFD simulations [113]. However, this approach is purely empirical and does not account for any physics-based mechanisms causing the surface reaction [67].

It is important to note that the radiation emitted away from a re-entry vehicle is of interest to not only design engineers but also the intelligence community (IC). It is reasonable to assume that near-peer countries to the United States (US) are pursuing stealthy hypersonic weapons and/or countermeasures to hypersonic technologies in response to our own system developments. Therefore, it is imperative that the IC have the capability to detect and identify enemy hypersonic weapons as a matter of national security. As Martin [69] points out, while it may be possible to reduce radar cross-sections and mask propulsion signatures, it is impossible to conceal radiation emitted from vehicles moving at high Mach numbers. Hence, any improved thermochemical models will enhance the capability of the IC to correctly identify hostile vehicles that pose a threat to the US or its interests. It is due to all of these considerations that the model which is developed in the following chapters is proposed.

The goal of the research described in this dissertation is to advance our understanding of the gas-surface interactions for the air-carbon chemical system in a high temperature, reacting flow environment by improving current ablation models to bet-

ter match experimental measurements. To evaluate the ablation models, a series of high-speed flow experiments were conducted in the X-2 facility at the University of Queensland, Australia. The X-2 facility is a shock expansion tunnel that can be used to test subscale models at realistic flight temperatures and enthalpies. The model used in the experiments was a short half-cylinder made of isomolded graphite and was tested at 8.6 km/s Earth entry flow monitored by ultraviolet (UV) spectrometry. The experiments pre-heated the model to high temperatures to stimulate surface reactions and increase ablation during the microseconds of available test time [133]. Further development of pre-heating techniques and capabilities have enabled the testing of carbon models approaching sublimation surface temperatures [56]. The nonequilibrium chemistry occurring in the shock layer was investigated by making calibrated measurements of the radiance emitted by the CN molecule. The choice of analyzing CN was ideal since it is a strong emitter and radiates in the UV spectrum for which the X-2 facility is equipped to measure. Also, an attempt was made to capture radiation spectra from C_2 and C_3 at near sublimation conditions. The experiments provided benchmark data to test the validity of the physical models used in the numerical simulations.

The work outlined in this dissertation aligns itself with the following four research objectives:

Research Objective 1: Perform an in-depth computational study by comparing current state-of-the-art ablation models and identify a preferred model at conditions of interest.

Research Objective 2: Propose improved ablation model by developing *original* finite-rate surface reactions based on experiments and theory.

Research Objective 3: Perform sensitivity study to determine which surface reactions have most impact on radiative heating and ablation rates.

Research Objective 4: Validate developed ablation model against the benchmark X-2 experimental results.

Chapter II provides an overview of the experiments performed in the X-2 facility. In Chapter III, the theory and computational methodology is presented describing the implementation of the ablation boundary condition into a CFD code. Before applying the ablation models to the X-2 experiments, Chapter IV characterizes the models in a representative blunt body re-entry flow. Chapter V then presents the results and analysis of the radiation comparisons to the X-2 measurements. Additionally, proposed modifications to a current surface model are implemented, providing better agreement with the experimental data. Finally, Chapter VI provides conclusions and proposes future work.

II. Experimental Testing

Understanding hypersonic re-entry remains one of the greatest challenges to aerospace engineers due to the many different types of phenomena present in the flow field, which include viscous-inviscid interactions, surface ablation, nonequilibrium thermodynamics, finite-rate chemical reactions, and radiative heat transfer [108]. The only way to investigate these phenomena in a coupled manner is through flight testing because ground test facilities are unable to replicate all aspects of hypersonic flight conditions. However, the expense of flight test programs has become so great that more emphasis is being placed on ground testing for the design of future hypersonic systems.

The premise of this dissertation is that integrating computational fluid dynamic (CFD) simulations with ground experiments will greatly improve our understanding of the phenomena seen in hypersonic flight and mitigate some of the limitations of ground testing. For example, shock expansion tunnels can reproduce hypersonic flight speeds and enthalpy conditions, but the test times are very short, 100 μs to 2 ms, which does not allow for any model thermal response [132]. Arc heated facilities enable steady-state testing of the thermal environment but do not correctly simulate hypersonic conditions [59]. However, by attempting to piece together the different regimes of hypersonic flight in ground test facilities, and coupling those results with CFD simulations, heavy reliance on flight test programs may not be needed.

To study the effects of ablation in expansion tunnels, a recent pre-heating concept was developed at the University of Queensland [132, 133, 56]. The concept involves electrically pre-heating carbon-based materials, such as those commonly used for a TPS, up to temperatures approaching the sublimation ablation regime. An environment is created where the surface boundary condition is matched to that seen in re-entry flight, and the gas-surface interaction can be simulated. It is then possible to numerically simulate these flows and compare radiation intensities to those measured

9

in the experiments. The following sections describe the experimental setup used for the expansion tunnel tests.

2.1 X-2 Facility

The hypersonic testing was conducted in the X-2 shock expansion tunnel at the University of Queensland, Australia. The tunnel is a free piston driven facility capable of simulating re-entry conditions for different atmospheres at speeds of up to 13 km/s. The operation of the X-2 facility is illustrated in Figure 2. The tunnel is a single tube separated into three sections by two diaphragms. A 2.0 mm thick pre-scored, steel primary diaphragm separates the driver section and shock tube, while a thin aluminum sheet secondary diaphragm separates the shock tube from the acceleration tube [29].

The piston is accelerated by a large gas reservoir that compresses the driver gas until the pressure is sufficiently high to rupture the primary diaphragm. The shock wave that is produced propagates through the shock tube accelerating the test gas until the secondary diaphragm is ruptured. The test gas is then free to flow downstream into the lower pressure of the acceleration tube. The test gas expands and accelerates as it travels through the nozzle, greatly increasing its energy in an isentropic unsteady expansion [29]. This whole process creates high enthalpy test flows suitable for aerodynamic testing.

A steady test flow is established through the nozzle exit and is passed over a subscale model or instrumentation package in the test section. A typical available test time is on the order of tens to several hundred microseconds. Optical windows at the sides of the test section allow non-invasive optical diagnostic techniques such as flow visualization through high-speed imaging or emission spectroscopy. Further information on the X-2 facility and its capabilities can be found in References [29, 71,

s = shock   cs = contact surface   usx = unsteady expansion
rs = reflected shock   sx = steady expansion   u + a = reflected u + a characteristic

Analytically indeterminant region
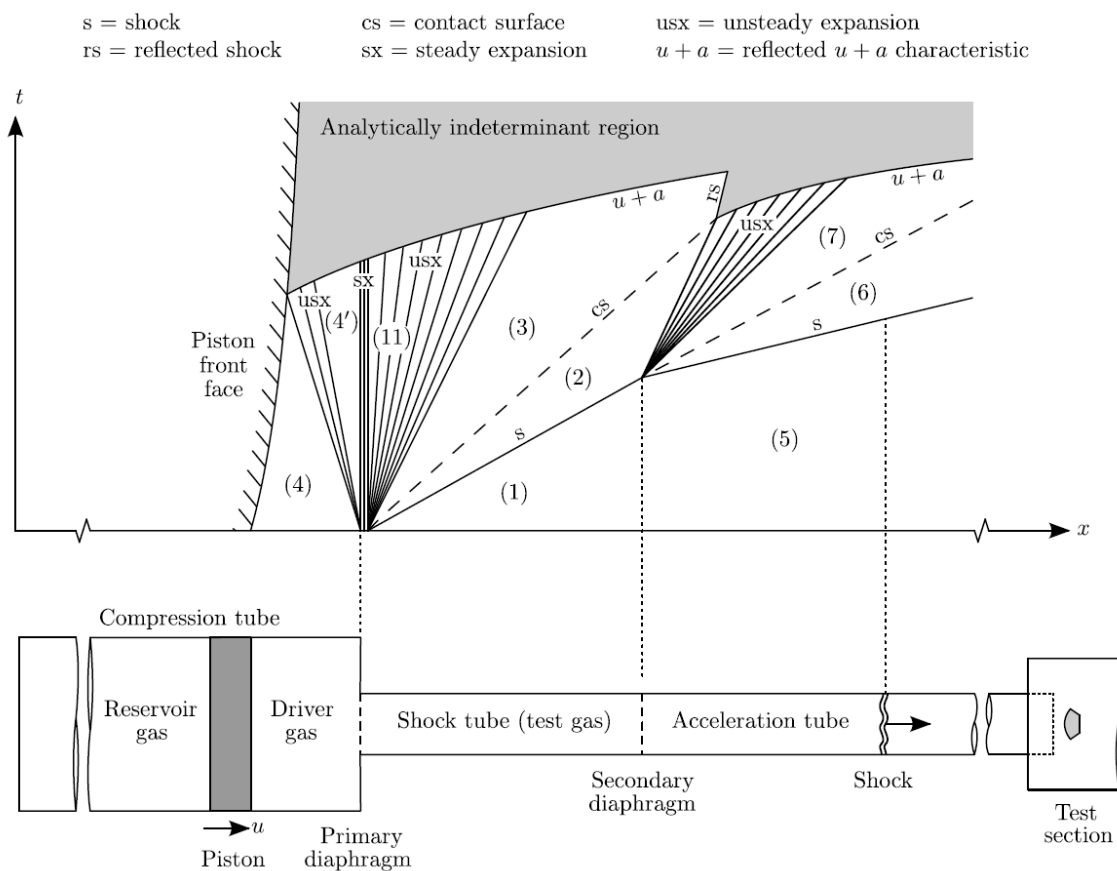
Figure 2. **Schematic diagram of the X-2 expansion tunnel and ideal x-t diagram [57].**

Table 1. Calculated X-2 freestream conditions.

Parameter	Value
Total Enthalpy (MJ/kg)	38.2
Pressure (Pa)	847
Temperature (K)	2040
Velocity (m/s)	8500
Density (kg/m^3)	1.45×10^{-3}
y_{N_2}	0.751
y_{O_2}	0.225
y_{NO}	8.53×10^{-3}
y_{CO}	1.26×10^{-5}
y_{CO_2}	4.65×10^{-4}
y_{Ar}	0.013
y_{O}	2.37×10^{-3}

Table 2. X-2 fill conditions for each section of the expansion tunnel.

Reservoir	Driver	Shock Tube	Acceleration & Test Section
6.85 MPa	742 mBar He	3 kPa Air	10 Pa Air
	186 mBar Ar		

75].

The tunnel condition used for these tests was a 8.6 km/s flight speed equivalent, which is representative of Earth re-entry conditions. The freestream conditions of the test flow are shown in Table 1. An estimate of the freestream conditions was detailed by Zander [131], which was a one-dimensional nozzle simulation that used an equilibrium assumption to calculate the chemical composition of the flow. The X-2 fill pressures for each section of the expansion tunnel are specified in Table 2.

2.2 Graphite Test Model

The conducted tests used a half-cylinder model that had a 50 mm outer diameter, a 46 mm inner diameter, and was 10 mm thick. The material used for all test models was GM-10 grade isotropic graphite manufactured by Graphel, LLC. The graphite is
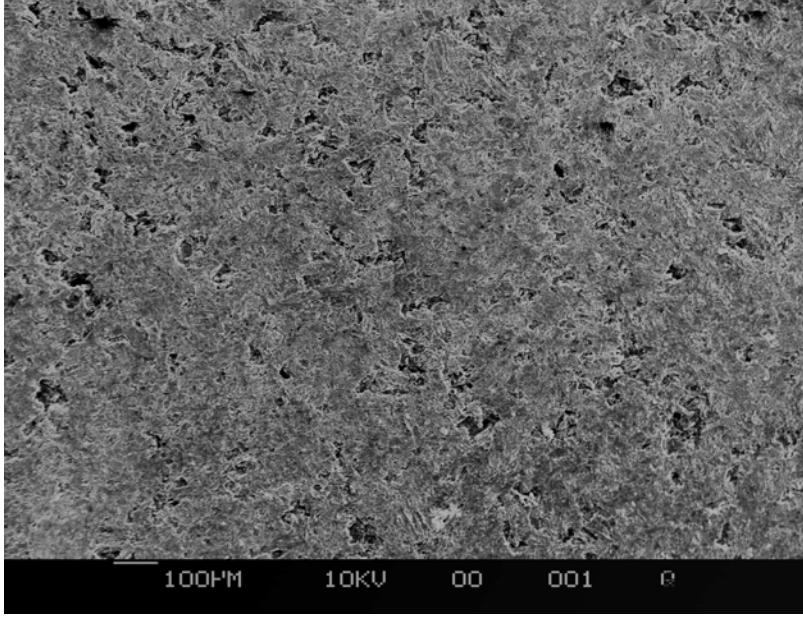
Figure 3. SEM image of the ISO-63 grade graphite surface at a magnification of 100 μm.

isostatically pressed to produce a very fine grain, high density sample. The graphite has an amorphous structure with no defined orientation as shown in Figure 3. The surface was imaged using a scanning electron microscope (SEM) at a magnification of 100 μm. The resistivity and density of the graphite is 1500 $\mu\Omega$/cm and 1.78 g/cm^3, respectively. The amount of resistive heating is driven by the resistance of the model, which is a function of the density. A higher resistance translates to larger achievable wall temperatures.

The model is positioned in the center of the core flow exiting the nozzle, which generated a three-dimensional flow field. Figure 4 displays a schematic and actual view of the model located in the tunnel during testing. A new model was used for each test because the model gets destroyed after arrival of the driver gas.
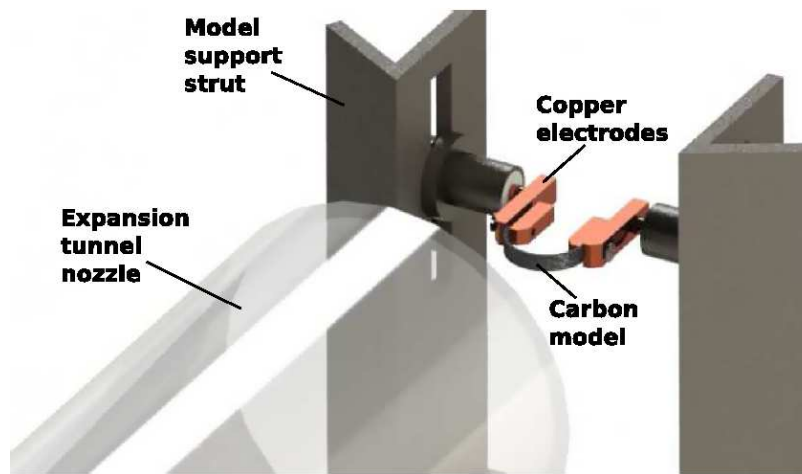
(a) Schematic
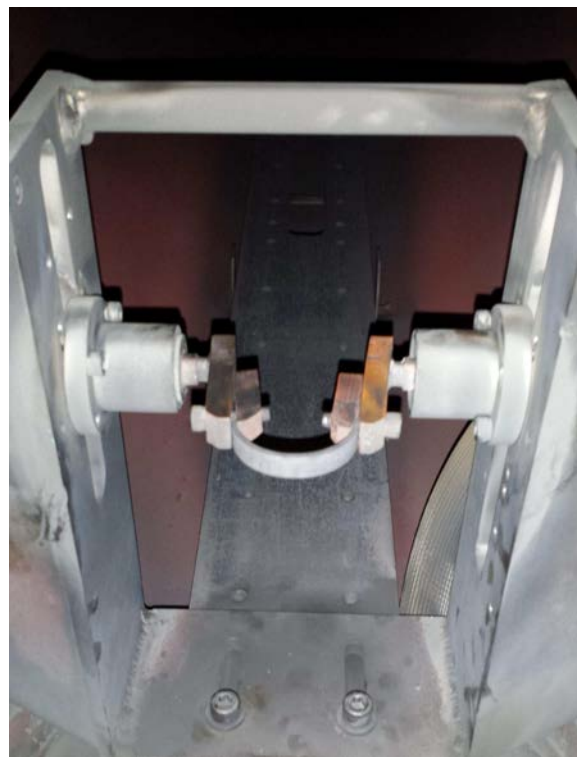
(b) Actual

Figure 4. Schematic and actual view of carbon model in the X-2 test section [133].

2.3 Techniques

2.3.1 Model Pre-Heating.

Pre-heating of models can be used to eliminate the time requirements necessary to correctly simulate the effects of ablation and surface chemistry in expansion tunnels. The time required to observe ablation effects in expansion tunnels is on the order of seconds for models initially at room temperature [74]. However, expansion tunnels only have test times on the order of microseconds. Zander et al. [133] has shown that pre-heating of the model can remove this time requirement by achieving re-entry surface temperatures that allows for the study of ablation and gas-surface interactions in hypersonic flow fields. The pre-heating is done by sending an electric current through the model, which gets conducted through the entire cross-section resulting in a uniform surface temperature. Prior to each test, the model was raised to the desired temperature and held at that temperature for approximately 5 seconds before firing. The model temperature was controlled by selecting an appropriate amperage with the power supply.

2.3.2 Two Color Ratio Pyrometry.

Determination of the model surface temperature was achieved by the two color ratio pyrometry (TCRP) technique. It is necessary to know the temperature of the model surface before the flow arrives in order to replicate these experiments with numerical simulations. The TCRP technique is described by Zander et al. [133], and it can be implemented with a commerically available digital single-lens reflex (DSLR) camera.

Two color ratio pyrometry relies on the ratio of light intensities at two different known wavelengths. Digital cameras provide this capability by capturing intensities for red, green, and blue wavelengths. The two color ratios can be used to calculate a
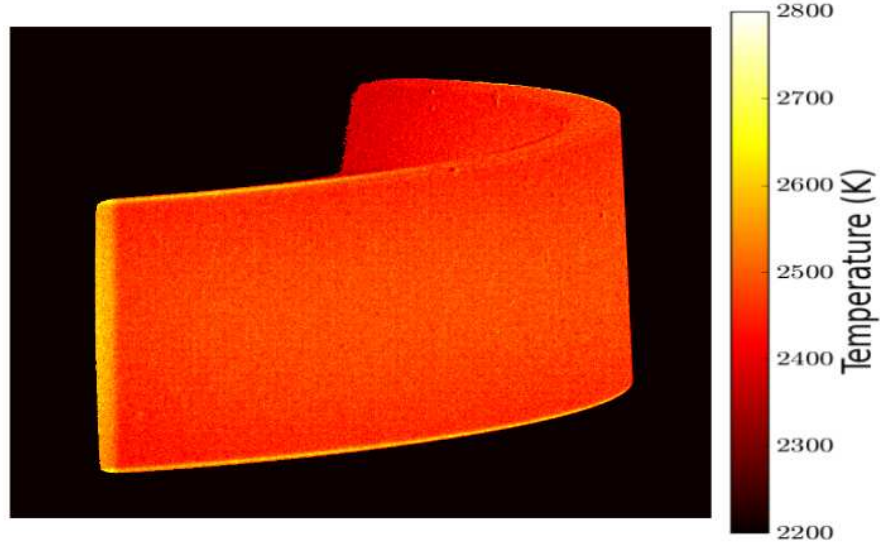
Figure 5. Representative two-color ratio pyrometry analysis displaying temperature contours derived from a DSLR image of the graphite model. Image taken immediately before test time.

temperature for each pixel using the image data. The graphite model was assumed to be radiating as a grey body (i.e. constant emissivity), which is consistent with other research involving carbon-carbon materials in near-vacuum conditions [133, 10]. The camera used for the tests was a Canon 400D DSLR with a Canon EF 75-300 mm lens. The images taken targeted the front surface of the model. Typical settings used during the tests were ISO 100, 1/4000 exposure, f/10 aperture and a focal length of 300 mm. An example TCRP analysis is shown in Figure 5 illustrating a fairly uniform temperature across the entire surface.

2.3.3 High Speed Imaging.

Recordings of each experimental test were done with a Shimadzu HPV-1 Hyper-vision high speed CCD camera. The high speed camera is capable of frame rates up to 1 MHz and records the luminosity of the flow over the model. The high speed video from each test was used to check the timing of the spectrometer's exposure

with respect to shock arrival, flow stabilization, and the end of steady test time. The videos for all the tests were recorded at a frame rate of 500 kHz, which allowed for all stages of flow development to be observed with a total recording time of 202 μs.

An example analysis is shown in Figure 6 with a model at a surface temperature of 1920 K. Figure 6b exhibits a time where steady conditions were achieved and 6c shows when the spectrometer was first exposed. Any test that had an excessive amount of luminosity due to contaminants, such as iron and aluminum, during the spectrometer exposure time were rejected. Figure 6e indicates the end of steady test time and shows driver gas arrival.

2.3.4 Ultraviolet Spectrometry.

Measurements of shock layer emissions were performed using an Acton Research SpectraPro 2300i spectrometer coupled to a Princeton Instruments PI-MAX ICCD UV-sensitive camera. The spectrometer was configured using a grating with a groove density of 1800 g/mm, centered at 372.5 nm that covered a wavelength range of 353-391 nm. The wavelength range was chosen to provide the maximum spectral resolution of the primary radiative transitions for the CN violet bands. The camera used a 20 μs delay and an exposure time of 15 μs during steady test time.

During initial testing at surface temperatures in excess of 3000 K, attempts were made to observe radiation from the C_2 Swan and C_3 Swings bands. For these tests, a 600 g/mm grating centered at 415 nm was used, which allowed observation from 350-480 nm. No discernible signal from these emission bands could be measured. Therefore, it was decided to focus only on the previous spectrometer settings that targeted CN.

The high temperature gas emits light through a pair of UV grade fused silica windows mounted on both sides of the X-2 test section. The UV optical path is
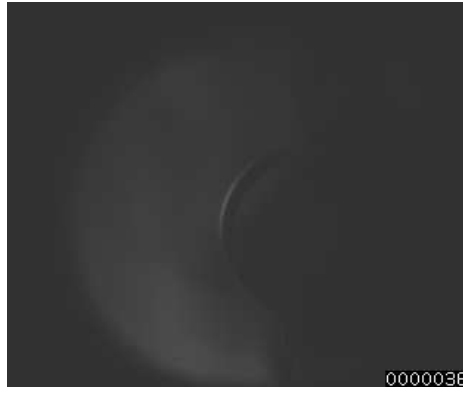
(a) Shock arrival ($t = 36\,\mu s$)
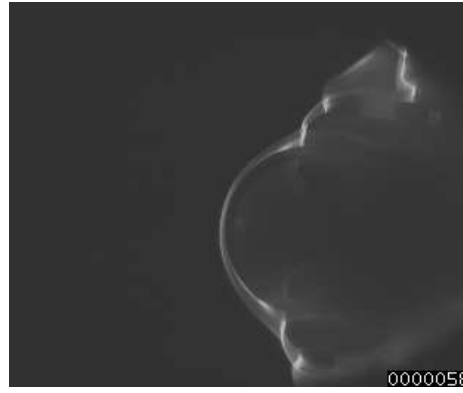
(b) Flow structure established ($t = 58\,\mu s$)
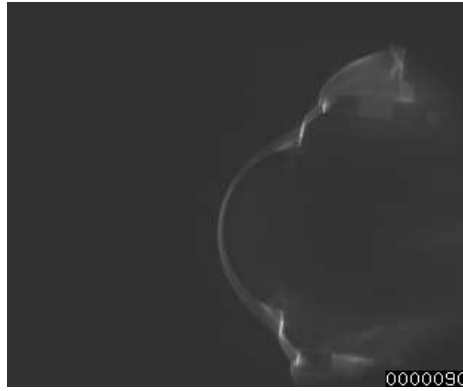
(c) Spectrometer start ($t = 90\,\mu s$)
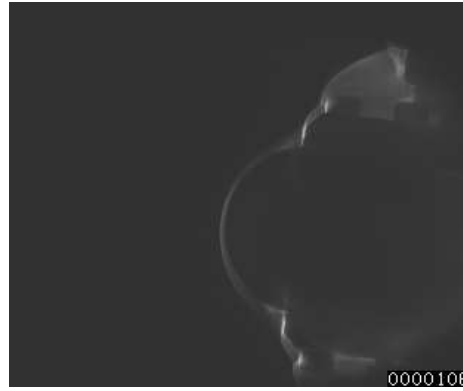
(d) Spectrometer finish ($t = 106\,\mu s$)
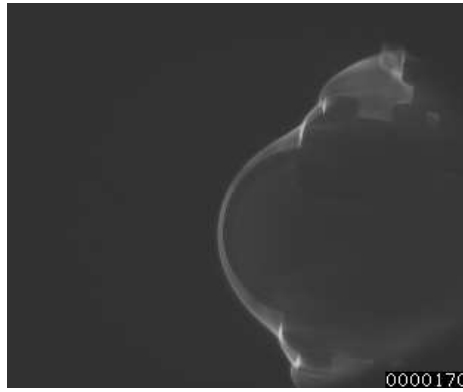
(e) Driver gas arrival ($t = 170\,\mu s$)
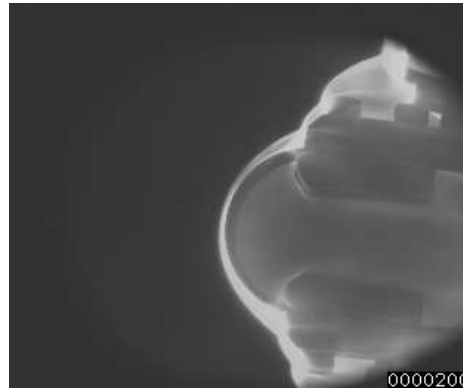
(f) Steady test time ended ($t = 200\,\mu s$)

Figure 6. Example analysis of high speed footage (times shown are with respect to start of video) [57].

diagrammed in Figure 7. A concave focusing mirror, flat turning mirror, and periscope were used to redirect the light onto the 50 μm wide entrance slit of the spectrometer. The periscope changes the height of the light path from the test section window to the height of the spectrometer entrance slit, and reorients the image by 90° as geometrically required to capture the model surface, shock layer, and freestream flow. All optical components were UV enhanced magnesium fluoride/aluminium coated mirrors to ensure good reflectivity at the wavelengths of interest [29].

2.4 Acquisition of Spectra

The radiation measured by the UV spectrometer during testing targeted the stagnation streamline region of the model. Figure 8 shows the capture area of the UV spectrometer that was imaged. Inside this capture area, the spectrometer camera accumulates an image of the model surface, shock layer, and some of the freestream. Note that the vertical dimension of the capture area identified in Figure 8 has been magnified for clarification.

The resultant image is a two-dimensional plot of pixel intensity with wavelength and spatial distance as the two axes. An example raw data image is shown in Figure 9 with the shock front, boundary layer edge, model edge, and flow direction labeled. The calibration process is described in Lewis et al. [57], which converts the raw spectral data, measured in the arbitrary units of "counts", into spectral radiance with units of W/(cm^2-μm-sr). Figure 10 shows the calibrated spectra, which have been spatially averaged within the boundary layer region, for the surface temperatures ranging from 1770-2410 K. The primary CN radiative transitions are clearly seen in this figure.
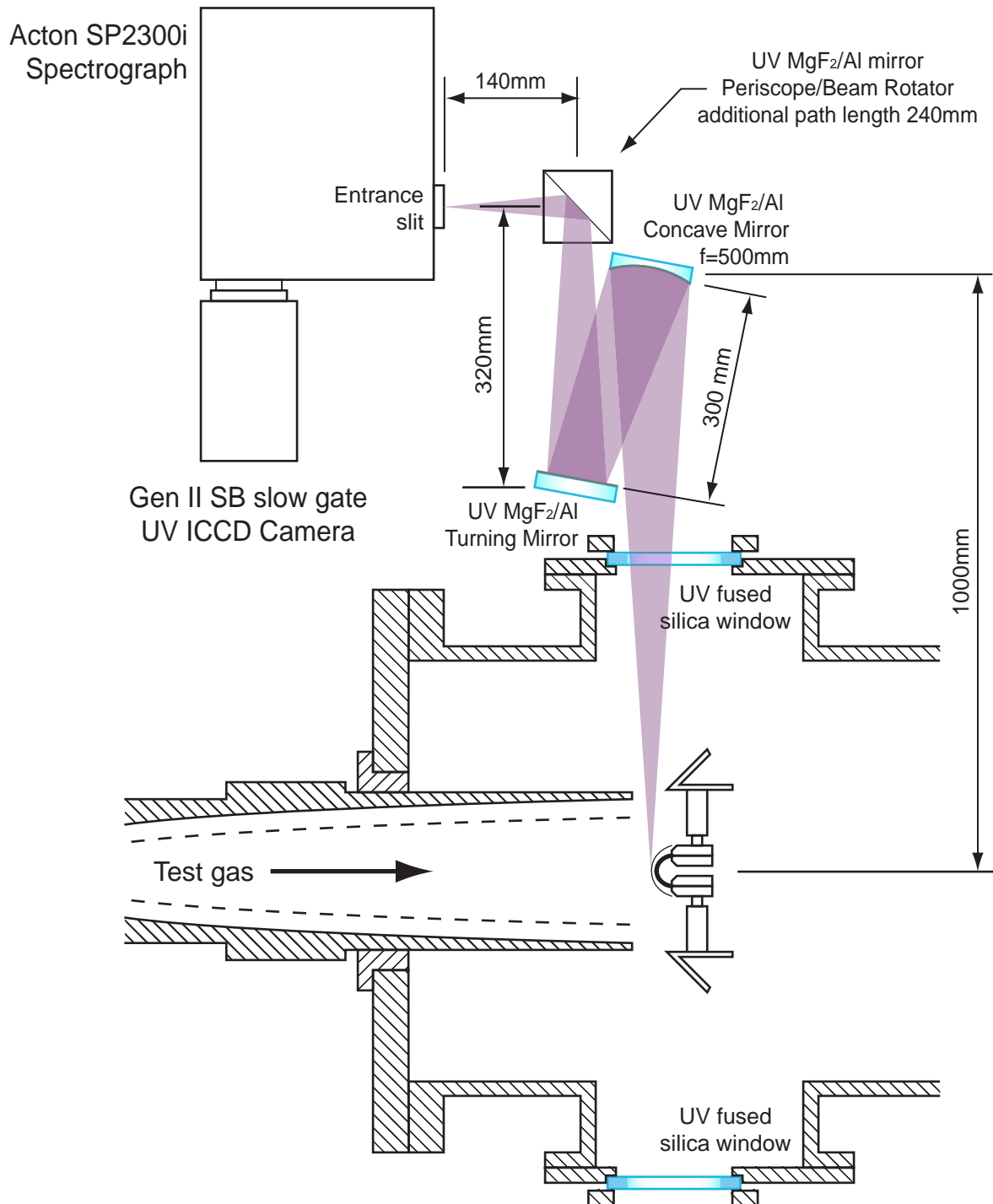
Figure 7. Schematic of UV spectrometer layout used during X-2 testing (adapted from Eichmann [29]).
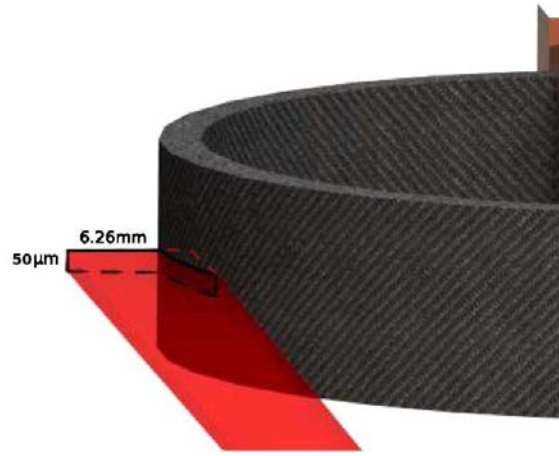
Figure 8. Side view of UV spectrometer capture area on the model (slit height not to scale, adapted from Zander et al. [133]).
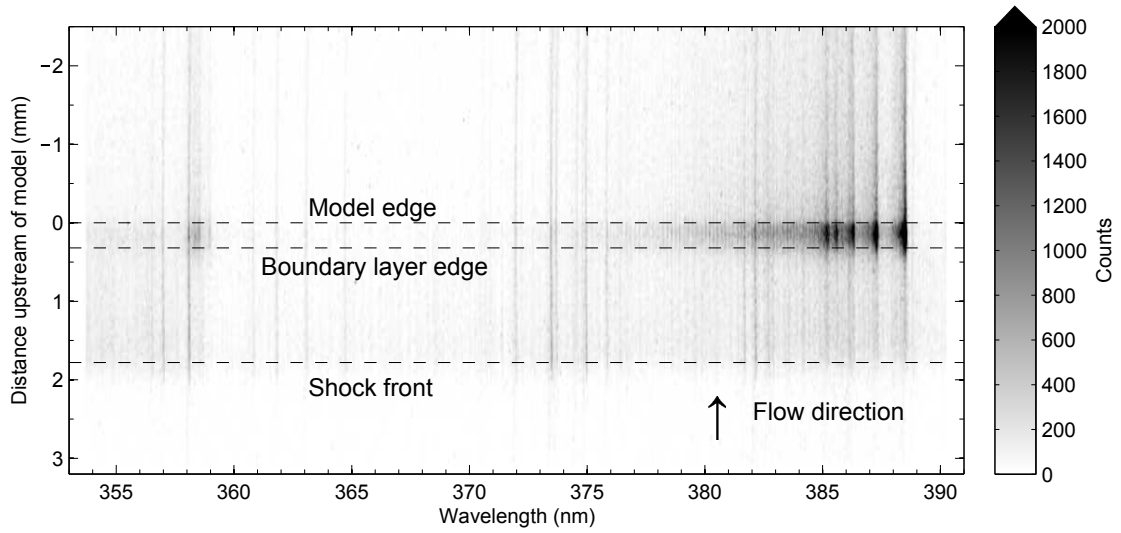
Figure 9. Raw spectral data for 2170 K test (scale adjusted for visibility, adapted from Lewis et al. [57]).
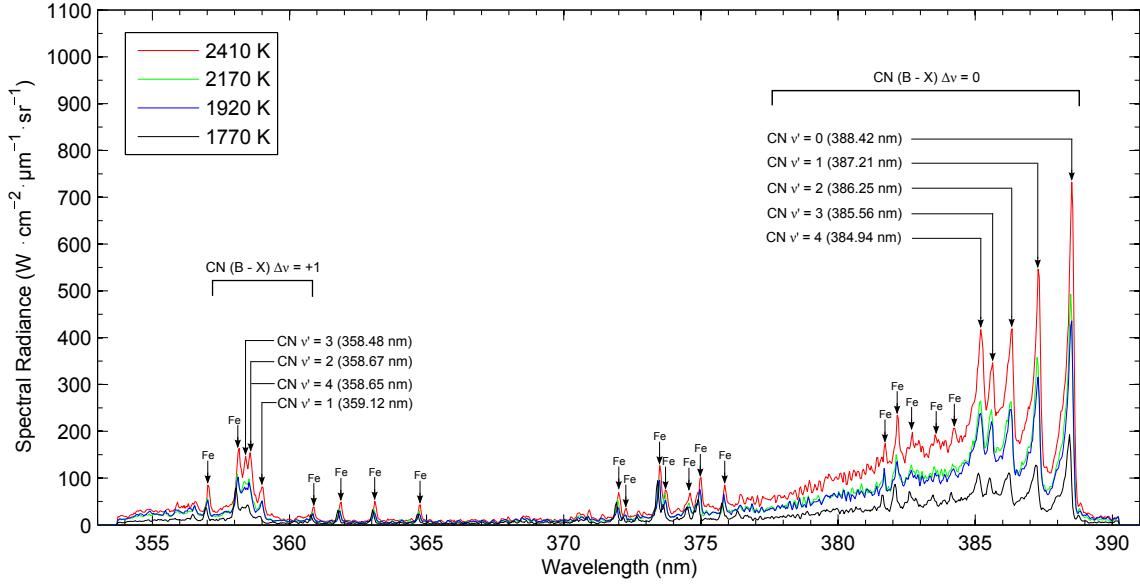
Figure 10. Spectra averaged within the boundary layer [57].

2.5 Cases

There were two separate experimental test efforts or "campaigns" that focused on different ablation regimes. The first campaign focused on the oxidation and nitridation reactions with a surface temperature range of 1770-2410 K. The second campaign attempted to achieve sublimation surface temperatures with a range of 2610-3280 K. Between the two campaigns, there were a total of eight experimental tests that produced "clean" spectral results. The measured wall temperature along with its associated uncertainty are provided in Table 3. It should be noted that the DSLR images taken for case 3 were overexposed and therefore unusable. Therefore, the temperature supplied for case 3 was taken from another test with identical power settings which was rejected due to flow contamination [57]. Cases 1-4 were from the first experimental campaign and cases 5-8 were from the second.

The maximum temperature for the first campaign was limited by the available power supply. The power supply used for the first campaign was a 10.75 V DC

Table 3. Measured wall temperature for each test case.

Case Number	Wall Temperature (K)	Uncertainty (K)
1	2410	±280
2	2170	±180
3	1920	±180
4	1770	±180
5	3280	±20
6	3190	±40
7	2760	±180
8	2610	±140

rectifier, which could provide up to 250 A with this test model. To achieve higher temperatures, a low-ripple DC rectifier capable of supplying up to 1500 A was purchased. Analysis by Lewis et al. [56] found that supplying approximately 450-500 A could achieve surface temperatures of 3000-3300 K. A comparison of SEM images of before and after heating to 3300 K is provided in Figure 11. Heating the graphite model to 3300 K resulted in a significant change to the surface structure, particularly an increase in porosity, which had unforeseen consequences during testing that will be discussed later.

The presence of iron contamination in the spectrum, as seen in Figure 10, was problematic because it caused integrated radiance levels to be higher than that of a clean flow. However, Lewis et al. [57] showed that the error due to iron contamination was not significant. Emission from CN was estimated to contribute 75-85% of the total measured radiance within the boundary layer region. The cases identified in Table 3 were selected for analysis because they had the lowest levels of contamination. The next chapter will discuss the numerical theory used to simulate these cases.
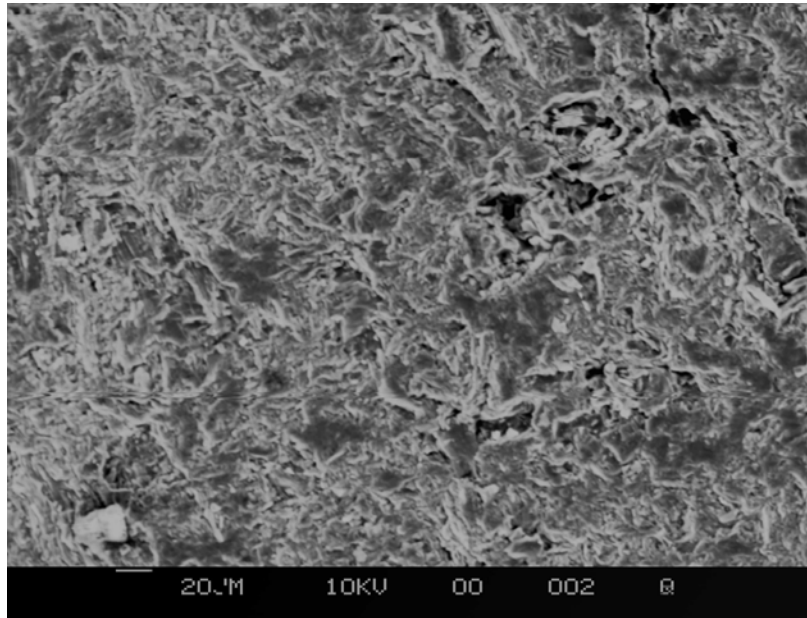
(a) Before heating.
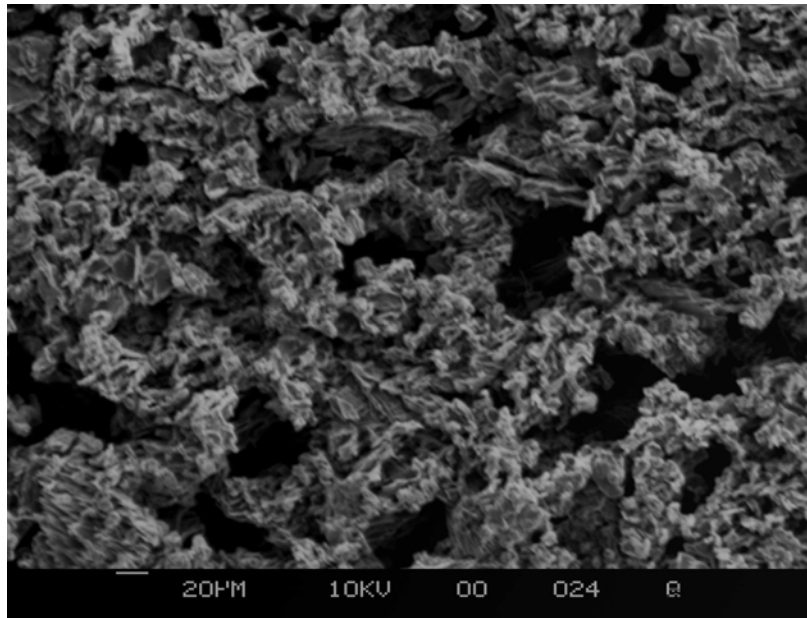
(b) After heating to 3300 K.

Figure 11. SEM images taken at a magnification of 20 μm comparing the model surface before and after heating to 3300 K.

III. Theory and Methodology

Hypersonic re-entry flows include many physical phenomena that cannot be modeled by the perfect gas form of the Navier-Stokes equations. The types of physical phenomena expected in these flows include chemical and thermal nonequilibrium, vibrational and electronic excitation, and weak ionization. The use of a real gas model, where molecular interactions are considered, is necessary to account for these phenomena.

The following sections will describe the CFD and radiation solvers used in this dissertation. The CFD solver is called US3D, which is a parallel implicit unstructured solver that was developed at the University of Minnesota [80, 81]. The radiation solver is the Nonequilibrium Air Radiation (NEQAIR) code version 13.2 developed at NASA Ames Research Center [125]. The CFD and radiation solutions were computed in an uncoupled manner because the incoming Mach number was around 9.4 and radiative heating was not expected to contribute much to the overall wall heating rate. Additionally, a description of the surface reaction model and how it is implemented as a CFD boundary condition is provided.

3.1 Assumptions

The Knudsen number is the ratio of the mean free path to a characteristic flow length, such as the diameter of the graphite test model, and can be used to distinguish between continuum or non-continuum flow conditions. The continuum formulation requires that the Knudsen number be much less than one (usually less than 0.1) so there are a sufficient number of molecules within a computational volume. Hence, there is little statistical variation at any point, and as a result, the continuum formulation of the viscous fluxes is consistent [22]. The Knudsen number near the stagnation

region for the X-2 flow conditions ranged from 10^{-4} to 10^{-3}. Therefore, the flow fields are assumed to be consistent with a continuum formulation. It is also assumed that there are sufficient number of collisions of the gas molecules with the wall, so there is no velocity or temperature slip. For continuum calculations, the Navier-Stokes equations may be solved to determine flow field solutions.

The thermal state of the gas was assumed to be in nonequilibrium and follows Park's two-temperature model [92, 91]. The energy in the translational and rotational modes of all gas species are characterized by a single temperature, T. A common translational-rotational temperature is a reasonable assumption because typically rotational equilibration with translation is very fast and occurs within a few collisions. The energy of the vibrational and electronic modes of all species and the electron translational energy mode is described by a single temperature, T_v. The justification that these three energy modes can be described by a single vibrational temperature is based on the rapid energy transfer between the translational motion of the free electrons and the vibrational motion of the polyatomic species, and on populations of the low-lying electronic states of heavy particles tending to be in equilibrium with the ground electronic state at the electronic temperature [91]. These assumptions regarding energy transfer simplify the conservation equations considerably by eliminating the need for separate translational and vibrational energy equations for each polyatomic species and an energy equation for electrons. While these simplifications may not be adequate for all high speed problems, they provide accurate results for aerodynamic coefficients and convective heating rates of re-entry vehicles [31].

3.2 CFD Solver

3.2.1 Conservation Equations.

The gas dynamic conservation equations for a individual gas species, s, in a nonequilibrium flow are presented in this section. The equations that describe the conservation of mass, momentum, and energy for a gas species follow the work in References [7, 120, 54]. The species mass conservation equation is given by:

$$\frac{\partial \rho_s}{\partial t} + \frac{\partial}{\partial x_j} \left[\rho_s \left(u_j + v_{sj} \right) \right] = w_s \tag{1}$$

where ρ_s are the species densities, u_j is the velocity in the j direction, v_{sj} is the species diffusion velocity, and w_s are the species mass production rates due to chemical reactions. The momentum conservation equations are written as:

$$\frac{\partial}{\partial t} \left(\rho u_j \right) + \frac{\partial}{\partial x_j} \left(\rho u_i u_j + p \delta_{ij} \right) = -\frac{\partial \tau_{ij}}{\partial x_j} \tag{2}$$

where ρ is the mixture density, p is the pressure, and τ_{ij} are the viscous shear stress components. There is a separate momentum equation for each spatial dimension of the problem. The total energy conservation equation is represented by:

$$\frac{\partial E}{\partial t} + \frac{\partial}{\partial x_j} \left(\left(E + p \right) u_j \right) = -\frac{\partial}{\partial x_j} \left(q_j + q_{v,j} \right) - \frac{\partial}{\partial x_j} \left(u_i \tau_{ij} \right) - \sum_{s=1}^{ns} \frac{\partial}{\partial x_j} \left(v_{sj} H_s \right) \tag{3}$$

where E is the total energy, q_j is the translational-rotational heat flux in the j direction, $q_{v,j}$ is the vibrational-electronic-electron heat flux in the j direction, H_s is the species enthalpy, and ns is the total number of species. Finally, the vibrational-

electronic-electron conservation equation is given by:

$$\frac{\partial E_v}{\partial t} + \frac{\partial}{\partial x_j}\left(E_v u_j\right) + \frac{\partial}{\partial x_j}\left(\sum_{s=1}^{nd} e_{v,s} v_{sj}\right) = -\frac{\partial q_{v,j}}{\partial x_j} + w_v \tag{4}$$

where E_v is the vibrational-electronic energy, $e_{v,s}$ is the vibrational-electronic energy of a polyatomic species, w_v is the vibrational energy source term, and nd is the total number of polyatomic species. The following sections provide more details on how these terms are modeled.

3.2.2 Viscous Terms.

The viscous shear stresses are modeled assuming a Newtonian fluid and are given by:

$$\tau_{ij} = -\mu\left(\frac{\partial u_i}{\partial x_j} + \frac{\partial u_j}{\partial x_i}\right) - \lambda\frac{\partial u_k}{\partial x_k}\delta_{ij} \tag{5}$$

where μ is the mixture coefficient of viscosity and $\lambda = -2/3\mu$ from Stoke's hypothesis.

The translational-rotational and vibrational-electronic heat flux vectors are given by Fourier's heat law:

$$q_j = -k\frac{\partial T}{\partial x_j}, \quad q_{v,j} = -k_v\frac{\partial T_v}{\partial x_j} \tag{6}$$

where k is the mixture translational-rotational thermal conductivity and k_v is the mixture vibrational-electronic thermal conductivity. The species mass diffusion fluxes, J_s, are modeled using Fick's law:

$$J_s = \rho_s v_{sj} = -\rho D_s\frac{\partial y_s}{\partial x_j} \tag{7}$$

where D_s is the species diffusion coefficient and y_s is the species mass fraction. The species diffusion coefficient, D_s, is replaced by a single binary coefficient, D, and

found by assuming a constant Lewis number, Le, by:

$$D = \frac{Lek}{\rho C_p} \qquad (8)$$

where k is the mixture translational-rotational thermal conductivity and C_p is the mixture translational-rotational specific heat at constant pressure. The Lewis number is set to 1.4.

There have been a few recent studies investigating the effects of different mass diffusion models for planetary re-entry vehicles including wall catalytic effects. Gosse and Candler [35] showed surface heating rates and mass fraction compositions computed by Fick's law began to diverge from multi-component diffusion models when freestream velocities were larger than 9.7 km/s. The main reasons for the large differences at freestream velocities greater than 9.7 km/s were due to the flow becoming increasingly dissociated and ionized. Specifically, the increased presence of N and N^+ were causing the surface heating predictions given by Fick's law to be larger than those predicted by the multi-component methods. Alkandry et al. [5] found that Fick's law consistently predicted larger stagnation point heat transfer rates compared to a modified Fick's law and other multi-component diffusion models. The source of the problem was due to Fick's law not enforcing the requirement that the diffusion mass fluxes sum to zero. Both studies used simple catalytic wall models and how the results would change with a more sophisticated surface reaction model is not clear. However, the freestream velocity of the experimental test condition is 8.5 km/s, so using Fick's law is assumed to be reasonable for the cases presented here.

3.2.3 Thermodynamic Properties.

The total pressure is found from the equation of state and is the sum of the partial pressures:

$$p = \sum_{s=1}^{ns} \rho_s \frac{R}{M_s} T \tag{9}$$

where R is the universal gas constant and M_s is the species molecular weight. The total energy of the mixture is given by:

$$E = \sum_{s=1}^{ns} \rho_s C_{v,s} T + \frac{1}{2} \sum_{s=1}^{ns} \rho_s u_i u_i + \sum_{s=1}^{ns} \rho_s h_s^\circ + E_v \tag{10}$$

where h_s° is the species heat of formation. This expression may be inverted to determine the translational-rotational temperature T. The translational-rotational specific heat at constant volume, $C_{v,s}$, is given by:

$$C_{v,s} = C_{v,tr,s} + C_{v,rot,s} \tag{11}$$

where $C_{v,tr,s} = \frac{3}{2} \frac{R}{M_s}$, $C_{v,rot,s} = \frac{R}{M_s}$ for molecules, and $C_{v,rot,s} = 0$ for monatomics. The species enthalpy is defined to be:

$$H_s = C_{v,s} T + R_s T + h_s^\circ + e_{v,s} \tag{12}$$

where $R_s = R/M_s$.

The species vibrational-electronic energy is calculated using the NASA Chemical Equilibrium with Applications (CEA) database. Gordon and McBride [34] and McBride et al. [70] developed a database that can be used to calculate thermodynamic functions for individual gas species. Thermodynamic data can be calculated for a temperature range from 200 to 20,000 K with a library of over 2,000 solid, liquid, and gaseous chemical species. The data are expressed as least-squares coefficients for

the calculation of the specific heat at constant pressure C_p, enthalpy H, and entropy S. From these thermodynamic quantities, the species vibrational-electronic energy can be calculated from the species enthalpy (Equation 12), and the species vibrational specific heat at constant volume can be calculated from the specific heat at constant pressure since $C_v = C_p - R$.

The thermodynamic functions in dimensionless form are as follows. The specific heat at constant pressure is:

$$\frac{C_p(T)}{R} = \frac{a_1}{T^2} + \frac{a_2}{T} + a_3 + a_4 T + a_5 T^2 + a_6 T^3 + a_7 T^4 \tag{13}$$

Enthalpy and entropy are obtained by integrating $C_p(T)$ and $C_p(T)/T$ with respect to T:

$$\frac{H(T)}{RT} = -\frac{a_1}{T^2} + \frac{a_2 \ln(T)}{T} + a_3 + \frac{1}{2}a_4 T + \frac{1}{3}a_5 T^2 + \frac{1}{4}a_6 T^3 + \frac{1}{5}a_7 T^4 + \frac{b_1}{T} \tag{14}$$

and

$$\frac{S(T)}{R} = -\frac{a_1}{2T^2} - \frac{a_2}{T} + a_3 \ln(T) + a_4 T + \frac{1}{2}a_5 T^2 + \frac{1}{3}a_6 T^3 + \frac{1}{4}a_7 T^4 + b_2 \tag{15}$$

where $a_1 - a_7$ are the least-square coefficients and b_1 and b_2 are integration constants. The thermodynamic database inherently accounts for both the vibrational and electronic internal energy modes, making it more accurate than a harmonic oscillator model for high energy flows.

3.2.4 Transport Properties.

The viscosity and thermal conductivities for each energy mode are calculated according to the Gupta-Yos mixing rule, which was designed for weakly ionized or

non-ionized flows [40]. The formulas used to compute the transport properties from the collision cross-sections are obtained from the first-order Chapman-Enskog approximation. For a gas in thermal equilibrium, the mixture viscosity is calculated by:

$$\mu = \sum_{i=1}^{ns} \left(\frac{\frac{M_i}{N_A}\chi_i}{\sum_{j=1}^{ns} \chi_j \Delta_{ij}^{(2)}} \right) \tag{16}$$

where the collision terms, Δ_{ij}, are evaluated at the controlling temperature, T, and the species molar fraction, χ_s, is given by:

$$\chi_s = \frac{\rho_s/M_s}{\sum_{s=1}^{ns} \rho_s/M_s} \tag{17}$$

The translational component of the thermal conductivity in a mixture is:

$$k_{tr} = \frac{15}{4} k_B \sum_{i=1}^{ns} \left(\frac{\chi_i}{\sum_{j=1}^{ns} \alpha_{ij}\chi_j \Delta_{ij}^{(2)}} \right) \tag{18}$$

where k_B is the Boltzmann constant and α_{ij} is defined as:

$$\alpha_{ij} = 1 + \frac{[1 - (M_i/M_j)][0.45 - 2.54(M_i/M_j)]}{[1 + (M_i/M_j)]^2} \tag{19}$$

The expression for the rotational thermal conductivity is:

$$k_{rot} = k_b \sum_{i=mol} \frac{\chi_i}{\sum_{j=1}^{ns-1} \chi_j \Delta_{ij}^{(1)}} \tag{20}$$

and the vibrational-electronic thermal conductivity is:

$$k_{vib} = k_b \frac{C_{v,vib}}{R_s} \sum_{i=mol} \frac{\chi_i}{\sum_{j=1}^{ns-1} \chi_j \Delta_{ij}^{(1)}} \tag{21}$$

32

Note that $C_{v,vib}$ in the above expression is evaluated using the CEA database. The mixture translational-rotational thermal conductivity is then given by the sum of each energy mode as:

$$k = k_{tr} + k_{rot} \tag{22}$$

The collision terms are defined as:

$$\Delta_{ij}^{(1)} = \frac{8}{3} \left[\frac{2M_i M_j}{\pi R T (M_i + M_j)} \right]^{1/2} 10^{-20} \pi \Omega_{ij}^{(1,1)} \tag{23}$$

and

$$\Delta_{ij}^{(2)} = \frac{16}{5} \left[\frac{2M_i M_j}{\pi R T (M_i + M_j)} \right]^{1/2} 10^{-20} \pi \Omega_{ij}^{(2,2)} \tag{24}$$

where the collision integrals $\pi \Omega_{ij}^{m,n}$ are the weighted average cross-section of a collision between species i and j [40]. The constant 10^{-20} converts to square meters from square Angstroms. The evaluation of the collision integrals can be obtained through a variety of methods. The recommended evaluation methods are given in Reference [126], which provides a complete set of collision integrals for the computation of transport properties.

3.2.5 Source Terms.

The source terms appear in the species mass (Equation 1) and vibrational-electronic-electron energy (Equation 4) conservation equations. The formulation of the species mass production rates due to chemical reactions, w_s, and the vibrational energy source term, w_v, are discussed here.

Chemical Reactions.

The species mass production rate source terms are derived from the chemical reactions that occur in the gas. Due to the high freestream enthalpies and velocities

of these flows, some degree of chemical nonequilibrium was expected in the post-shock conditions. Hence, a 20-species, 40 reaction finite-rate chemistry model for reacting air that includes carbon species is used in this work. The species considered in the model are N_2, O_2, NO, CO_2, CO, C_2, C_3, CN, NO^+, N_2^+, O_2^+, CO^+, Ar, C, N, O, N^+, O^+, C^+, and e^-. The chemical production rate of species s in reaction q can be represented generally as [31, 107]:

$$w_{s,q} = (\beta_{sq} - \alpha_{sq}) \left[k_{f,q} \prod_j \left(\frac{\rho_j}{M_j} \right)^{\alpha_{sq}} - k_{b,q} \prod_j \left(\frac{\rho_j}{M_j} \right)^{\beta_{sq}} \right] \tag{25}$$

where α and β are the stoichiometric coefficients for each reaction. The source terms in the species mass conservation equation are given by:

$$w_s = M_s \sum_q w_{s,q} \tag{26}$$

Each reaction is governed by forward and backward reaction rate coefficients, $k_{f,q}$ and $k_{b,q}$, respectively. The forward reaction rates are calculated using an Arrhenius equation:

$$k_{f,q} = A_{f,q} T_{f,q}^{n_{f,q}} \exp\left(-D_{f,q}/T_{f,q}\right) \tag{27}$$

where the constants $A_{f,q}$, $n_{f,q}$ and $D_{f,q}$ are experimentally determined. Most of the chemical reactions used Park rates with reaction coefficients determined in air where applicable. However, a majority of the rate coefficients for the reactions involving carbon species were determined assuming a Martian atmosphere. The 40 reactions considered are listed in Table 4. The reactions involving C_3 were not considered in any of the references attributable to Park, but under strong sublimation conditions these reactions become important. Following the work of Candler [23], the dissociation, oxidation, and nitridation reactions for C_3 were included. Candler showed the

formation of C_3 does not become appreciable until the surface temperature reaches approximately 3000 K for an equilibrium air-carbon mixture.

The backward reaction rates are obtained from:

$$k_{b,q} = \frac{k_{f,q}}{K_{eq,q}} \tag{28}$$

where $K_{eq,q}$ is the concentration-based equilibrium constant for reaction q. The concentration-based equilibrium constant is calculated using the activity-based equilibrium constant $K_{a,q}$:

$$K_{eq,q} = K_{a,q} \left(\frac{p_0}{RT} \right)^{\nu_{gq}} \tag{29}$$

where the net stoichiometric exponent ν_{gq} considers only the gas species in reaction q:

$$\nu_{gq} = \sum_{k=1}^{K_g} \left(\nu_{kq}^{''} - \nu_{kq}^{'} \right) \tag{30}$$

The activity-based equilibrium constant is computed using Gibbs free energy minimization and the NASA CEA curve fits for enthalpy and entropy:

$$K_{a,q} = \exp\left[\frac{-\Delta G_q^{\circ}(T)}{RT} \right] = \exp\left[-\sum_{k=1}^{K} \nu_{kq} \left(\frac{H_k(T)}{RT} - \frac{S_k(T)}{R} \right) \right] \tag{31}$$

where $G_q^{\circ}(T)$ is Gibbs free energy and ν_{kq} is the net stoichiometric for species k in reaction q. The activity-based equilibrium constant can be calculated directly if the necessary thermodynamic functions are available for each species in the reaction. The US3D code uses the CEA thermodynamic database with a reference pressure of 10^5 Pa to compute the activity and concentration-based equilibrium constants.

For dissociation reactions, the forward rates should be governed by the translational-rotational and vibrational-electronic temperatures. The exact form of the temperature dependencies on the dissociation rate is unknown, but a few theories have been

postulated in the literature. Hammerling et al. [41] developed the coupled vibration dissociation (CVD) model where dissociation rate expressions were derived for a rotationless harmonic oscillator with vibrational levels populated according to a Boltzmann distribution. The CVD model provides a dissociation rate that is a function of T and T_v, but proved to be inadequate because the vibrational energy removed by dissociation was neglected. Park [92] suggested that the dissociation rate is governed by a geometric average between the translational-rotational and the vibrational-electronic temperatures:

$$T_a = \sqrt{TT_v} \tag{32}$$

This average temperature accounts for vibration-dissociation coupling [91]. A more general expression is also typically used:

$$T_a = T_v^q T^{1-q} \tag{33}$$

where the parameter q is taken to be somewhere between 0.3 and 0.5. Park notes that the CVD rate can be approximately reproduced when $q = 0.3$, but this value may underestimate the influence of the vibrational temperature [91]. Previous work has also shown that radiative heating calculations are extremely sensitive to the choice of q. Hartung [42] showed that a q of 0.5 produced a peak radiative heating value that was double that of choosing q equal to 0.3. The US3D code employs Equation 32 to govern the dissociation rate and is used for the simulations presented in this dissertation. Yet, the choice of q is acknowledged as an uncertain parameter.

Additionally, a kinetics model proposed by Johnston et al. [46] that mainly modifies the Park CO and CO_2 dissociation rates was also used. Particular to this study, the CO dissociation rate is increased by a factor of 13 compared to the Park rate. For

Table 4. Reactions and rate coefficients for the gas-phase chemistry model.

q	Reaction	$A_{f,q}$	$n_{f,q}$	$D_{f,q}$	$T_{f,q}$	Third Body, M	Ref.
1	$CO_2 + M \leftrightarrow CO + O + M$	1.4e+19	-1.50	6.328e+4	T_a	C, N, O, N+, O+, C+	[96]
		6.9e+17	-1.50	6.328e+4	T_a	Ar	[96]
		6.9e+18	-1.50	6.328e+4	T_a	others	[96]
2	$CO + M \leftrightarrow C + O + M$	3.4e+17	-1.00	1.29e+5	T_a	C, N, O, N+, O+, C+	[96]
		2.3e+16	-1.00	1.29e+5	T_a	Ar	[96]
		2.3e+17	-1.00	1.29e+5	T_a	others	[96]
3	$N_2 + M \leftrightarrow N + N + M$	3.0e+19	-1.60	1.132e+5	T_a	C, N, O, N+, O+, C+	[93]
		3.0e+21	-1.60	1.132e+5	T_a	e^-	[93]
		7.0e+18	-1.60	1.132e+5	T_a	others	[93]
4	$O_2 + M \leftrightarrow O + O + M$	1.0e+19	-1.50	5.95e+4	T_a	C, N, O, N+, O+, C+	[93]
		2.0e+18	-1.50	5.95e+4	T_a	others	[93]
5	$NO + M \leftrightarrow N + O + M$	1.1e+14	0.00	7.55e+4	T_a	C, N, O, N+, O+, C+, NO, CO_2	[93]
		5.0e+12	0.00	7.55e+4	T_a	others	[93]
6	$C_2 + M \leftrightarrow C + C + M$	3.7e+11	0.00	6.99e+4	T_a	All	[96]
7	$CN + M \leftrightarrow C + N + M$	2.5e+11	0.00	8.774e+4	T_a	All	[97]
8	$C_3 + M \leftrightarrow C_2 + C + M$	3.7e+11	0.00	6.99e+4	T_a	All	[23]
9	$N + e^- \leftrightarrow N^+ + e^- + e^-$	2.5e+31	-3.82	1.682e+5	T_v		[97]
10	$O + e^- \leftrightarrow O^+ + e^- + e^-$	3.9e+30	-3.78	1.585e+5	T_v		[93]
11	$C + e^- \leftrightarrow C^+ + e^- + e^-$	3.7e+28	-3.00	1.307e+5	T_v		[97]
12	$NO + O \leftrightarrow O_2 + N$	8.4e+9	0.00	1.94e+4	T		[93]
13	$N_2 + O \leftrightarrow NO + N$	6.4e+14	-1.00	3.84e+4	T		[93]
14	$CO + O \leftrightarrow O_2 + C$	3.9e+10	-0.18	6.92e+4	T		[96]
15	$CO + C \leftrightarrow C_2 + O$	2.0e+14	-1.00	5.80e+4	T		[96]
16	$CO + N \leftrightarrow CN + O$	1.0e+11	0.00	3.86e+4	T		[96]
17	$N_2 + C \leftrightarrow CN + N$	1.1e+11	-0.11	2.32e+4	T		[96]
18	$CN + O \leftrightarrow NO + C$	1.6e+10	0.10	1.46e+4	T		[96]
19	$CN + C \leftrightarrow C_2 + N$	5.0e+10	0.00	1.30e+4	T		[96]
20	$CO_2 + O \leftrightarrow O_2 + CO$	2.1e+10	0.00	2.78e+4	T		[96]
21	$C_2 + C_2 \leftrightarrow C_3 + C$	3.0e+19	0.00	0.00	T		[23]
22	$O + C_3 \leftrightarrow CO + C_2$	3.0e+10	0.00	0.00	T		[23]
23	$N + C_3 \leftrightarrow C_2 + CN$	3.0e+9	0.00	0.00	T		[23]
24	$N + O \leftrightarrow NO^+ + e^-$	5.3e+9	0.00	3.19e+4	T		[92]
25	$N + N \leftrightarrow N_2^+ + e^-$	2.0e+10	0.00	6.75e+4	T		[92]
26	$O + O \leftrightarrow O_2^+ + e^-$	1.1e+10	0.00	8.06e+4	T		[92]
27	$C + O \leftrightarrow CO^+ + e^-$	8.8e+5	1.00	3.31e+4	T		[96]
28	$O^+ + N_2 \leftrightarrow N_2^+ + O$	9.0e+8	0.36	2.28e+4	T		[92]
29	$O^+ + NO \leftrightarrow N^+ + O_2$	1.4e+2	1.90	1.53e+4	T		[92]
30	$NO^+ + O_2 \leftrightarrow O_2^+ + NO$	2.4e+10	0.41	3.26e+4	T		[92]
31	$NO^+ + N \leftrightarrow N_2^+ + O$	7.2e+10	0.00	3.55e+4	T		[92]
32	$NO^+ + O \leftrightarrow N^+ + O_2$	1.0e+9	0.50	7.72e+4	T		[92]
33	$O_2^+ + N \leftrightarrow N^+ + O_2$	8.7e+10	0.14	2.86e+4	T		[92]
34	$O_2^+ + N_2 \leftrightarrow N_2^+ + O_2$	9.9e+9	0.00	4.07e+4	T		[92]
35	$O_2^+ + O \leftrightarrow O^+ + O_2$	4.0e+9	-0.09	1.80e+4	T		[92]
36	$NO^+ + N \leftrightarrow O^+ + N_2$	3.4e+10	-1.08	1.28e+4	T		[92]
37	$NO^+ + O \leftrightarrow O_2^+ + N$	7.2e+9	0.29	4.86e+4	T		[92]
38	$O_2 + C^+ \leftrightarrow O_2^+ + C$	1.0e+10	0.00	9.40e+3	T		[96]
39	$CO + C^+ \leftrightarrow CO^+ + C$	1.0e+10	0.00	3.14e+4	T		[96]
40	$NO^+ + C \leftrightarrow NO + C^+$	1.0e+10	0.00	2.32e+4	T		[96]

Table 5. Park gas-phase chemistry rate modifications made by Johnston et al. [46]

Reaction	Multiplication Factor
$CO_2 + M \leftrightarrow CO + O + M$	2
$CO + M \leftrightarrow C + O + M$	13
$CN + O \leftrightarrow NO + C$	0.1
$CN + C \leftrightarrow C_2 + N$	3.2
$CO_2 + O \leftrightarrow O_2 + CO$	6

this model, Johnston et al. [46] made modifications based on comparisons with shock tube radiation measurements under Mars re-entry conditions in the NASA EAST facility. Table 5 lists a summary of the reaction rate modifications. Brandis et al. [20] found this kinetics model improved nonequilibrium radiance predictions compared to the standard Park gas-phase chemistry model with experiments conducted in EAST.

Vibrational Energy.

The vibrational energy source term is given by:

$$w_v = Q_{c-v} + \sum_s Q_{T-v,s} \tag{34}$$

where Q_{c-v} represents the amount of vibrational-electronic energy added or removed due to chemical reactions. The Q_{c-v} source term can be defined with a preferential or non-preferential model for dissociation. The non-preferential model assumes that molecules are created or destroyed at the average vibrational energy. The preferential model assumes that molecules are more likely to dissociate at higher vibrational energy levels, which tends to suppress the vibrational energy and dissociation rate. The amount of energy added or removed is typically set to an arbitrary fraction (usually 0.3) of the dissociation energy. However, the energy removal rate must be consistent with the details of the vibration-dissociation coupling model [84]. The two-temperature model used in US3D is not based on a detailed representation of

the dissociation process, so it is impossible to derive an expression for the vibrational energy added or removed by dissociation [23]. Therefore, the non-preferential model for Q_{c-v} is used and defined as:

$$Q_{c-v} = \sum_s w_s e_{v,s} \tag{35}$$

Preferential models have been developed and studied in the past where the energy contained in the upper vibrational levels was accounted for in the dissociation process [117, 65, 109]. However, these models are computationally intensive and not often implemented in CFD codes.

The $Q_{T-v,s}$ term is the energy exchange rate between the vibrational-electronic and translational-rotational energy modes. It is assumed to be modeled by a single exchange rate due to the fast energy transfer between the translation-rotational and vibrational-electronic modes [92]. The rate of change in vibrational state population levels can be described by the Landau-Teller formulation where it is assumed that molecules behave as harmonic oscillators and the vibrational level can only change one quantum level at a time [120]. The single energy exchange rate for each species is:

$$Q_{T-v,s} = \rho_s \frac{e_{v,s}(T) - e_{v,s}(T_v)}{\tau_s} \tag{36}$$

where $e_{v,s}$ is the vibrational energy evaluated either at the local translational-rotational temperature or at the local vibrational-electronic temperature. Again, the internal vibrational energy is computed using the CEA database. The relaxation time, τ_s, is defined as:

$$\tau_s = <\tau_{s,LT}> + \tau_{cs} \tag{37}$$

where $<\tau_{s,LT}>$ is the molar averaged Landau-Teller relaxation time [54] and τ_{cs} is

the collision limited relaxation time. The molar averaged relaxation time is given as:

$$< \tau_{s,LT} >= \frac{\sum_r \chi_r}{\sum_r \chi_r / \tau_{sr}} \tag{38}$$

where τ_{sr} is the Landau-Teller inter-species relaxation time and is modeled using curve fits developed by Millikan and White [72] as:

$$
\begin{aligned}
\tau_{sr} &= \frac{1}{p} \exp\left[A_{sr}\left(T^{-1/3} - 0.015\mu_{sr}^{1/4}\right) - 18.42\right], \quad p \text{ in atm,} \\
A_{sr} &= 1.16 \times 10^{-3} \mu_{sr}^{1/2} \theta_{v,s}^{4/3} \\
\mu_{sr} &= M_s M_r / \left(M_s + M_r\right)
\end{aligned}
\tag{39}
$$

The relaxation time in Equation 36 would calculate a relaxation rate unrealistically large at high temperatures due to an over prediction of the collision cross-section if only the Landau-Teller rate expression from Millikan and White was used [22]. Park [92] corrected this problem by introducing a collision limited relaxation time, τ_{cs}, which is written as:

$$\tau_{cs} = \frac{1}{\sigma_v c_s N} \tag{40}$$

where N is the number density of the mixture, c_s is the average molecular speed of species s given as:

$$c_s = \sqrt{\frac{8RT}{\pi M_s}} \tag{41}$$

and σ_v is the limiting cross section given by:

$$\sigma_v = \sigma_{vs} \left(\frac{50,000}{T}\right)^2 \quad \text{m}^2 \tag{42}$$

where σ_{vs} is the limiting cross section for species s. This expression was originally developed for nitrogen, so most molecules default to the limiting cross section of

Table 6. Limiting cross sections for different gas species [93, 96].

Molecular Species	σ_{vs} (m^2)
N$_2$	3×10^{-21}
NO	3×10^{-21}
O$_2$	3×10^{-21}
CO	3×10^{-22}
CO$_2$	1×10^{-20}

nitrogen if not specified. Table 6 provides the limiting cross sections used in US3D.

3.2.6   Numerical Methods.

The numerical methods utilized in US3D are similar to those used in the NASA Ames DPLR Navier-Stokes solver [127, 128] because US3D was originally intended to be a follow-on to that code. US3D shares many of the same numerics and has also been extensively validated against the NASA DPLR code on a wide variety of test problems [43]. The compressible Navier-Stokes equations that also account for internal energy relaxation and finite-rate chemical kinetics are solved in US3D using the finite-volume formulation. Convective fluxes are calculated using the modified Steger-Warming flux vector splitting method for steady-state simulations. For unsteady simulations, low-dissipation centrally differenced fluxes are available with second, fourth, and sixth order spatial accuracy. There are first, second, and third order accurate explicit and implicit time integration methods. The MUSCL scheme with a pressure limiter is used to limit overshoots and prevent non-physical values in regions with strong shocks. Cell-centered gradients are calculated using a weighted-least-squares reconstruction of the primitive variables while viscous fluxes are calculated using a deferred-correction approach. The data parallel line relaxation numerical method is used along lines of cells normal to walls for rapid convergence to steady-state. However, the full matrix point relaxation numerical method is used in regions where lines

cannot be formed. US3D incorporates a generalized set of boundary conditions including catalytic and partially-catalytic walls with and without radiative equilibrium, wall blowing and suction, subsonic inflow and outflow conditions, and slip wall conditions for rarefied flow applications. The next section will discuss how an ablating wall boundary condition is implemented in US3D.

3.3   Ablation Modeling

3.3.1   Past Work.

Using carbon as a TPS material for re-entry applications has been extensively examined. Most of the early research almost exclusively focused on the oxidation rate of carbon under various surface temperatures and pressures. The experimental data always assumed that the oxidation process followed a rate law in an Arrhenius form:

$$\dot{m} = Ap^n \exp\left(-E_a/RT\right) \tag{43}$$

where A is a pre-exponential coefficient, p is the surface pressure, E_a is the activation energy, R is the universal gas constant, and T is the surface temperature. Note that $\dot{m}$ is a function of the pressure to the power n, the order of the reaction. However, huge scatter was seen in the experimental data, and there were varying levels of reasoning for why one data set was different from another. Scala [105] attempted to specify a set of kinetic parameters that best bracketed the data, which spanned a reaction rate range of four orders of magnitude. Unfortunately, all of the data used by Scala was obtained below a surface temperature of 1373 K, and linear extrapolation of simple Arrhenius expressions to higher temperatures is known to predict oxidation rate probabilities exceeding those theoretically possible [62].

Maahs [62] compiled high temperature data from many sources to demonstrate
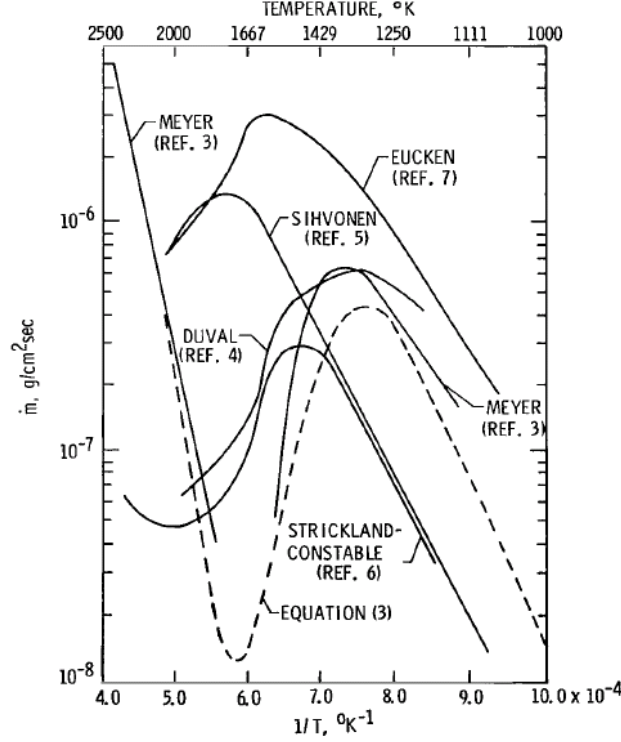
Figure 12. Arrhenius plot of carbon mass loss rate for a carbon filament-oxygen reaction at $p = 1.33$ Pa [62].

the non-linear behavior of carbon oxidation. Figure 12 shows the mass loss rate due to oxidation from a carbon filament-oxygen reaction at $p = 1.33$ Pa. The dashed line in the figure represents a kinetic expression developed by Blyholder et al. [16] that described the surface as having two types of reaction sites, one being more reactive than the other. Although not shown in Figure 12, the experiments of Rosner and Allendorf [102, 103] have also shown the oxidation rate in an Arrhenius plot to be non-linear. The mass loss rates differ by orders of magnitude, and the curves exhibit maxima and minima. Some of the differences can be attributed to the diversity of carbon materials used in the experiments (i.e. impurities, porosities, structure, etc.). Clearly, a simple linear Arrhenius expression cannot be expected to adequately describe the oxidation process that would span a wide temperature and pressure range.

43

Many researchers have attempted to theoretically and empirically derive kinetic expressions for carbon oxidation at high temperatures. Both Blyholder et al. [16] and Strickland-Constable et al. [78] used a surface model that assumed reaction sites could be classified into a more reactive A-site and a less reactive B-site. At low temperatures, the oxidation rate was dominated by the A-sites. As the temperature rose, the A-sites thermally annealed to form less reactive B-sites. The B-sites created A-sites as they oxidized and desorbed CO. It was the competition between the generation and deactivation of both these reaction sites that resulted in observed maximums in the oxidation rate [58]. An important assumption to note was that CO was the primary product. Ong [85] used transition-state theory to deduce a set of controlling kinetic steps, calculating required transition energies by statistical thermodynamics, and empirically determining several constants from high temperature oxidation data. Ong's rate expression only assumed one type of active site on the carbon surface. A contrasting feature from the Blyholder and Strickland-Constable models was that Ong considered two product species from the carbon-oxygen reaction, CO_2 at low temperatures and CO at higher temperatures. A rate maximum was also predicted by Ong's model, which was attributed to a change in the vibration chemical potential of molecular oxygen.

None of the aforementioned kinetic models accurately predict oxidation rates because they rely on linear Arrhenius expressions. A gas-surface reaction can be very complex considering there may be a large number of separate, competing kinetic steps involved. These include adsorption, surface migration, chemical bonding with a carbon atom, and desorption of the gaseous product. One of these steps may be of greater or lesser importance because the apparent activation energy and/or steric factor may change as the surface temperature and pressure changes. Therefore, while it may be possible to correlate kinetic data with a simple Arrhenius expression over

a narrow range of temperatures and pressures, such an expression cannot be applied with reliability outside that range [62].

Much uncertainty remains in predicting mass loss rates due to sublimation processes. Sublimation is known to be the primary mass loss mechanism for surface temperatures above approximately 3000 K. The sublimation regime has typically been defined as the range of conditions where the mass loss due to vaporization exceeds the diffusion-controlled oxidation mass loss rate [106]. In order to predict these rates, thermodynamic databases are commonly used to calculate transport properties of individual chemical species at a given temperature. However, previous research has shown that these databases predict large variations in carbon sublimation rates. Milos and Chen [73] compared the JANAF [1] and CEA [70] thermodynamic databases and found that C_3 and C_5 contained large discrepancies. The C_3 disagreement was troublesome because this is the primary species present for carbon sublimation and is critical for the prediction of ablation rates. Havstad and Ferencz [44] recommended the addition of C_5 and C_7 sublimation into the nonequilibrium chemistry model for a more accurate ablation rate prediction when surface temperatures are greater than approximately 3900 K.

Gosse et al. [36] compared equilibrium ablation profiles from the CEA database and other researchers who have attempted to improve the equilibrium vapor pressures of carbon gas species. Figure 13 shows equilibrium ablation, or B' curves, for different thermochemical models in the sublimation regime. The divergence in predicted ablation rates becomes more severe as surface temperatures rise above 3400 K, which highlights the discrepancy between the different thermochemical models. Additionally, Gosse et al. [36] compared the pressure-temperature phase change diagram for a graphite system again using values from CEA and equilibrium vapor pressures given by nonequilibrium sublimation models for carbon. Figure 14 shows a large variation
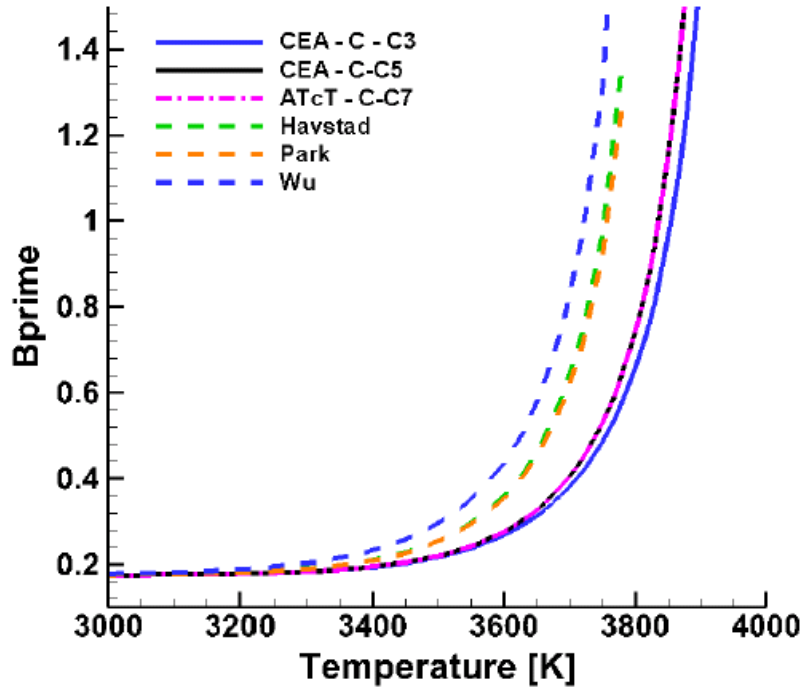
Figure 13. Equilibrium ablation rate curves from the NASA CEA database and equilibrium vapor pressures from selected finite-rate chemistry models [36].
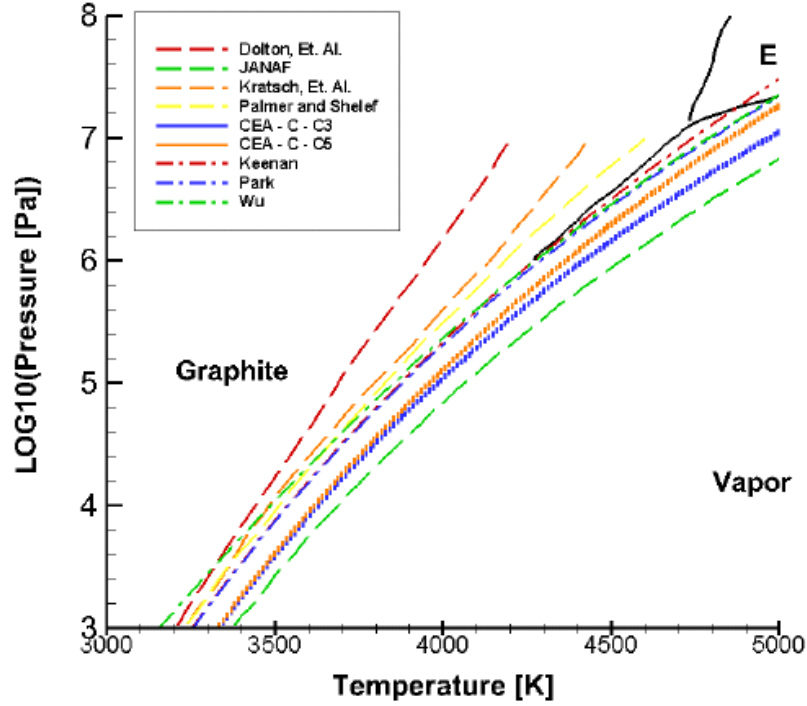
Figure 14. Graphite pressure-temperature phase change diagram comparing different thermodynamic data [36].

between the predicted pressure-temperature at which carbon would sublimate. The CEA database, which is currently assumed to give the best thermodynamic values, does not line up with the graphite to vapor phase change.

3.3.2 Equilibrium: B' Curve for Air-Carbon.

A common approximation to account for the effects of ablation products being released into the gaseous flow field, and accompanying surface blowing that occurs, is to employ a blowing correction term, B', that is based on boundary layer theory and mass balance at the surface. Consider a mixture of air and carbon in the gas-phase interacting with a surface of solid carbon. The mass flux of carbon gas, $\dot{m}_c$, from the wall is:

$$\rho_w D_c \nabla y_c \Big|_w + \dot{m}_c = y_{c,w} \dot{m}_c \tag{44}$$

where y_c is the total mass fraction of gaseous carbon and the subscript w represents the wall state.

Now assume that the heat/mass transfer analogy holds such that $C_M = C_H$ with unity Prandtl/Lewis numbers and equal species diffusion. Using the definition of the blowing and heat transfer coefficients, it can be shown that B' is given by:

$$B' = \frac{\dot{m}}{\rho_e v_e C_M} \approx \frac{\dot{m}}{\rho_e v_e C_H} = \frac{y_{c,w}}{1 - y_{c,w}} = \frac{y_{c,w}}{y_{a,w}} \tag{45}$$

where the subscript e represents boundary layer edge conditions and $y_{a,w}$ is the mass fraction of air species at the wall conditions. Thus, B' is the ratio of the mass fraction of gaseous carbon species to air species at the local wall conditions [23]. MacLean [63] showed that the blowing correction can be adjusted to match experimental data using the expression:

$$\frac{C_H}{C_{H,0}} = \frac{2\lambda B'}{e^{2\lambda B'} - 1} \tag{46}$$

where $C_{H,0}$ is the non-blowing heat transfer coefficient and λ is an empirical parameter that can be tailored for the expected output.

To obtain the equilibrium saturated state for an air-carbon mixture at a given pressure and temperature, bulk carbon is added to air until the carbon starts to condense to a solid. That condensation point gives the equilibrium value for B'. Figure 15a plots B' for an air-carbon mixture as function of temperature for several pressures. At low temperatures, air reacts with carbon to produce CO_2, which results in a plateau at $B' = 0.089$. In the next temperature regime, CO is the dominant reaction product due to reactions of atomic oxygen with carbon. The rate of ablation increases until all of the oxygen is consumed resulting in a value of $B' = 0.178$. As the surface temperature continues to increase, the solid carbon begins to sublime directly to gaseous carbon. The B' of this process increases exponentially as the surface temperature approaches and passes the equilibrium vapor pressure of the carbon gas mixture.

Figure 15b plots the composition of the saturated air-carbon mixture at a pressure of 1 atm. For surface temperatures below 2500 K, the gas is a simple mixture of N_2, CO, and CO_2. Above 2500 K, appreciable quantities of CN start to form. As sublimation becomes stronger, the surface chemical state becomes complicated as many polyatomic carbon and nitrogen species are formed. The primary species formed in order of concentration level are C_3, C_5, CN, C_2, C_4, and then C.

Many ablation modeling approaches use B' to obtain the gas-solid interface boundary condition [76, 8, 26, 73, 63]. For each gas-surface boundary of the CFD grid, the surface temperature, pressure, and existing gas-phase composition are used as input variables. The resulting saturated air-carbon composition provides mass fractions of all gaseous species that are injected into the flow. The new mass fractions are set as explicit boundary conditions [63]. The gas blowing rate $\dot{m}$ is then found using
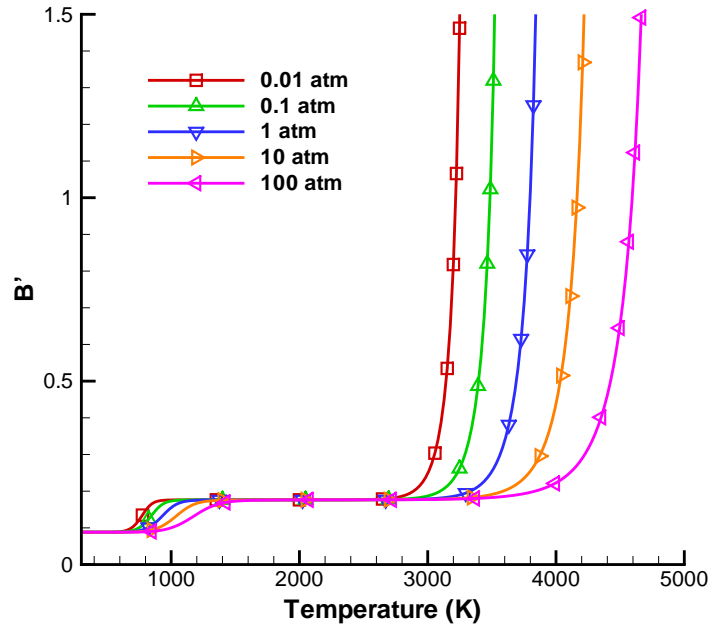
(a) B' for air-carbon as function of temperature and pressure.
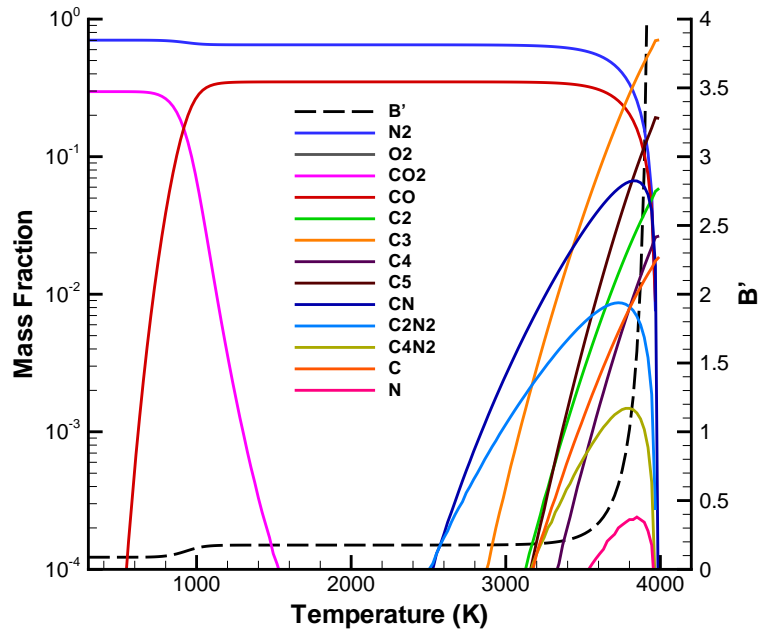
(b) Mass fractions and B' at 1 atm pressure.

Figure 15. Equilibrium saturated air-carbon mixture composition and dimensionless blowing rate.

Equation 44. The heat flux can also be reduced using B' through Equation 46 to account for the effect of ablation.

3.3.3 Finite-Rate Surface Reaction Formulation.

The nonequilibrium, finite-rate gas-surface interaction system model utilized in this work follows the formulation developed by Marschall and MacLean [67] and MacLean et al. [64]. A summary of the derivation is presented to provide information necessary to follow the implementation discussion in the next section. Please refer to the identified references for more information. The model consists of three environments that can exist at the gas-surface interface:

1. Gas environment

2. Surface environment

3. Bulk environment

The gas environment is a single phase containing all the gas species. The surface environment can have multiple phases, each occupying a fraction of the total surface area. Each surface phase consists of one or more sets of "active sites" where surface reactions can occur. Each set of active sites has an associated set of chemically-distinct species. The surface species can include open or available sites and chemically adsorbed species. The total number of open and occupied sites for each set is conserved. The bulk environment can also have multiple phases with each representing a different material or constituent. Each bulk phase (i.e. solid phase) is associated with a unique set of chemical species that can participate in surface reaction processes as would occur with a re-entry vehicle undergoing ablation [64]. All reactions must occur at active sites on the surface and involve open and/or occupied sites. Note that the same atom or molecule is treated as a distinct chemical species when in the gas

50

or surface phase. The different environments recognize that surface reactions occur with chemical species in different chemical states (i.e. gas, adsorbed, bulk), which provides the flexibility to specify rate parameters in an appropriate manner.

A surface reaction should involve surface species to include interactions with each other and/or species from the gas and bulk environments. Additionally, surface reactions must involve empty and/or filled sites. The following surface reaction types can be defined where (s) denotes an open active site, $A(s)$ denotes an adsorbed species on the surface, and $A(b)$ denotes a bulk phase species:

- Adsorption/desorption $\qquad A + (s) \leftrightarrow A(s)$

- Eley-Rideal (ER) $\qquad A + B(s) \leftrightarrow AB + (s)$

- Langmuir-Hinshelwood (LH) $\qquad A(s) + B(s) \leftrightarrow AB + 2(s)$

- Oxidation/reduction $\qquad A + (s) + B(b) \leftrightarrow AB + (s)$

- Sublimation/condensation $\qquad (s) + A(b) \leftrightarrow A + (s)$

The only bulk phase material considered in this work was that of carbon, so the number of bulk species is equal to one. The production or loss of any species comes from the summation of the forward and backward rate processes for each reaction. The procedure is analogous to the finite-rate formulation for the gas phase chemistry discussed in Section 3.2.5, except species production occurs at the surface and the rate is per unit surface area per unit time (e.g. kmol m^{-2} s^{-1}). The forward and backward rate coefficients are related through an equilibrium constant, which can be obtained in three ways:

1. Specifying individual Gibbs free energies for each species

2. Explicitly specifying the equilibrium constant by use of a curve fit (i.e. Equation 31) or a direct expression
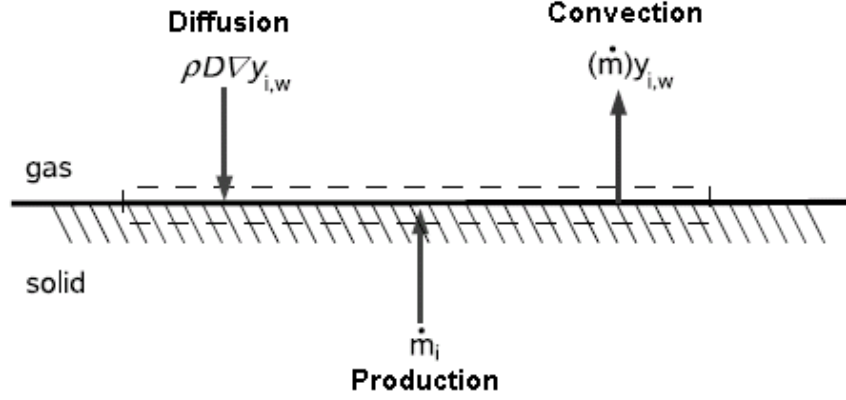
Figure 16. Surface mass balance.

3. Specifying forward and backward reaction rate coefficients

The reaction flux, r_i, for reaction i is given by:

$$r_i = k_{fi} \prod_{k=1}^{K} X_k^{\nu'_{ki}} - k_{bi} \prod_{k=1}^{K} X_k^{\nu''_{ki}} \qquad (47)$$

where k_{fi} and k_{bi} are the forward and backward reaction rate coefficients for reaction i at a given temperature, ν'_{ki} is the reactant stoichiometric coefficient for species k, ν''_{ki} is the product stoichiometric coefficient for species k, and X_k is a generalized concentration of species k. The concentration of species k is usually calculated as ρ_k/M_k as shown in Equation 25. The reaction flux is given in units of (kmol m^{-2} s^{-1}). The net production rate of species k is:

$$w_k = \sum_{i=1}^{NR} (\nu_{ki} r_i) \qquad (48)$$

where $\nu_{ki} = (\nu''_{ki} - \nu'_{ki})$ and NR represents the total number of reactions involving species k. The chemical source term in Equation 48 applies to any species at the gas-surface interface.

Mass balance at the surface is used to set the boundary condition for each species in the gas phase by considering the fluxes of mass entering and leaving an infinitely thin control volume fixed at the surface as shown in Figure 16. The surface mass balance for species k, with the assumption that no material is being removed due to mechanical erosion (spallation), can be written as:

$$\rho_w D_k \nabla y_k \bigg|_w + M_k w_k = \rho_w v_w y_{k,w} \tag{49}$$

where y_k is the species mass fraction and v_w is the surface normal velocity. The terms on the left-hand side of Equation 49 represent the mass fluxes entering the surface due to diffusion and species production from surface reactions. These mass fluxes are exactly balanced by the terms on the right-hand side that represent the rate at which the mixture is convected away from the surface due to ablation. Equation 49 represents the rate at which the mass of each gas phase species changes at the surface [64].

3.3.4 Surface Equilibrium Constants.

Calculation of the reaction flux r_i in Equation 47 requires the specification of two of the three quantities: k_{fi}, k_{bi}, or K_{eq}. Typically, the forward rate coefficient is specified, and the backward rate coefficient is calculated using the equilibrium constant. The calculation of equilibrium constants for surface reactions requires thermodynamic data for each surface and gas phase species in the reaction. If the backward rate coefficient is specified, the concentration-based equilibrium constant can be calculated directly using Equation 28. Otherwise, it can be computed using the activity-based equilibrium constant as shown in Equation 29. In the calculation of the activity-based equilibrium constant, the enthalpy and entropy are not available for species in the surface phase, so equilibrium constant expressions are specified directly for the

53

adsorption/desorption reactions.

The adsorption/desorption equilibrium constants are expressed in dimensionless activity-based form and depend on the type of adsorption (mobile or immobile). For mobile adsorption, the adsorbed species remains in a gaseous state and acts as a two-dimensional gas over the surface. It is common to assume that mobile adsorption has no activation energy since there is a very weak van der Waals bond to the adsorption sites. The activity-based equilibrium constant is given by:

$$K_{a,m} = \frac{p_0}{BkT} \left(\frac{2\pi m_i kT}{h^2} \right)^{-1/2} \exp \left(\frac{T_{des}}{T} \right) \tag{50}$$

where p_0 is a reference pressure of 10^5 Pa, $m_i = m_O$ or m_N, h is the Planck constant, and T_{des} is related to the desorption energy by $E_{des} = RT_{des}$. The surface site concentration B represents the total number of available reaction sites given in m^{-2}. Substituting $k = R/A_v$ and $m_i = M_i/A_v$ gives:

$$K_{a,m} = \frac{A_v p_0}{BRT} \left(\frac{2\pi M_i RT}{A_v^2 h^2} \right)^{-1/2} \exp \left(\frac{T_{des}}{T} \right) \tag{51}$$

where A_v is Avogadro's number. For immobile adsorption, the adsorbed species stays wherever it was adsorbed until it desorbs or reacts with the bulk surface. This process requires an activation energy for the gas-phase species to overcome in order to bond to an adsorption site. The activity-based equilibrium constant is given by:

$$K_{a,im} = \frac{A_v p_0}{RT} \left(\frac{2\pi M_i RT}{A_v^2 h^2} \right)^{-3/2} \exp \left(\frac{T_{des}}{T} \right) \tag{52}$$

The activity-based equilibrium constant is converted to a concentration-based equilibrium using Equation 29. For an adsorption reaction, ν_g equals -1 and gives the

concentration-based equilibrium constant for mobile adsorption as:

$$K_{eq,m} = K_{a,m} \left(\frac{RT}{p_0} \right) = \frac{A_v}{B} \left(\frac{2\pi M_i RT}{A_v^2 h^2} \right)^{-1/2} \exp \left(\frac{E_{des}}{RT} \right) \tag{53}$$

and for immobile adsorption:

$$K_{eq,im} = K_{a,im} \left(\frac{RT}{p_0} \right) = A_v \left(\frac{2\pi M_i RT}{A_v^2 h^2} \right)^{-3/2} \exp \left(\frac{E_{des}}{RT} \right) \tag{54}$$

Marschall and MacLean [67] provided a general equation for the adsorption/desorption reactions that can be implemented into a CFD code:

$$K_{eq} = A_{eq} T'^\beta K_0 \exp \left(\frac{E_{des} - E_{ad}}{RT} \right) \tag{55}$$

where A_{eq} is a constant, β and T' are dimensionless ($T' \equiv T/1\,\mathrm{K}$), and E_{des} and E_{ad} are the activation energies for desorption and adsorption, respectively. Relating the above constants, it is shown that:

$$A_{eq} = \begin{cases} \dfrac{A_v}{B} & \text{mobile} \\[2ex] A_v & \text{immobile} \end{cases}$$

$$K_0 = \begin{cases} \left(\dfrac{2\pi M_i RT}{A_v^2 h^2} \right)^{-1/2} & \text{mobile} \\[2ex] \left(\dfrac{2\pi M_i RT}{A_v^2 h^2} \right)^{-3/2} & \text{immobile} \end{cases}$$

Therefore, the type of adsorption process is critical to characterizing the overall surface kinetic model. The sensitivity of the ablation process to the adsorption process is discussed in Chapter IV.

Table 7. Forward reaction rate formulas.

Type	Rate Formula	Specified Parameters
Arrhenius	$k_f = AT'^{\beta} \exp\left(-\dfrac{E}{RT}\right)$	A, β, E
Adsorption	$k_f = \left[\dfrac{\bar{\nu}_s}{4\Phi^{\nu_s}}\right] S_0 T'^{\beta} \exp\left(-\dfrac{E_{ad}}{RT}\right)$	S_0, β, E_{ad}
Eley-Rideal	$k_f = \left[\dfrac{\bar{\nu}_s}{4\Phi^{\nu_s}}\right] \gamma_{er} T'^{\beta} \exp\left(-\dfrac{E_{er}}{RT}\right)$	$\gamma_{er}, \beta, E_{er}$

3.3.5 Forward Reaction Rates.

Forward reaction rates must be specified for each surface reaction in the model. Please refer to Reference [67] for the rate formulas available for the different reaction types. The implemented surface models only use the Arrhenius, adsorption, and ER reaction types and the corresponding rate formulas are specified in Table 7.

The units of A in the Arrhenius formula vary depending on the type of reactants and stoichiometries involved. For example, the units of A would be (m^3 $kmol^{-2}$ s^{-1}) for a reaction involving one gas and one surface species. For a reaction involving two surface species, the units of A would be (m^2 $kmol^{-1}$ s^{-1}) . Finally, the units of A would be (s^{-1}) for a reaction involving one surface and one bulk species. The Arrhenius expression is the most general way to specify a forward reaction rate. The disadvantage of using the basic Arrhenius formulation is that the magnitudes of A and β are difficult to relate to physical, chemical, and kinetic processes [67]. However, kinetics-based formulations (i.e. adsorption, ER) provide a more intuitive way to specify surface reaction rates because they are describing physical processes occurring at the gas-surface interface.

The leading term in the brackets for the kinetics-based rates contains the following variables: Φ is the total active site density, ν_s is the site density exponent equal to the

sum of stoichiometric coefficients for all surface reactants, and $\bar{\nu}_s$ is the mean thermal velocity of the incoming reactant gas species:

$$\bar{\nu}_s = \sqrt{\frac{8RT}{\pi M_s}} \tag{56}$$

The sticking coefficient S_0 and ER reaction efficiency coefficient γ_{er} are dimensionless, and their values should lie between zero and one.

3.3.6 Park Model.

Two of the more common air-carbon surface models contained in the literature are from Zhluktov and Abe (ZA) [136] and Park. As MacLean et al. [64] point out, the simple Park model was actually first published by Chen and Milos [25]. This "Park model" is more or less a compilation of Park's published work on carbon ablation models [89, 90, 92, 95]. The surface reactions involved in the Park model are given as:

(1) $O + (s) + C(b) \rightarrow CO + (s)$

(2) $O_2 + 2(s) + 2C(b) \rightarrow 2CO + 2(s)$

(3) $N + (s) + C(b) \rightarrow CN + (s)$

(4) $3(s) + 3C(b) \rightarrow C_3 + 3(s)$

(5) $C_3 + 3(s) \rightarrow 3(s) + 3C(b)$
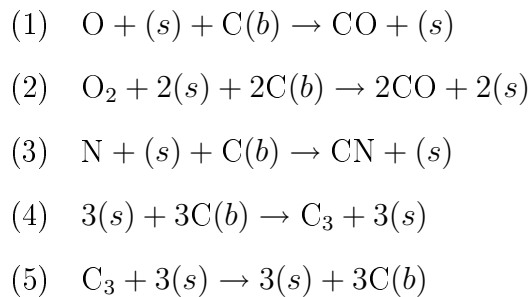
The above reaction set contains irreversible oxidation of both atomic and molecular oxygen, irreversible nitridation of atomic nitrogen, and C_3 sublimation. The reaction rates are based on kinetic theory [92] with experimentally determined reaction probabilities assigned for each surface reaction. The fluxes for each reaction

are:

$$r_1 = \rho_w y_O \bar{\nu}_O \gamma_1 \frac{M_C}{M_O} \tag{57}$$

$$r_2 = 2\rho_w y_{O_2} \bar{\nu}_{O_2} \gamma_2 \frac{M_C}{M_{O_2}} \tag{58}$$

$$r_3 = \rho_w y_N \bar{\nu}_N \gamma_3 \frac{M_C}{M_N} \tag{59}$$

$$r_4 = \rho_w y_{C_3,E} \bar{\nu}_{C_3} \gamma_4 \tag{60}$$

$$r_5 = \rho_w y_{C_3} \bar{\nu}_{C_3} \gamma_5 \tag{61}$$

Here, $\bar{\nu}_s$ is defined as $\sqrt{RT_w/2\pi M_s}$ and γ_i is the efficiency of surface reaction i. The reaction efficiencies are taken from the literature to be [89, 25]:

$$\gamma_1 = 0.63 \exp\left(\frac{-1160}{T_w}\right) \tag{62}$$

$$\gamma_2 = 0.5 \tag{63}$$

$$\gamma_4 = 1 \tag{64}$$

$$\gamma_5 = 0.1 \tag{65}$$

There has been a lot of recent work in determining the reaction probability or efficiency of carbon nitridation because it is considered as an important reaction for carbon-based TPS materials. The nitridation reaction contributes directly to the surface mass loss and radiative heating. The efficiency of this reaction published by Park and Bogdanoff [95] states that 30% of N atoms impacting the surface form CN. However, Driver and MacLean [28] found that an efficiency of 1×10^{-3} provides the best fit for recession data in arc jet tests. Zhang et al. [135] provides an excellent comparison of experimental work determining the nitridation efficiency, including their own, and found the efficiency to be about two orders of magnitude lower than that obtained by Park and Bogdanoff [95]. The experimental efficiencies generated

Figure 17. Experimentally determined reaction efficiency for carbon nitridation by atomic nitrogen from different investigators. Reproduced from Zhang et al. **[135]** and references cited in the plot refer to those contained in that article. The "o" symbols refer to the work performed by Zhang et al.

by Goldstein [33], Suzuki et al. [114, 116] and Zhang et al. [135] were all around 10^{-3} and showed a weak temperature dependence as shown in Figure 17. Suzuki et al. [115] proposed a nitridation efficiency based on their results as:

$$\gamma_{nit} = 8.441 \times 10^{-3} \exp\left(-\frac{2322}{T}\right) \tag{66}$$

The above efficiency expression fits nitridation data with surface temperatures ranging from 1351 to 2184 K. In this dissertation, results will be presented using the Park ablation model with a nitridation efficiency of 0.3 and with that specified by Equation 66.

The sublimation reactions are based on a Knudsen-Langmuir formulation for nonequilibrium surface evaporation where the C_3 concentration in Equation 60 is

59

computed from the saturated vapor pressure [8, 48]. The reaction flux then becomes:

$$r_4 = p_v \gamma_4 \sqrt{\frac{M_{C_3}}{2\pi R T_w}} \tag{67}$$

with the saturated carbon vapor pressure as:

$$p_v = 5.19 \times 10^{13} \exp\left(\frac{-93310}{T_w}\right) \tag{68}$$

Species mass conservation at the surface is then solved using Equation 49 with:

$$\rho_w v_w = \sum_{s=1}^{ns} \dot{m}_s \tag{69}$$

The source terms for each species are defined as:

$$\dot{m}_{CO} = (r_1 + r_2)\frac{M_{CO}}{M_C} \tag{70}$$

$$\dot{m}_{CN} = r_3 \frac{M_{CN}}{M_C} \tag{71}$$

$$\dot{m}_{C_3} = r_4 - r_5 \tag{72}$$

$$\dot{m}_N = -r_3 \frac{M_N}{M_C} \tag{73}$$

$$\dot{m}_O = -r_1 \frac{M_O}{M_C} \tag{74}$$

$$\dot{m}_{O_2} = -r_2 \frac{M_{O_2}}{2M_C} \tag{75}$$

and $\dot{m}_s = 0$ for all other species considered.

3.3.7 Zhluktov and Abe Model.

Considered one of the most advanced kinetic models for air-carbon gas-surface chemistry, the finite-rate Zhluktov and Abe [136] model involves 12 surface reactions with defined forward and backward rates that are thermodynamically constrained.

Table 8. Reaction set for the Zhluktov and Abe gas-surface chemistry model.

Reaction	Type	S_0 / γ_{er} / A	β	E (kJ mol^{-1})
1.) $O + (s) \leftrightarrow O(s)$	Ads	1	0	0
2.) $N + (s) \leftrightarrow N(s)$	Ads	1	0	0
3.) $2O(s) \leftrightarrow O_2 + 2(s)$	Arrh	3.58×10^{13}	1	256.07
4.) $O_2 + (s) \leftrightarrow O + O(s)$	ER	1	0	118.06
5.) $CO_2 + (s) \leftrightarrow CO + O(s)$	ER	0.9	0	0
6.) $O(s) + C(b) \leftrightarrow CO + (s)$	Arrh	2.08×10^9	1	332.56
7.) $O + O(s) + C(b) \leftrightarrow CO_2 + (s)$	ER	0.8	0	16.63
8.) $2O(s) + C(b) \leftrightarrow CO_2 + 2(s)$	Arrh	3.58×10^{17}	0	332.56
9.) $C + (s) \leftrightarrow (s) + C(b)$	ER	0.24	0	0
10.) $C_2 + 2(s) \leftrightarrow 2(s) + 2C(b)$	ER	0.5	0	0
11.) $C_3 + 3(s) \leftrightarrow 3(s) + 3C(b)$	ER	0.023	0	0
12.) $N_2 + (s) \leftrightarrow N + N(s)$	ER	1	0	636.85

The implementation into US3D was first described by Candler [23]. The original implementation had to be modified in this work due to errors found through initial testing. Verification of the implementation in US3D is supplied in Chapter IV. The approach involves solving for the surface coverage (number of adsorbed N and O atoms on the available surface sites), and then computing the rate of formation of gas-phase species through competing kinetics-based processes [23]. The reactions and rate coefficients that comprise the ZA model are taken from Reference [64] and are shown in Table 8.

The first two reactions represent the adsorption and desorption of atomic oxygen

and nitrogen. Reactions 3-8 and 12 represent the recombination of adsorbed atoms, recombination of gas-phase species with adsorbed atoms, and oxidation of bulk carbon. Reactions 9-11 represent the sublimation of bulk carbon or the condensation of atomic and molecular carbon gas. A major difference from the Park model is that surface reactions are allowed to take place in both directions with the preferred direction dependent on the kinetic rates and equilibrium constants of each reaction. The original ZA model lacks a carbon nitridation reaction, but a method to implement it is discussed in Section 3.4. The importance of nitridation will be discussed in the next few chapters.

Corresponding net reaction fluxes are as follows:

$$
\begin{aligned}
r_1 &= k_{f1}\frac{\rho_O}{M_O}\Phi_e - k_{b1}\Phi_O \\[4pt]
r_2 &= k_{f2}\frac{\rho_N}{M_N}\Phi_e - k_{b2}\Phi_N \\[4pt]
r_3 &= k_{f3}\left(\Phi_O\right)^2 - k_{b3}\frac{\rho_{O_2}}{M_{O_2}}\left(\Phi_e\right)^2 \\[4pt]
r_4 &= k_{f4}\frac{\rho_{O_2}}{M_{O_2}}\Phi_e - k_{b4}\frac{\rho_O}{M_O}\Phi_O \\[4pt]
r_5 &= k_{f5}\frac{\rho_{CO_2}}{M_{CO_2}}\Phi_e - k_{b5}\frac{\rho_{CO}}{M_{CO}}\Phi_O \\[4pt]
r_6 &= k_{f6}\Phi_O - k_{b6}\frac{\rho_{CO}}{M_{CO}}\Phi_e \quad\quad\quad (76) \\[4pt]
r_7 &= k_{f7}\frac{\rho_O}{M_O}\Phi_O - k_{b7}\frac{\rho_{CO_2}}{M_{CO_2}}\Phi_e \\[4pt]
r_8 &= k_{f8}\left(\Phi_O\right)^2 - k_{b8}\frac{\rho_{CO_2}}{M_{CO_2}}\left(\Phi_e\right)^2 \\[4pt]
r_9 &= k_{f9}\frac{\rho_C}{M_C}\Phi_e - k_{b9}\Phi_e \\[4pt]
r_{10} &= k_{f10}\frac{\rho_{C_2}}{M_{C_2}}\left(\Phi_e\right)^2 - k_{b10}\left(\Phi_e\right)^2 \\[4pt]
r_{11} &= k_{f11}\frac{\rho_{C_3}}{M_{C_3}}\left(\Phi_e\right)^3 - k_{b11}\left(\Phi_e\right)^3 \\[4pt]
r_{12} &= k_{f12}\frac{\rho_{N_2}}{M_{N_2}}\Phi_e - k_{b12}\frac{\rho_N}{M_N}\Phi_N
\end{aligned}
$$

where Φ_e, Φ_O, and Φ_N are the concentrations of empty surface sites, sites with ad-

Table 9. Adsorption/desorption equilibrium rate constants for the Zhluktov and Abe model.

Reaction	A_{eq}	β	E_{des} (kJ mol^{-1})
1b.) $O + (s) \leftrightarrow O(s)$	1.72×10^7	0	374.13
2b.) $N + (s) \leftrightarrow N(s)$	1.72×10^7	0	304.29

sorbed atomic oxygen, and sites with adsorbed atomic nitrogen, respectively. The calculation of the equilibrium constants begins by using known equilibrium expressions for reactions one and two. The equilibrium constant for reaction one is a function of the concentration of oxygen atoms X_O in the gas phase on the reactants side and the amount of adsorbed O atoms on the products side:

$$K_1 = \frac{k_{f1}}{k_{b1}} = \frac{\Phi_O}{X_O \Phi_e} \tag{77}$$

where X_k represents the concentration of species k. Solving for Φ_e / Φ_O gives:

$$\frac{\Phi_e}{\Phi_O} = \frac{1}{K_1 X_O} \quad \text{or} \quad \frac{\Phi_O}{\Phi_e} = K_1 X_O \tag{78}$$

The Φ_O / Φ_e fraction is common to many of the equilibrium constant expressions for the reactions listed in Table 8. Similarly for reaction two:

$$K_2 = \frac{k_{f2}}{k_{b2}} = \frac{\Phi_N}{X_N \Phi_e} \tag{79}$$

$$\Rightarrow \frac{\Phi_e}{\Phi_N} = \frac{1}{K_2 X_N} \quad \text{or} \quad \frac{\Phi_N}{\Phi_e} = K_2 X_N$$

The equilibrium constants for both adsorption/desorption reactions (K_1 and K_2) are found using Equation 55 with their respective rate constants and activation energies found in Table 9. Mobile adsorption was assumed with the surface site concentration set to $B = 3.5 \times 10^{19}$ m^{-2}, which gives $\Phi = 5.8 \times 10^{-8}$ kmol m^{-2} [136].

Next, the equilibrium constant for reaction three can be written as:

$$K_3 = \frac{X_{O_2}\Phi_e^2}{\Phi_O^2} = \frac{X_{O_2}}{X_O^2}\frac{1}{K_1^2} \tag{80}$$

The ratio X_{O_2}/X_O^2 is the equilibrium constant for the *gas phase* reaction:

$$O + O \to O_2 \tag{81}$$

The equilibrium constant can be computed using thermodynamic data from the CEA database and the Gibbs free energy equation. Hence, K_3 is easily computed from known quantities. Following this same procedure, the rest of the equilibrium constants are calculated as follows:

$$
\begin{aligned}
K_4 &= \frac{X_O\Phi_O}{X_{O_2}\Phi_e} = \frac{X_O^2}{X_{O_2}}K_1 \\
K_5 &= \frac{X_{CO}\Phi_O}{X_{CO_2}\Phi_e} = \frac{X_{CO}X_O}{X_{CO_2}}K_1 \\
K_6 &= \frac{X_{CO}\Phi_e}{X_{C(b)}\Phi_O} = \frac{X_{CO}}{X_O X_{C(b)}}\frac{1}{K_1} \\
K_7 &= \frac{X_{CO_2}\Phi_e}{X_O X_{C(b)}\Phi_O} = \frac{X_{CO_2}}{X_O^2 X_{C(b)}}\frac{1}{K_1} \\
K_8 &= \frac{X_{CO_2}\Phi_e^2}{X_{C(b)}\Phi_O^2} = \frac{X_{CO_2}}{X_O^2 X_{C(b)}}\frac{1}{K_1^2} \\
K_9 &= \frac{X_{C(b)}\Phi_e}{X_C\Phi_e} = \frac{X_{C(b)}}{X_C} \\
K_{10} &= \frac{X_{C(b)}^2\Phi_e^2}{X_{C_2}\Phi_e^2} = \frac{X_{C(b)}^2}{X_{C_2}} \\
K_{11} &= \frac{X_{C(b)}^3\Phi_e^3}{X_{C_3}\Phi_e^3} = \frac{X_{C(b)}^3}{X_{C_3}} \\
K_{12} &= \frac{X_N\Phi_N}{X_{N_2}\Phi_e} = \frac{X_N^2}{X_{N_2}}K_2
\end{aligned} \tag{82}
$$

The backward rate coefficients are simply found by evaluating $k_{bi} = k_{fi}/K_i$. It is

64

important to stress that the surface equilibrium constants are dependent on gas-phase equilibrium constants, and thus, there is a coupling between the gas-phase kinetic model and the surface boundary condition [23]. There are five reactions in the above equilibrium relations that involve gas phase species and carbon bulk material (e.g. $X_{C(b)}/X_C$; $C \rightarrow C(b)$). Fortunately, the CEA database includes thermodynamic properties for certain bulk materials such as carbon, and the equilibrium constants can be computed.

The rates of species production on the surface are:

$$
\begin{aligned}
\dot{m}_O &= (-r_1 + r_4 - r_7)\, M_O \\
\dot{m}_{CO} &= (r_5 + r_6)\, M_{CO} \\
\dot{m}_{CO_2} &= (-r_5 + r_7 + r_8)\, M_{CO_2} \\
\dot{m}_C &= -r_9 M_C \\
\dot{m}_{C_2} &= -r_{10} M_{C_2} \\
\dot{m}_{C_3} &= -r_{11} M_{C_3} \\
\dot{m}_N &= (-r_2 + r_{12})\, M_N \\
\dot{m}_{O_2} &= (r_3 - r_4)\, M_{O_2} \\
\dot{m}_{N_2} &= -r_{12} M_{N_2}
\end{aligned}
\tag{83}
$$

The surface production rate for any species included in the gas phase chemistry, including charged particles, that does not contribute to any surface reaction is set to zero. The mass fluxes for the amount of O and N absorbed on the surface are:

$$
\begin{aligned}
\dot{m}_{O(s)}/M_O &= r_1 - 2r_3 + r_4 + r_5 - r_6 - r_7 - 2r_8 = 0 \\
\dot{m}_{N(s)}/M_N &= r_2 + r_{12} = 0
\end{aligned}
\tag{84}
$$

Using these expressions, the total surface mass blowing rate is:

$$\dot{m} = \sum \dot{m}_i = M_C \left(r_6 + r_7 + r_8 - r_9 - 2r_{10} - 3r_{11} \right) \tag{85}$$

The solution of Equations 84 together with the sum of surface coverage concentrations:

$$\Phi_O + \Phi_N + \Phi_e = \Phi \tag{86}$$

yields Φ_O, Φ_N, and Φ_e values.

Newton's method for non-linear systems in two-dimensions is used for determining the surface coverage concentrations, which is written in vector notation as:

$$\vec{P}_{n+1} = \vec{P}_n - \vec{J}^{-1}\left(\vec{P}_n\right) \vec{F}\left(\vec{P}_n\right) \tag{87}$$

where $\vec{J}$ represents the Jacobian. The vectors $\vec{P}$ and $\vec{F}$ are given by:

$$\vec{P} = \begin{bmatrix} \Phi_O \\ \Phi_N \end{bmatrix}, \quad \vec{F} = \begin{bmatrix} f_1\left(\Phi_O\right) \\ f_2\left(\Phi_N\right) \end{bmatrix} = \begin{bmatrix} r_1 - 2r_3 + r_4 + r_5 - r_6 - r_7 - 2r_8 \\ r_2 + r_{12} \end{bmatrix} \tag{88}$$

The Jacobian and its inverse are written as:

$$\vec{J} = \begin{bmatrix} \dfrac{\partial f_1}{\partial \Phi_O} & \dfrac{\partial f_1}{\partial \Phi_N} \\ \dfrac{\partial f_2}{\partial \Phi_O} & \dfrac{\partial f_2}{\partial \Phi_N} \end{bmatrix}, \quad \vec{J}^{-1} = \dfrac{1}{\dfrac{\partial f_1}{\partial \Phi_O}\dfrac{\partial f_2}{\partial \Phi_N} - \dfrac{\partial f_1}{\partial \Phi_N}\dfrac{\partial f_2}{\partial \Phi_O}} \begin{bmatrix} \dfrac{\partial f_2}{\partial \Phi_N} & -\dfrac{\partial f_1}{\partial \Phi_N} \\ -\dfrac{\partial f_2}{\partial \Phi_O} & \dfrac{\partial f_1}{\partial \Phi_O} \end{bmatrix} \tag{89}$$

Last, the partial derivatives of f_1 and f_2 need to be calculated using the chain rule by invoking the constraint:

$$\Phi_e = \Phi - \Phi_O - \Phi_N, \quad \frac{\partial \Phi_e}{\partial \Phi_O} = -1, \quad \frac{\partial \Phi_e}{\partial \Phi_N} = -1 \tag{90}$$

The solution procedure is iterated until we have converged solutions for Φ_O and Φ_N.

By substituting Φ_O, Φ_N, and Φ_e into Equations 76, the necessary mass production rates can be obtained from Equations 83. Next, the surface mass balance equation is solved where v_w is obtained from Equation 85 since $\dot{m} = \rho_w v_w$. Equation 49 is non-linear that is solved iteratively for each species until the surface normal velocity converges. The approach assumes that Fick's law for diffusion holds.

As an example, the surface mass balance equation can be solved for the N_2 surface mass fraction. The discretized form of Equation 49 is given as:

$$-\rho_w D \frac{(y_{N_2,1} - y_{N_2,w})}{\Delta n} + \rho_w v_w y_{N_2,w} = M_{N_2} w_{N_2} = \dot{m}_{N_2} \tag{91}$$

where $y_{N_2,1}$ is the mass fraction of N_2 in the first cell away from the wall and Δn is the distance from the first cell center to the wall. Substituting for $\dot{m}_{N_2}$ from Equations 83 and 76 and rearranging terms, results in:

$$
\begin{aligned}
\left(\frac{D}{\Delta n} + v_w\right) y_{N_2,w} &= \frac{D}{\Delta n} y_{N_2,1} + \frac{1}{\rho_w}\left(-r_{12} M_{N_2}\right) \\
\left(\frac{D}{\Delta n} + v_w\right) y_{N_2,w} &= \frac{D}{\Delta n} y_{N_2,1} + k_{b12}\frac{M_{N_2}}{M_N}\frac{\rho_N}{\rho_w}\Phi_N - k_{f12}\frac{\rho_{N_2}}{\rho_N}\Phi_e
\end{aligned}
\tag{92}
$$

where $\rho_N/\rho_w = y_{N,w}$ and $\rho_{N_2}/\rho_w = y_{N_2,w}$. Solving for $y_{N_2,w}$ gives:

$$y_{N_2,w} = \frac{\dfrac{D}{\Delta n} y_{N_2,1} + k_{b12}\dfrac{M_{N_2}}{M_N} y_{N,w}\Phi_N}{\dfrac{D}{\Delta n} + v_w + k_{f12}\Phi_e} \tag{93}$$

Equation 93 is an approximate solution for $y_{N_2,w}$ because we are assuming $y_{N,w}$ is known when it actually has its own mass balance equation to solve. However, the entire solution procedure is iterated until the wall normal velocity converges. All mass fractions at the wall should balance when the convergence criterion for v_w is met and

then the proper gradients for the wall boundary condition can be set.

3.3.8 Comparison of Park and ZA Models.

Many authors have applied and compared the Park and ZA models to different re-entry trajectories and arcjet tunnel data. Havstad and Ferencz [44] found the models predicted similar ablative mass fluxes under sublimation conditions. The primary species resulting from carbon sublimation is C_3, and both models include a C_3 reaction with similar forward rates. Chen and Milos [27] showed that the ZA model predicted substantially lower stagnation point ablation rates compared to the Park model but larger convective heat fluxes. Another interesting discovery by Chen and Milos was the effect of the nitridation reaction included in the Park model, which the ZA model lacks. The removal of the nitridation reaction from the Park model significantly lowered the ablation rate to values near the ZA prediction but had a relatively minor impact on other parameters such as the wall heating rate.

Suzuki et al. [115, 116] calculated the nitridation rate of graphite test models to be 100 times smaller than the value obtained by Park and Bogdanoff [94] in plasma wind tunnel tests at surface temperatures ranging from 1351-1723 K. However even with a much lower nitridation efficiency, they predicted the surface recession of the HAYABUSA capsule to be 25% larger than that calculated without nitridation. Beerman et al. [12] used the Park model with and without nitridation to analyze a carbon ablative material at a Stardust peak heating condition. They found that nitridation had a very minimal impact on the stagnation point ablation and convective heating rates, which is in stark contrast to the results of Chen and Milos [27] and Suzuki et al. [115, 116] The rationale was that nitridation was an insignificant surface reaction, or did not occur, and it could be replaced by a surface nitrogen catalytic process. This idea was carried over into the work of Chen and Gokcen [24] who compared the two

models against arcjet data but replaced Park's nitridation reaction with a nitrogen surface recombination reaction. Note that the arcjet tests had stagnation pressures ranging from approximately 0.023-0.83 atm and surface temperatures ranging from approximately 1600-3000 K. It will be shown in this research that the level of nitridation is dependent on the wall pressure and temperature. The ablation rates predicted by the modified Park model matched arcjet data extremely well for a majority of the tests while the ZA model consistently under predicted the ablation rates. The inclusion of a nitridation reaction into the ZA model could possibly improve these predictions.

Recognize that both ablation models specify forward rates using relatively linear Arrhenius expressions. As previously discussed and shown in Figure 12, measured oxidation rates displayed non-linear Arrhenius behavior. The ZA model attempts to account for this non-linearity by specifying "linear" expressions for many separate, competing kinetic steps. The surface reactions specified in the legacy models, including the Park model, only describe one-step kinetic processes and cannot adequately capture this non-linear behavior.

3.4 Carbon Nitridation Reaction

Carbon nitridation is recognized as an important surface reaction to characterize in order to properly compute convective and radiative heat fluxes [108, 38]. Currently, the ZA model can only be considered an oxidation and sublimation surface reaction model because it does not include a carbon nitridation mechanism. The addition of a carbon nitridation reaction will make it a more comprehensive and physically authentic model. The development of the nitridation reaction rates for inclusion in the ZA model shown in this section represents new and original work.

Zhang et al. [135] presented a review experimental carbon nitridation reaction

69

efficiencies determined from measured carbon mass loss rates. Additionally, Lutz et al. [60] is attempting to measure nitridation and oxidation efficiencies using laser-induced fluorescence. The nitridation reaction defined in these works is:

$$N + C(b) \rightarrow CN \tag{94}$$

There have been attempts to implement this reaction into computational ablation models, however it was usually defined as an irreversible process [95, 25, 6]. Following the surface chemistry model developed in the previous section, the carbon nitridation reaction can be represented using an ER recombination process or an Arrhenius-type expression. All defined surface reactions are assumed to proceed through a single active site type (i.e. bulk carbon). The first path is simply defined as direct nitridation:

$$N + (s) + C(b) \leftrightarrow CN + (s) \tag{95}$$
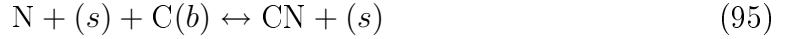
The second path is defined as a surface participating reaction:

$$N(s) + C(b) \leftrightarrow CN + (s) \tag{96}$$

These formulations allow for the surface reactions to occur in forward and backward directions with the preferred direction dependent on the kinetic rates and equilibrium constants of each reaction.

The net reaction flux for each pathway can be expressed in terms of forward and backward reaction rate coefficients (k_f and k_b), stoichiometric coefficients (ν), and the generalized concentrations of gas, surface, and bulk species (X_s) as shown in Equation 47. For a gas phase species $X_s \equiv C_s = \rho_s/M_s$ in kmol m^{-3}, for a surface species $X_s \equiv \Phi_s$ in kmol m^{-2}, and for a pure bulk species $X_s \equiv 1$ (dimensionless). The net reaction flux is different between the reaction paths. For direct nitridation,

the reaction flux is:

$$r = k_f C_N \Phi_e - k_b C_{CN} \Phi_e \tag{97}$$

The units of the reaction flux are kmol m^{-2} s^{-1}, which gives the forward reaction rate in units of m^3 $kmol^{-1}$ s^{-1} for consistency. The net flux for the surface participating reaction is given by:

$$r = k_f \Phi_N - k_b C_{CN} \Phi_e \tag{98}$$

For consistency, the units of the forward reaction rate are s^{-1}.

The direct nitridation equilibrium constant can be written as:

$$K = \frac{X_{CN} \Phi_e}{X_N X_{C(b)} \Phi_e} = \frac{X_{CN}}{X_N X_{C(b)}} \tag{99}$$

which can be computed using the CEA database [70] and the minimization of Gibbs free energy (Equation 31). As before, CEA computes the activity-based equilibrium constant which needs to be converted to the concentration-based equilibrium constant. The surface participating equilibrium constant is given by:

$$K = \frac{X_{CN} \Phi_e}{\Phi_N X_{C(b)}} \tag{100}$$

which is a function of the nitrogen adsorption reaction. Substituting in Equation 79 for Φ_e / Φ_N, the equilibrium constant can now be specified as:

$$K = \frac{X_{CN}}{X_N X_{C(b)}} \frac{1}{K_2} \tag{101}$$

The solution process is the same as described previously, but only the flux for the surface participating nitridation reaction will affect the surface coverage equation for Φ_N. Because the ZA model does not include any other CN production mechanism,

71

the CN mass production rate is simply:

$$\dot{m}_{CN} = r M_{CN} \tag{102}$$

The total surface mass blowing rate will now also include contribution from this reaction flux computed by either nitridation mechanism. Therefore, to close the system of equations, the forward reaction rates must be defined for each path.

3.4.1 Determination of Forward Rates.

Even though the purpose of Zhang et al. [135] was to publish carbon nitridation reaction efficiencies, the most fundamental information contained in the article is the carbon mass loss rate at different surface temperatures, pressures, and nitrogen concentrations. The experiments were performed in N-N_2 mixtures with carbon mass loss rates measured over a pure graphite rod. The reaction efficiencies simply parametrize the observed mass loss within a very simple model that only considers the reaction $N + C(b) \rightarrow CN$, with no competing surface processes like adsorption or catalysis nor the limitation of a finite number of active sites. The tabulated carbon mass loss rates, which are averaged over time and surface location, can be matched to an analytical expression developed for a simple N-N_2 system. The experimental carbon mass loss rate due to nitridation can be computed from values in Tables 2 and 4 from Zhang et al. [135]:

$$\dot{m}_C = \frac{\triangle m_{C,tot} - \triangle m_{C,con}}{\triangle t \pi d_s L_s} \tag{103}$$

where $\triangle m_{C,tot}$ is the total carbon mass loss, $\triangle m_{C,con}$ is the control mass loss, $\triangle t$ is the test time, d_s is the diameter of the graphite rod, and L_s is the rod length. The diameter of all the rods was 3.175 mm. The corresponding test conditions are contained in Tables 1 and 3 from Zhang et al. [135]

The experimental carbon mass loss rate should match Equation 102, but with M_C instead of M_{CN}, and with the reaction flux specified by either Equation 97 or 98, depending on the path. The fraction of available surface sites covered by atomic nitrogen must be considered, which may be different under different environmental conditions, because it will influence the nitridation rate for both paths. The goal is to obtain a set of experimentally-based k_f values as a function of surface temperatures that reproduce the set of carbon mass loss measurements. Then a fit can be computed based on an ER or Arrhenius form, which can be implemented into the ZA model.

Consider a simple N-N_2 system that accounts for adsorption and ER recombination at the surface:

$$N + (s) \leftrightarrow N(s) \tag{104}$$

$$N_2 + (s) \leftrightarrow N + N(s) \tag{105}$$

with parameters taken from Table 8. The concentration of empty and occupied sites are related to the total site concentration as:

$$\Phi = \Phi_e + \Phi_N \tag{106}$$

where $\Phi = 5.8 \times 10^{-8}$ kmol m^{-2} [136]. The next subsections develop the analytical expressions for the forward reaction rates based on either nitridation path.

3.4.2   Direct Nitridation.

The first step in finding an expression for k_f is to determine the concentration of empty sites from the concentration of sites occupied by atomic nitrogen. The rate of change of the adsorbed atomic nitrogen under steady-state conditions is:

$$\frac{d\Phi_N}{dt} = 0 = r_1 + r_2 \tag{107}$$

where the subscripts 1 and 2 refer to the adsorption and ER reactions, respectively, shown in Equations 104 and 105. Substituting for the reaction fluxes and empty surface site concentrations gives:

$$k_{f1}C_N \left(\Phi - \Phi_N\right) - k_{b1}\Phi_N + k_{f2}C_{N_2} \left(\Phi - \Phi_N\right) - k_{b2}C_N\Phi_N = 0 \tag{108}$$

Solving for Φ_N gives:

$$\Phi_N = \frac{\left(k_{f1}C_N + k_{f2}C_{N_2}\right)\Phi}{k_{f1}C_N + k_{b1} + k_{f2}C_{N_2} + k_{b2}C_N} \tag{109}$$

All forward and backward reaction rates are taken from the ZA model, and the concentrations of N and N_2 are measured in the experiment. The concentration of empty sites can then be calculated by $\Phi_e = \Phi - \Phi_N$. The experimental carbon mass loss rate should match the analytic rate:

$$\dot{m}_C = r_3 M_C = \left(k_{f3}C_N\Phi_e - k_{b3}C_{CN}\Phi_e\right)M_C \tag{110}$$

where the subscript 3 refers to the direct nitridation reaction. The reaction flux for direct nitridation is given in Equation 97. Solving for k_{f3}:

$$k_{f3} = \frac{\dot{m}_C}{\Phi_e C_N M_C} + \frac{k_{b3}C_{CN}}{C_N} \tag{111}$$

74

The equilibrium constant for the nitridation reaction could also be substituted giving k_{f3} as:

$$k_{f3} = \frac{\dot{m}_C}{\Phi_e M_C \left(C_N - \dfrac{C_{CN}}{K_3} \right)} \tag{112}$$

The concentration of CN at the surface was not measured in the experiment, so it is an unknown. However, an assumption may be made that C_{CN} is negligible compared to C_N and C_{N_2} $(C_{CN} \ll C_N, C_{N_2})$, which gives k_{f3} as:

$$k_{f3} = \frac{\dot{m}_C}{\Phi_e C_N M_C} \tag{113}$$

In fact, this assumption is consistent with the experiments because the mole fractions were computed based on assuming that N and N_2 were the only gas species in the flow. Equation 113 provides a simple relation to calculate forward reaction rates based on experimental carbon mass loss rates at different surface temperatures.

The ER forward rate can be used to define the direct nitridation reaction as shown in Table 7. The required inputs for the ER rate are γ_{er}, β, and E_{er}. For a pure kinetic formulation, β equals zero and γ_{er} is within the range of zero to one [67]. The reaction efficiency is dimensionless, so the bracketed term provides the units for k_f, which is consistent with the net reaction flux shown in Equation 97.

The ER coefficients can be determined by a linear least squares fit on the log of the forward reaction rate. The resulting linear equation is:

$$\ln\left(|k_f|\right) = \ln\left(\left|\frac{\bar{\nu}_s}{4\Phi}\right|\right) + \ln\left(|\gamma_{er}|\right) + \frac{(-E_{er})}{RT} \tag{114}$$

Equation 114 can be represented by the matrix equation $Ax = b$ with a known linear

least squares solution of $x = \left(A^T A\right)^{-1} A^T b$ [4]. The system in matrix form is:

$$
\begin{bmatrix} 1 & \dfrac{1}{RT} \\ \vdots & \vdots \\ \vdots & \vdots \\ 1 & 0 \end{bmatrix} \begin{bmatrix} \ln\left(|\gamma_{er}|\right) \\ \left(-E_{er}\right) \end{bmatrix} = \begin{bmatrix} \ln\left(|k_f|\right) - \ln\left(\left|\dfrac{\bar{\nu}_s}{4\Phi}\right|\right) \\ \vdots \\ \vdots \\ 0 \end{bmatrix}
\tag{115}
$$

where the constraint $0 < \gamma_{er} \leq 1$ is also folded into the system of equations. The method described here will provide an ER forward reaction rate that can be implemented into the ZA model.

3.4.3 Surface Participating Reaction.

For the surface participating reaction, the situation is more complicated because the surface coverage is coupled to the nitridation rate. Now the rate of change of the adsorbed atomic nitrogen under steady-state conditions is:

$$
\frac{\mathrm{d}\Phi_N}{\mathrm{d}t} = 0 = r_1 + r_2 - r_3
\tag{116}
$$

where r_1 and r_2 represent the same reactions as defined for direction nitridation and r_3 is defined by Equation 98. Substituting for the reaction fluxes and empty surface site concentrations results in:

$$
k_{f1}C_N\left(\Phi - \Phi_N\right) - k_{b1}\Phi_N + k_{f2}C_{N_2}\left(\Phi - \Phi_N\right) - k_{b2}C_N\Phi_N - k_{f3}\Phi_N + k_{b3}C_{CN}\left(\Phi - \Phi_N\right) = 0
\tag{117}
$$

Solving for Φ_N gives:

$$
\Phi_N = \frac{\left(k_{f1}C_N + k_{f2}C_{N_2} + k_{b3}C_{CN}\right)\Phi}{k_{f1}C_N + k_{b1} + k_{f2}C_{N_2} + k_{b2}C_N + k_{f3} + k_{b3}C_{CN}}
\tag{118}
$$

The analytic solution for Φ_N now contains forward and backward rates for the surface participating nitridation reaction. Solving for the experimental carbon mass loss rate shows:

$$\dot{m}_C = r_3 M_C = (k_{f3}\Phi_N - k_{b3}C_{CN}\Phi_e) M_C \tag{119}$$

Substituting for Φ_N and using the known equilibrium constant instead of k_{b3} gives:

$$\dot{m}_C = k_{f3}M_C\Phi \left\{ \frac{k_{f1}C_N + k_{f2}C_{N_2} + k_{b3}C_{CN}}{k_{f1}C_N + k_{b1} + k_{f2}C_{N_2} + k_{b2}C_N + k_{f3} + k_{b3}C_{CN}} - \frac{C_{CN}}{K_3}\left[1 - \frac{k_{f1}C_N + k_{f2}C_{N_2} + k_{b3}C_{CN}}{k_{f1}C_N + k_{b1} + k_{f2}C_{N_2} + k_{b2}C_N + k_{f3} + k_{b3}C_{CN}}\right]\right\} \tag{120}$$

Assuming again that $C_{CN} \ll C_N, C_{N_2}$, the carbon mass loss rate can be simplified to:

$$\dot{m}_C = k_{f3}M_C\Phi \left[\frac{k_{f1}C_N + k_{f2}C_{N_2}}{k_{f1}C_N + k_{b1} + k_{f2}C_{N_2} + k_{b2}C_N + k_{f3}} \right] \tag{121}$$

Solving the above equation for k_{f3} gives:

$$k_{f3} = \frac{\dfrac{\dot{m}_C}{M_C\Phi}\left(k_{f1}C_N + k_{b1} + k_{f2}C_{N_2} + k_{b2}C_N\right)}{k_{f1}C_N + k_{f2}C_{N_2} - \dfrac{\dot{m}_C}{M_C\Phi}} \tag{122}$$

Again, all parameters above are known from either the ZA model or experiment. Accordingly, the forward reaction rate values can be tabulated as a function of surface temperature.

An Arrhenius expression will be used for the forward rate of the surface participating reaction because the units are in s^{-1}. The coefficients A, β, and E_a can be found using a linear least squares fit as was done previously. For consistency with the ZA oxidation reactions that are specified in an Arrhenius form, β is set equal to one.
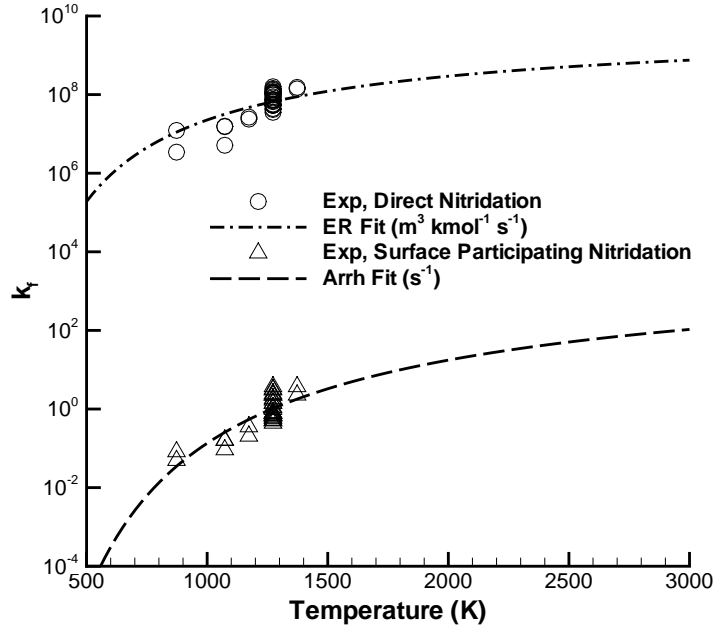
Figure 18. Forward rate fits for both considered carbon nitridation reactions.

The linear equation is:

$$\ln\left(|k_f|\right) = \ln\left(|A|\right) + \ln\left(\left|T'\right|\right) + \frac{(-E_a)}{RT} \qquad (123)$$

The linear least squares solution can be found, and the surface participating nitridation reaction can also be added to the ZA model.

3.4.4 Forward Rate Fits.

The results of the linear least squares solution for both nitridation paths are shown in Table 10. As expected, there is excellent agreement between the proposed forward reaction rates and experimental data as shown in Figure 18. Additional experimental data is desired to further validate the forward rate expressions, especially at higher surface temperatures. However, there is no known experimental data that attempts

Table 10. Forward rate fits for nitridation reactions.

Reaction	Type	γ_{er} or A	β	E (kJ mol^{-1})
$N + (s) + C(b) \leftrightarrow CN + (s)$	ER	0.36	0	36.86
$N(s) + C(b) \leftrightarrow CN + (s)$	Arrh	0.57	1	69.46

to characterize the nitrogen-carbon surface interaction, much less consider the steps of the surface reaction process.

The direct nitridation reaction has a lower activation energy compared to the surface participating reaction, which will likely give the occurrence of this reaction a higher probability. Furthermore, direct nitridation is a one-step reaction that is only dependent on the availability of open surface sites. In comparison, the surface participating reaction follows a general surface reaction process similar to the oxidation mechanisms found in the ZA model, where atomic nitrogen needs to be in an adsorbed state before it will react with the bulk carbon. Ma et al. [61] demonstrated adsorption and diffusion of N-atoms on single layers of graphene using density-functional theory. Therefore, the reaction that represents the physical process may be the Arrhenius-type mechanism, but this needs to be experimentally verified. It is expected that if both reaction types predicted CN production at the surface, the direct nitridation mechanism would produce larger quantities of CN.

3.5 Radiative Transitions of Cyanogen (CN)

Atoms and molecules emit radiation in high temperature hypersonic flows that can be measured to determine radiative heating contributions. Radiative transitions occur when energy is released resulting from the internal energy state of an atom or molecule going from an upper to a lower level. The transitions from the first two excited electronic states to the ground state of CN are known as the CN red ($A^2\Pi \rightarrow X^2\Sigma^+$) and CN violet ($B^2\Sigma^+ \rightarrow X^2\Sigma^+$) bands. The notation used to indicate

Table 11. Radiative transition wavelengths for the CN violet band. The v' and v" columns represent different vibrational quantum states [52].

v'	v"	λ (nm)	v'	v"	λ (nm)	v'	v"	λ (nm)	v'	v"	λ (nm)
0	0	387.629	3	4	416.067	6	4	334.724	8	8	385.813
0	1	420.956	3	5	452.537	6	5	357.930	8	9	415.141
0	2	459.995	4	0	293.755	6	6	384.203	8	10	448.759
1	0	358.145	4	2	333.518	6	7	414.184	9	4	283.778
1	1	386.410	4	3	357.224	6	8	448.705	9	5	300.284
1	2	419.057	4	4	384.168	7	3	296.885	9	6	318.560
1	3	457.177	4	5	415.053	7	4	315.262	9	8	361.667
2	0	333.274	4	6	450.800	7	5	335.765	9	9	387.317
2	1	357.617	5	3	333.985	7	6	358.780	9	10	416.422
2	2	385.404	5	4	357.423	7	7	384.791	10	5	285.947
2	3	417.414	5	5	384.009	7	8	414.411	10	6	302.472
2	4	454.677	5	6	414.412	7	9	448.439	10	7	320.750
3	1	333.291	5	7	449.508	8	4	298.433	10	9	363.791
3	2	357.299	6	2	295.608	8	5	316.743	10	10	389.351
3	3	384.645	6	3	314.082	8	7	360.012			

the type of transition (i.e. $B^2\Sigma^+ \rightarrow X^2\Sigma^+$) comes from the description of molecular structure using quantum physics. The different electronic states are represented by X, A, B, etc, with X designating the ground electronic state. The first three total angular momentum quantum (energy) states are designated as Σ, Π, or Δ. The pre-superscript and superscript to the total angular momentum quantum state identifies the total spin multiplicity of all the electrons in the outermost orbit and the symmetry of the electronic wave functions, respectively. The radiative transition wavelengths for the CN violet bands are given in Table 11 [52].

3.6 Radiation Solver

The radiation solver used is the Nonequilibrium Air Radiation (NEQAIR) code version 13.2 [125]. NEQAIR is a spectral high-resolution line-by-line code that computes the radiative emission and adsorption of atomic species and molecular electronic

and infrared band systems along a line-of-sight. The solver requires temperatures and species number densities along that line-of-sight to calculate quantities such as spectral radiance or radiative heating. The code can model bound-free and free-free continuum radiation. NEQAIR has been used extensively to compare against experimental measurements from a number of different facilities and simulated atmospheres [21, 87, 68, 39]. As noted previously, the radiation solver is run uncoupled from the CFD solver.

The populations of the excited electronic states can be found by using either Boltzmann or non-Boltzmann distributions. The Boltzmann distribution is appropriate under equilibrium conditions and is evaluated at the specified electronic temperature, which is equal to the vibrational temperature under the assumed two-temperature model. The non-Boltzmann distribution is appropriate for thermal nonequilibrium conditions and follows the quasi-steady-state (QSS) method [92, 125]. The QSS method assumes the rate of change in the population of any electronic energy level is slow compared to the excitation/de-excitation rates into and out of that energy level. Under this condition, the electronic state populations are determined by solving a simple set of linear algebraic equations instead of a set of differential equations.

All NEQAIR results used a non-Boltzmann distribution for the population of excited electronic states. Previous studies [19, 130, 87, 71] have shown that Boltzmann distributions over predict radiation intensities. However, these over predictions were found in highly nonequilibrium regimes, and in particular, for carbon containing environments like Mars and Titan. The CN violet bands were the only atomic or molecular systems considered for the NEQAIR calculations because these were the primary radiative transitions measured in the experiments. The radiative transition wavelengths for the CN violet bands span the spectral range from approximately 283-460 nm [52]. The strongest bands are contained within an approximate spectral range

of 350-390 nm, which were targeted by the spectrometer during experimental testing and used as inputs into NEQAIR. The only other relevant species that radiates near this wavelength range is N_2^+, which has a transition wavelength at 391.1 nm [52]. However, Figure 10 from Chapter II showed there were no substantial spectra measured near this wavelength throughout the shock layer for each surface temperature. Therefore, N_2^+ was not contributing to the measured radiation for these conditions.

Radiance comparisons are made between the spectrometer measurements and the NEQAIR results. The radiance is defined as the radiative flux emitted per unit of observed area and is calculated by integrating the spectral radiance between the wavelength range of 353-391 nm. The radiance is measured in units of $W/(cm^2$-sr). The post-shock flow quantities computed by US3D are extracted from the volumetric solution corresponding to the experimental line-of-sight. The experimental line-of-sight is normal to the stagnation streamline and captures the radiation emitted from the surface out to the shock. Therefore, multiple slice extractions were performed along the stagnation streamline that provided radiance predictions as a function of wall normal distance. The length of the line-of-sight used for the NEQAIR simulations corresponded to the X-2 diameter of 8.5 cm.

The wavelength calibration of the UV spectrometer tended to drift slightly, so the experimental spectra were shifted to match the computed CN transition at approximately 388.4 nm. The slit function of the experimental setup has been characterized as a Voigt profile with Gaussian and Lorentzian line widths of 1.1 nm and 0.3 nm, respectively. To verify this slit function, Figure 19 plots the scaled CN spectral radiance 0.2 mm away from the wall along the stagnation streamline for $T_w = 2410$ K. The plot displays the results from the experiment (X-2) and from using the ZA and Park ablation models. Each data set was scaled by its maximum spectral radiance value. After convolution with the Voigt profile, the numerical spectra calculated by
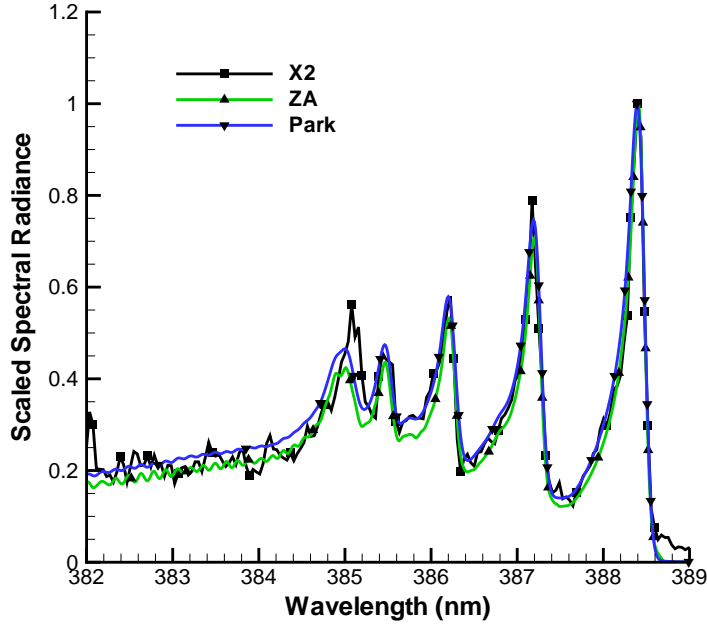
Figure 19. Comparison of the scaled CN spectral radiance 0.2 mm away from the wall along the stagnation streamline for the $T_w = 2410\,\mathrm{K}$ case.

NEQAIR matched the experimental spectra well. The same Gaussian and Lorentzian line widths that comprised the Voigt profile were used for all solutions.

3.6.1 Spatial Resolution Function.

A direct comparison of the radiance measured in the experiment and that predicted by NEQAIR has limited accuracy because there are instrument constraints. The spatial resolution of the collection and spectrometer optics is limited by how sharply the shock layer can be resolved. The resolution of the image focused on the spectrometer camera is determined by the quality of optical alignment. Also, the spectrometer camera is subject to charge smearing, which causes adjacent pixels to share intensity measurements. The net effect of these resolution limitations results in a spatial profile that is broadened in comparison to the actual result.

Following the work of Brandis et al. [20], the broadening may be accounted for

by convolving the predicted radiance computed by NEQAIR with a spatial resolution function (SRF). The SRF is a convolution of the optical and camera resolution functions that is determined by the specific experimental setup. The convolution function used for this work was based on similar experiments at NASA EAST, which matched the same UV spectrometer camera settings. The camera pixel to wall normal distance correlation was mapped to the X-2 setup to calculate appropriate convolutions. Note that this is an estimated SRF calculation, but it should provide a better comparison to the experimental results.

3.7 ZA Rate Coefficients Screening

Computational analyses are sensitive to the physical, chemical, and numerical models used for aeroheating predictions [32]. The input parameters of the models generally use a single nominal value, but there is a range of uncertainty associated with each value [88]. To quantify this uncertainty, Monte Carlo methods are widely used due to their robustness and convergence rate properties. A Monte Carlo uncertainty analysis provides statistical data that determines the fractional contribution of each input parameter to the overall variability of a selected output variable [88]. However to reach statistical convergence, 2000-3000 CFD solutions are required for each input parameter, which makes the method very computationally expensive.

A more recently developed method, called a definitive screening design, has the ability to address the sensitivity of input variables on quantities of interest. Jones and Nachtsheim [47] proposed a three-level definitive screening design that assesses the relative impact of a large number of factors with the ability to identify main (linear) and second-order (non-linear) effects independent of two-factor interactions. The design uses three factor levels with the number of runs equal to $2m + 1$ for m factors with one center point run (baseline). The general structure for m factors is

Table 12. General structure of a definitive screen design with m factors [47]

Run	Factor Levels				
(i)	$x_{i,1}$	$x_{i,2}$	$x_{i,3}$	$\ldots$	$x_{i,m}$
1	0	± 1	± 1	$\ldots$	± 1
2	0	± 1	± 1	$\ldots$	± 1
3	± 1	0	± 1	$\ldots$	± 1
4	± 1	0	± 1	$\ldots$	± 1
5	± 1	± 1	0	$\ldots$	± 1
6	± 1	± 1	0	$\ldots$	± 1
$\vdots$	$\vdots$	$\vdots$	$\vdots$	$\ddots$	$\vdots$
$2m-1$	± 1	± 1	± 1	$\ldots$	0
$2m$	± 1	± 1	± 1	$\ldots$	0
$2m+1$	0	0	0	$\ldots$	0

shown in Table 12. Each run has exactly one factor at its center point and sets all other factors to high or low levels. In addition, two runs were added where no factors were set at their center point.

The 13 pre-exponential reaction rate coefficients of the ZA model (with nitridation) were screened for their relative significance in determining the total CN radiative heat flux. In the absence of precise uncertainty estimates for each coefficient, the screening process was performed by varying the values within a conservative uncertainty range guided by the work of Palmer et al. [88] The adsorption sticking coefficients, S_0, and ER reaction efficiencies, γ_{er}, were varied by $\pm 10\%$, while the Arrhenius reaction rate coefficients were varied by ± 1 order of magnitude. The total CN radiance from each combination of factors was compared to the case with all coefficients set to their nominal values (i.e. baseline case). The quantitative metric was the absolute percent difference from the baseline case. The goal of the screening process is to show which surface reactions have the greatest influence on the overall variability of the CN radiance. Specifically, identification of those reactions that increase

the radiance were of most interest. It should be evident that an efficiency greater than one is not physically meaningful in the context of the surface reaction model framework. However for the purpose of this screening design, it will provide insight into the sensitivity of the efficiency parameters. Before the Park and ZA models are applied to the X-2 experiments, the next chapter will characterize the performance of each model under representative hypersonic re-entry conditions.

IV. Characterization of Ablation Models

In order to better understand the behavior of the different ablation models, a simple set of test cases is used that is representative of a typical re-entry trajectory. The ablation models will be applied to the simulations described by Candler [23]. The results presented below examine the influence of nitridation, the effect of immobile or mobile adsorption, and the sensitivity of the total surface site concentration.

4.1 Simulation Parameters

The test cases involved a 10 cm radius sphere, 8° cone geometry with freestream conditions corresponding to altitudes of 20, 25, 30, and 40 km at a velocity of 7 km sec^{-1}. The surface temperatures and pressures for each altitude are shown in Figure 20. The flow fields were computed on the same grid used in Candler [23], which consisted of 48,000 hexahedral elements (160 axial and 300 wall-normal). The gas is considered to be composed of the following species: N_2, O_2, NO, CO_2, CO, C_2, C_3, CN, C, N, and O. Candler's results compared different gas-phase models coupled with the ZA ablation boundary condition. The results presented here used a gas-phase chemistry model essentially equivalent to that shown in Table 4, but with the elimination of charged species chemistry and the addition of important reactions identified by Martin and Boyd [68]. The three additional Martin and Boyd reactions shown in Arrhenius form (Equation 27) are given in Table 13.

4.2 ZA Model Verification

First, a code verification study was performed because the implementation of the ZA model was relatively complex. The ZA model implemented in US3D was verified against the NASA DPLR code [129, 64]. The verification used the 30 km test
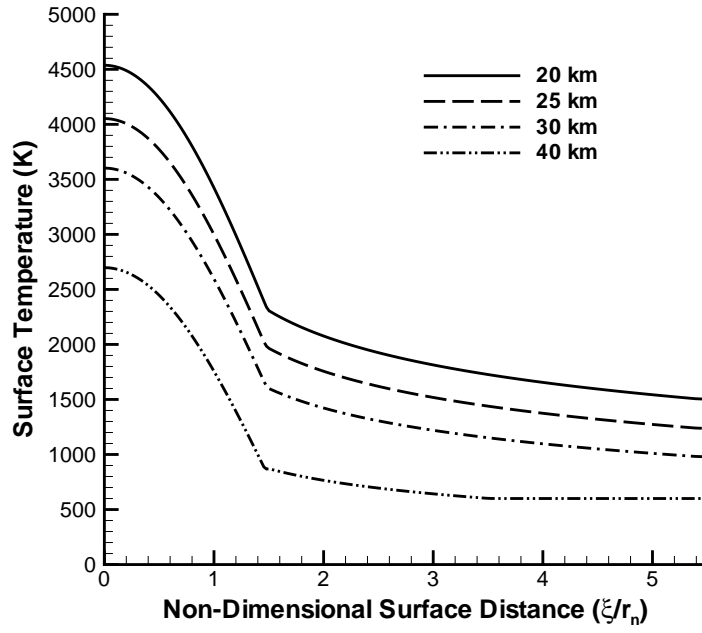
(a) Surface temperature
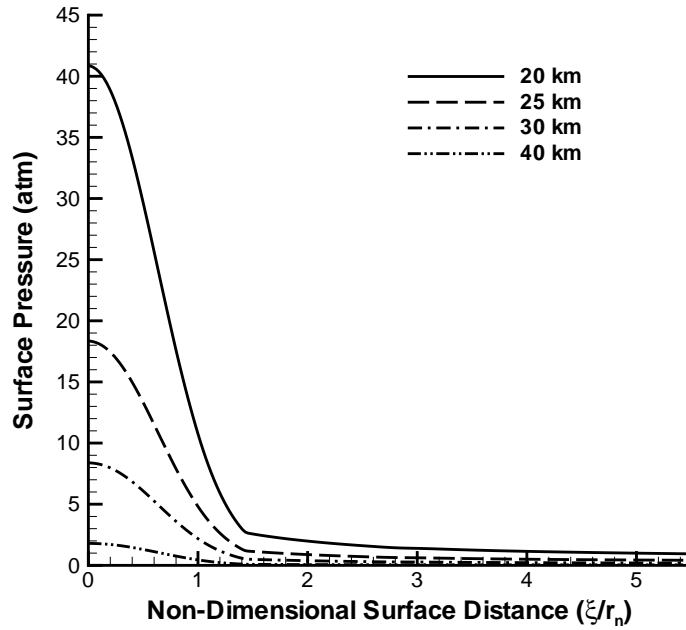
(b) Surface pressure

Figure 20. Surface temperature and pressure distributions for each representative reentry test case.

Table 13. Martin and Boyd reactions and rate coefficients [68].

q	Reaction	A_f	n_f	D_f	T_f
1	$C + NO \leftrightarrow CO + N$	2.3e+10	0.00	0.00	T
2	$C_2 + N_2 \leftrightarrow CN + CN$	1.5e+10	0.00	2.10e+4	T
3	$N + CO_2 \leftrightarrow NO + CO$	3.0e+9	0.00	5.69e+3	T
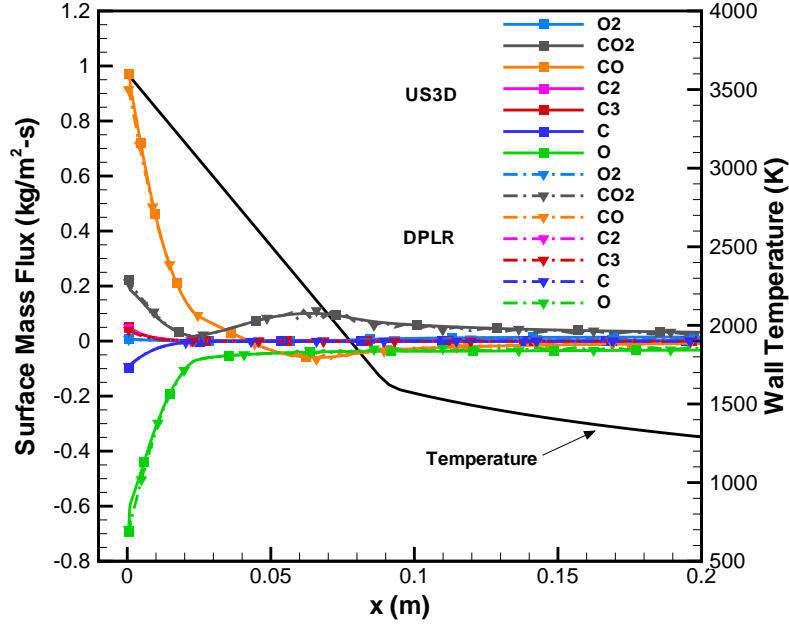
Figure 21. Comparison of species surface mass fluxes predicted by the US3D and DPLR codes using the Zhluktov and Abe ablation model.

conditions. Figure 21 shows the wall temperature distribution along with the species surface mass fluxes computed by the US3D and DPLR codes. There is excellent agreement between the codes and verifies the implementation of the ZA model in US3D.

4.3 Influence of Nitridation

The following figures will display results for the four different cases considered at the four freestream conditions. The original ZA model without nitridation is iden-

tified as the baseline model. The modified ZA model includes the direct nitridation reaction and the surface participating nitridation reaction which are identified as "ER nitridation" and "Arrh nitridation", respectively, due to the reaction types.

4.3.1 Surface Mass Flux Comparison.

First, the total mass flux from the surface is compared as a function of surface distance measured from the stagnation point. Figure 22 plots this quantity and shows that at strong sublimation conditions (20 km), all results gave similar total mass fluxes near the stagnation point, with the ZA model (with or without nitridation) being about 10% higher. Further along the surface, as the wall temperature cools, the effect of direct nitridation is seen where there is an increase in mass loss rate over a short surface distance compared to the baseline model. The effect of direct nitridation becomes more significant as the wall temperatures and pressures are lowered at the higher altitude conditions and as sublimation becomes more of an inconsequential reaction. The largest impact of direct nitridation occurred at the 30 km condition where it increased the surface mass flux at the stagnation point by about 154% compared to the baseline model. In comparison, the Park model had an approximate 46% higher mass flux than the baseline model. Even though there are substantial increases to the mass fluxes caused by direct nitridation, it does not necessarily translate to significant increases in gaseous CN concentrations. For most cases, the modified ZA mass loss rates relax to the baseline values beyond the nose of the sphere-cone geometry. Clearly, the surface participating nitridation reaction had a very minimal effect compared to the baseline model and did not alter any mass loss rates or gas-phase species compositions as will be shown in subsequent figures.

The carbon-bearing species surface mass fluxes are plotted in Figures 23-29 for each test condition. At the 20 km condition, the baseline and modified ZA model
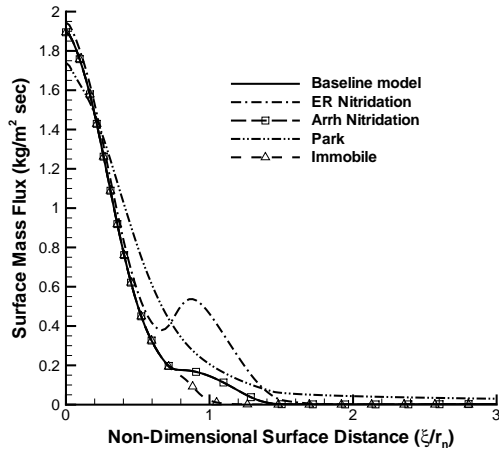
(a) 20 km
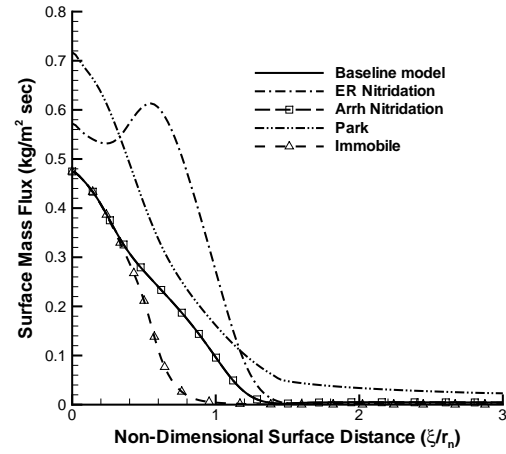
(b) 25 km
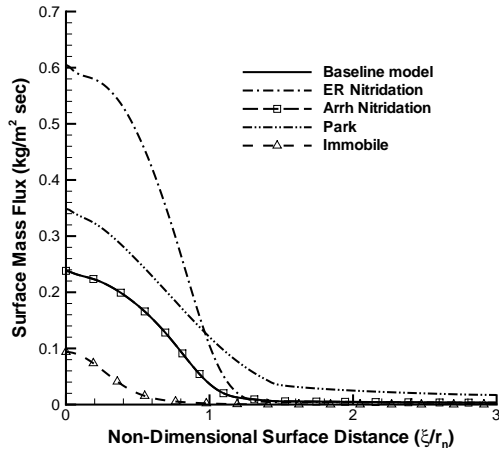
(c) 30 km
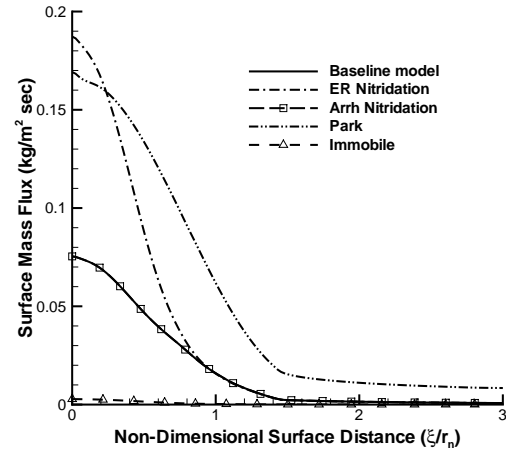
(d) 40 km

Figure 22. Predicted total surface mass flux as a function of normalized distance from stagnation point.

91

shows that C_3 formation is the dominant surface reaction at the stagnation point, but the Park model has relatively equal mass flux contributions from C_3 sublimation and nitridation. Furthermore, the Park model produces less C_3 than the ZA models. The ZA models have C_2 and C recombining at the surface, whereas the Park model has zero mass flux for both of these species at the stagnation point. However, as noted above, the Park model has no mechanism for C_2 formation or C recombination on the surface, which will become an important distinction at the higher altitude conditions. The Park model shows significant CN production around the entire nose of the geometry, but the modified ZA model with direct nitridation only has CN forming around the sphere-cone juncture.

For the 25 km case, oxidation and nitridation become more important closer to the stagnation point while the level of sublimation decreases for the modified ZA model. The CN formation rate has increased near the stagnation region, but it has also caused the amount of oxidation to decrease compared to the baseline model. Sublimation and nitridation remain the dominant reactions for the Park model. Also, the Park model predicts approximately zero CO production. At the stagnation point, the Park model predicts four times as much CN formation compared to the modified ZA model. The level of nitridation becomes similar between the Park and modified ZA models at the 30 km condition, which is shown in Figure 27. Interestingly, the production of CN is now 15% higher at the stagnation point for the modified ZA model compared to the Park model. The amount of oxidation predicted by the modified ZA model near the stagnation point is also substantially reduced compared to the baseline model. There are relatively large levels of C recombination at the wall with direct nitridation, which will affect the CN concentrations in the near-wall boundary layer. In contrast, the Park model shows nitridation as the only relevant surface reaction for this test condition.
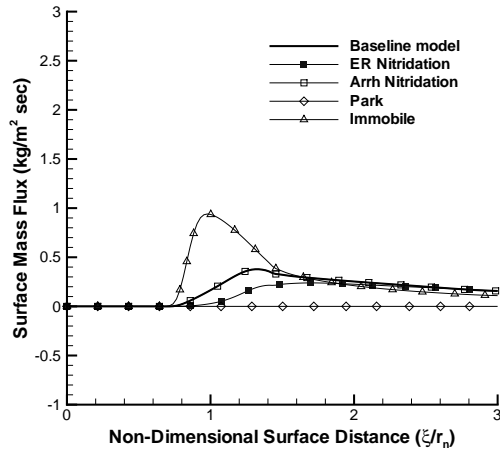
(a) CO_2
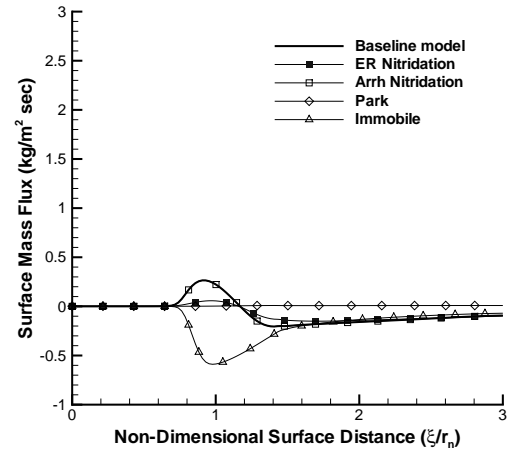
(b) CO
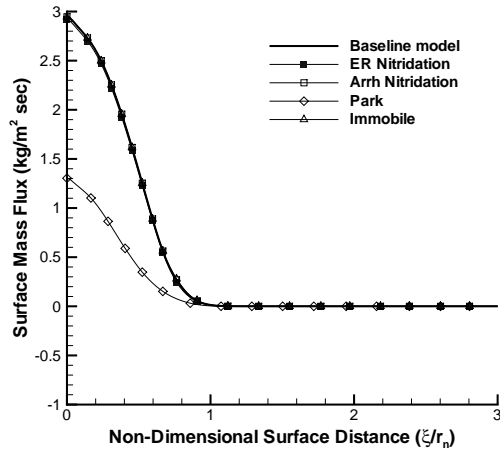
(c) C_3
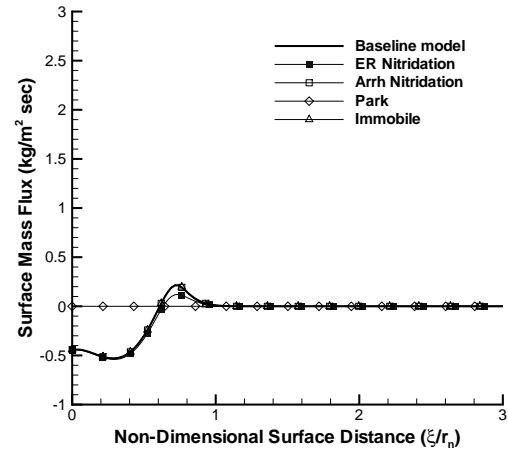
(d) C_2

Figure 23. CO_2, CO, C_3, and C_2 surface mass fluxes as a function of normalized distance from stagnation point at 20 km conditions.
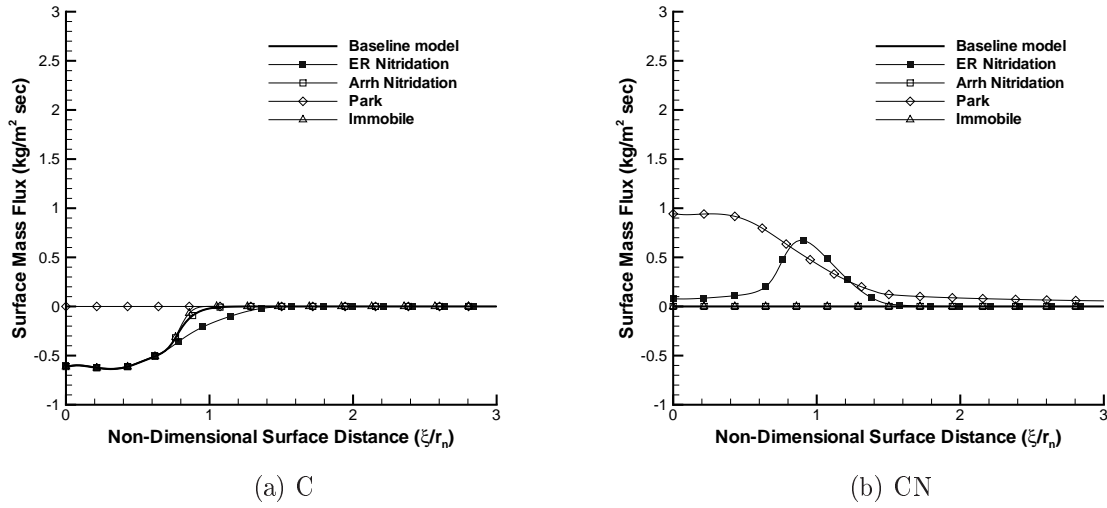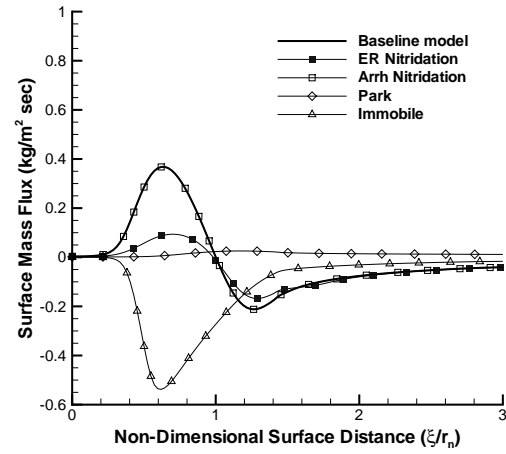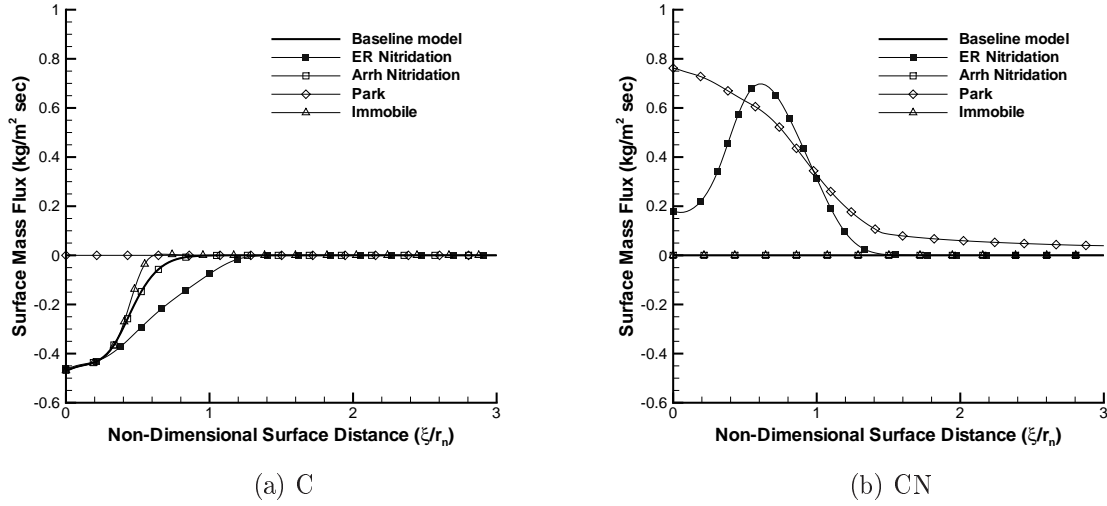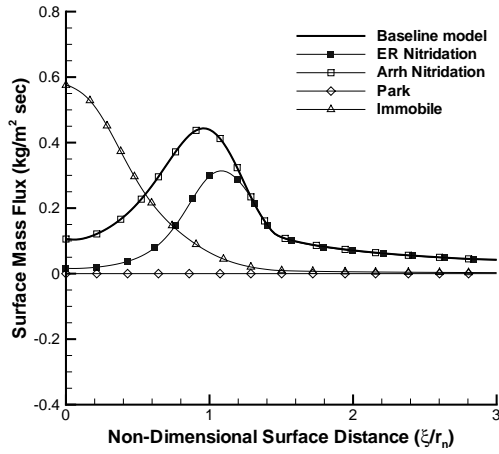
Figure 24. **C and CN surface mass fluxes as a function of normalized distance from stagnation point at 20 km conditions.**

The competition between the oxidation and nitridation processes is further highlighted in Figure 29, which shows the 40 km species surface mass fluxes. Now, CO_2 formation is the dominant surface reaction with nitridation still contributing to the total mass flux for the modified ZA model. The ZA models predict CO to recombine at the surface, which is opposed to the Park model that predicts CO production. The CN production rate for the Park model has again overtaken the modified ZA model being 60% higher at the stagnation point. Thus, even though the total mass flux at the stagnation point for the Park and modified ZA models is fairly close (within 10%), the mechanisms are completely different.

The previous analysis has shown that nitridation can be as or more important of a surface reaction as oxidation and sublimation under certain simulated re-entry conditions. The implemented direct nitridation mechanism proved to have a more significant impact on surface mass fluxes than the surface participating nitridation mechanism. The reason is due to a lack of N adsorbing to the surface, which is a precursor step for the nitridation reaction. For all of the test conditions, the mass flux
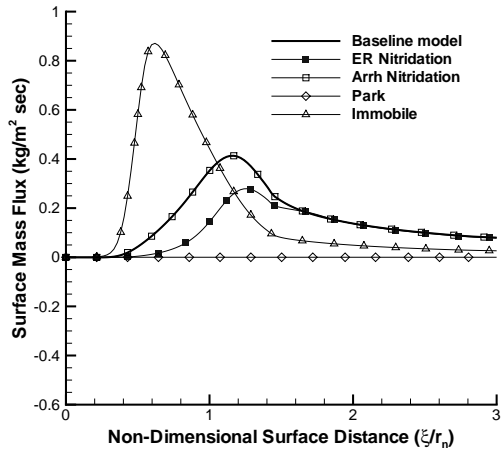
(a) CO_2

(b) CO
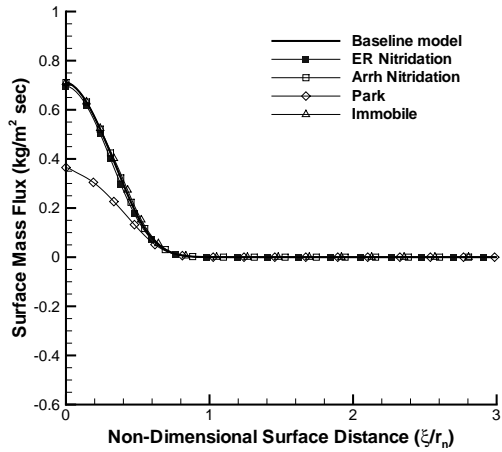
(c) C_3
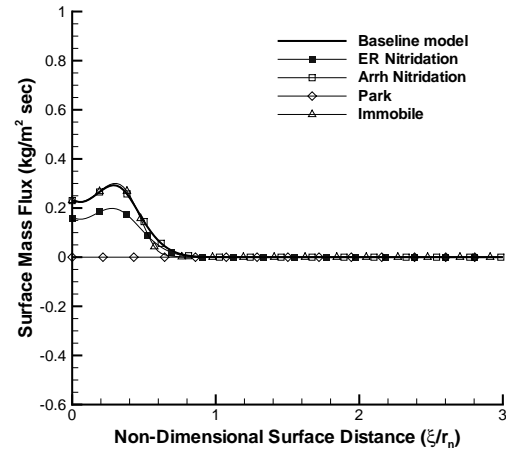
(d) C_2

Figure 25. CO_2, CO, C_3, and C_2 surface mass fluxes as a function of normalized distance from stagnation point at 25 km conditions.

Figure 26. C and CN surface mass fluxes as a function of normalized distance from stagnation point at 25 km conditions.

of N either away or towards the surface was essentially zero. The effect of nitridation can be further assessed by considering Figures 30-33, which plot select gas-phase species concentrations in the boundary layer. The figures will focus on how the CN mass fraction changes between the different models.

4.3.2 Species Mass Fraction Comparison.

Figure 30 plots the species mass fractions as a function of distance from the surface at the stagnation point for the 20 km case. Note that the same gas-phase chemistry model was used with each surface reaction model. The initial mass fractions at the surface reflect the surface mass flux results. Therefore, C_2 and CN have higher fractions at the wall for the Park model and C_3 is higher at the wall for the ZA models. C_2 and CN form from C_3 immediately away from the surface. Then, as the amount of C_3 continually diminishes, the concentrations of C_2 and CN also rapidly decline. The ZA and Park models predict similar CN mass fraction profiles due to the differences in C_3 and CN production rates. Even though the amount of CN formation at the

(a) CO_2
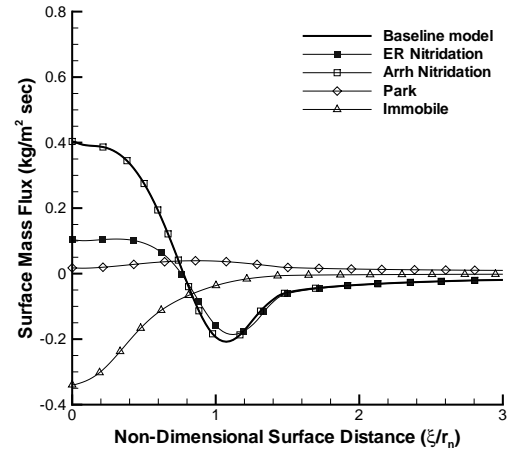
(b) CO
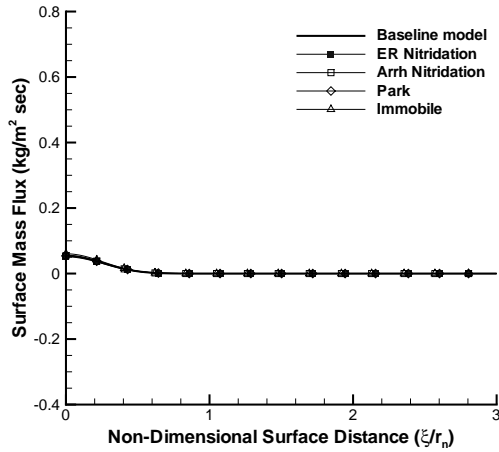
(c) C_3
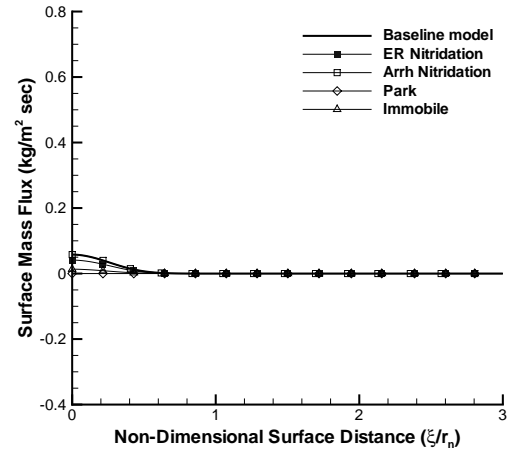
(d) C_2

Figure 27. Species surface mass fluxes as a function of normalized distance from stagnation point at 30 km conditions.
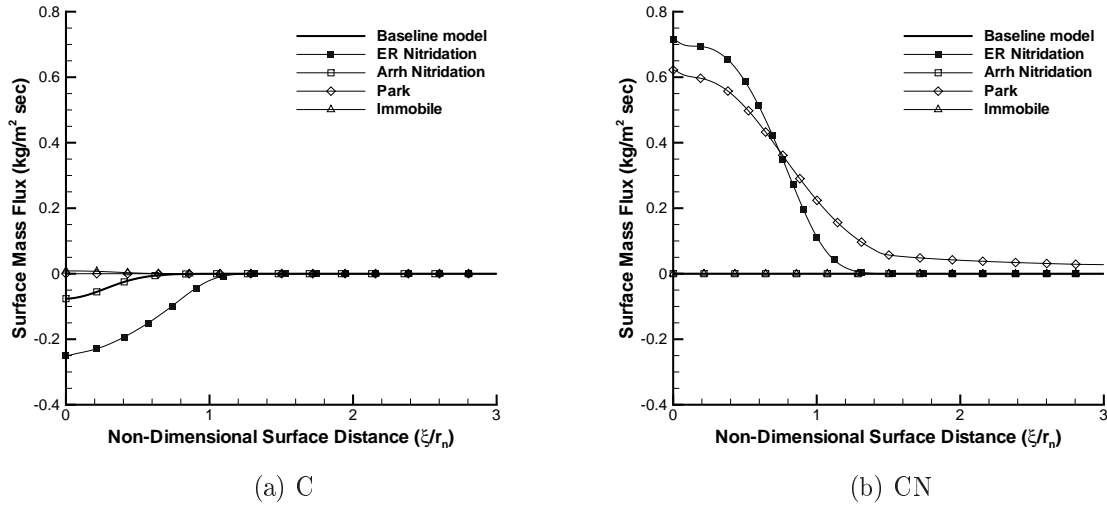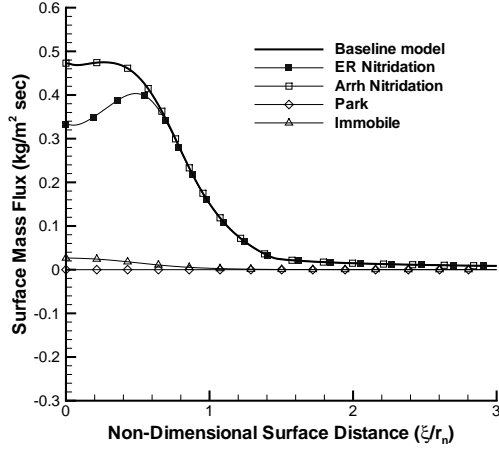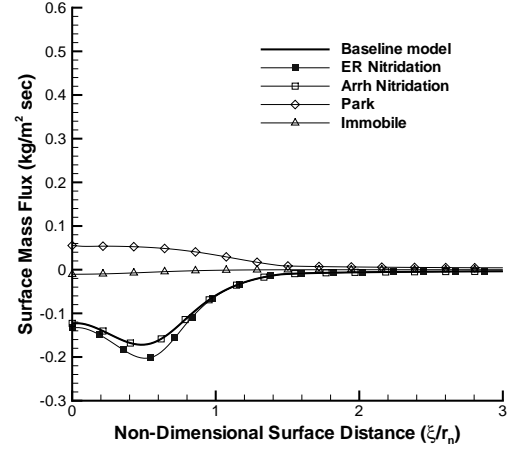
Figure 28. C and CN surface mass fluxes as a function of normalized distance from stagnation point at 30 km conditions.

stagnation point is much lower for the ZA model than the Park model, the higher levels of C_3 predicted by the ZA models accelerate CN formation in the gas-phase. In Figure 31 for the 25 km case, the CN mass fraction profiles are due to the amount of nitridation that occurred at the surface for either ablation model and the dissociation rate of CN determined from the gas-phase chemistry. Note the large difference in C concentration between the Park and ZA models, which is a common result at all freestream conditions and will have a strong influence on CN concentrations at the higher altitudes.

At the two highest altitude conditions, the ability of C to recombine at the surface is the primary discrepancy between the resulting CN mass fraction profiles. Figures 32 and 33 show the species mass fractions for the 30 km and 40 km cases. Again, for these cases the oxidation and nitridation mechanisms are the most dominant surface reaction processes. It is interesting to observe the concentration of CN is higher for the Park model than the ZA model with direct nitridation because the CN mass flux at the stagnation point was higher for the ZA model. However, this can be explained
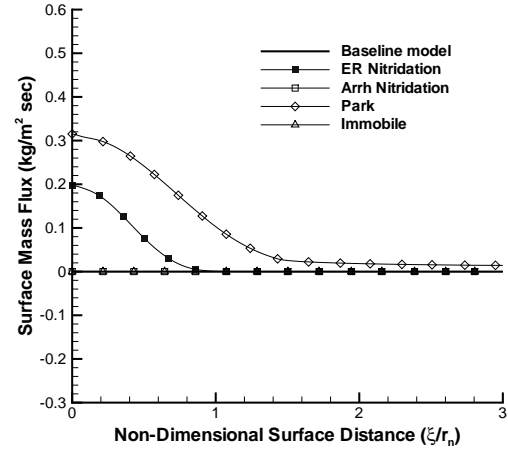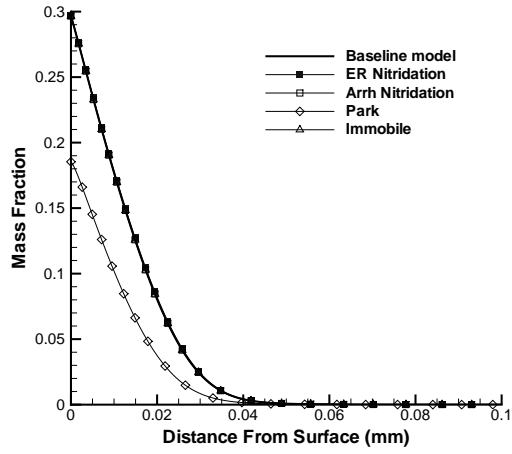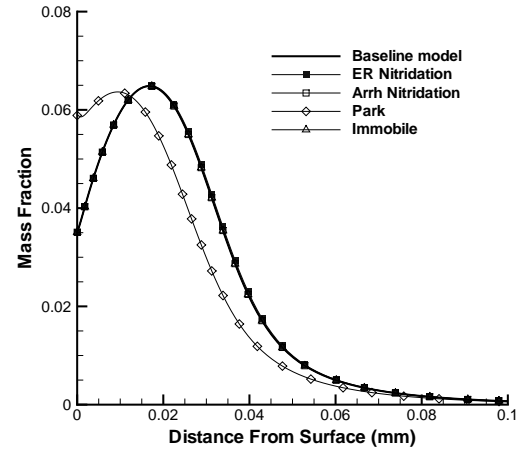
(a) CO_2

(b) CO
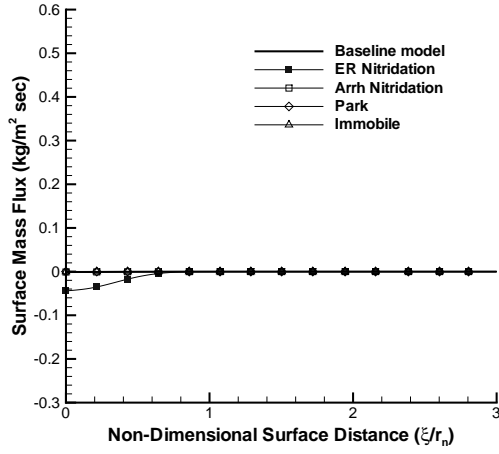
(c) C

(d) CN

Figure 29. Species surface mass fluxes as a function of normalized distance from stagnation point at 40 km conditions. At these conditions, there is no flux of C_3 or C_2 for any model considered.
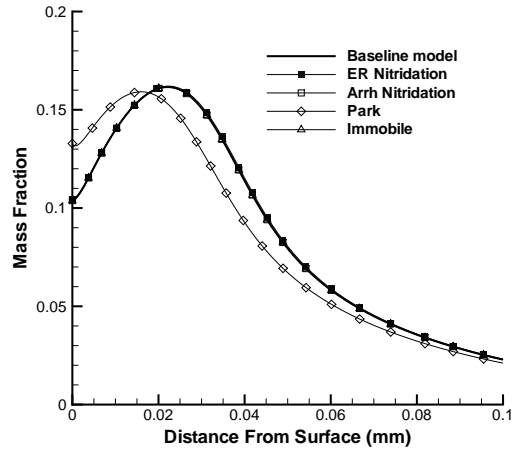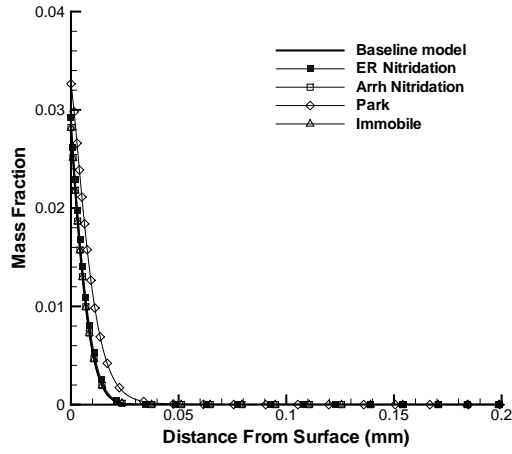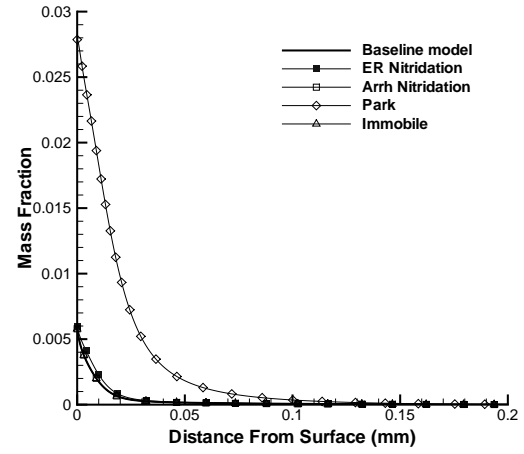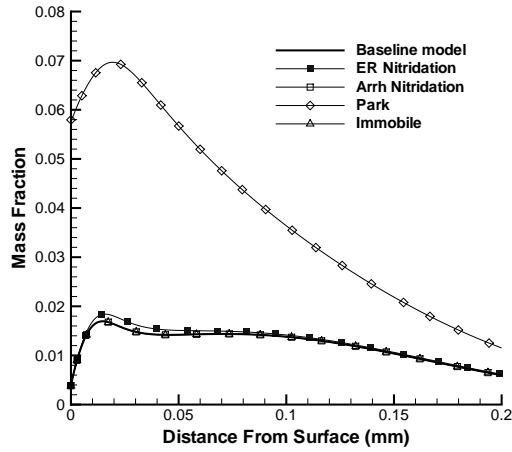
(a) C_3

(b) C_2

(c) CN

Figure 30. Species mass fractions as a function of surface-normal distance at the stagnation point at 20 km conditions.
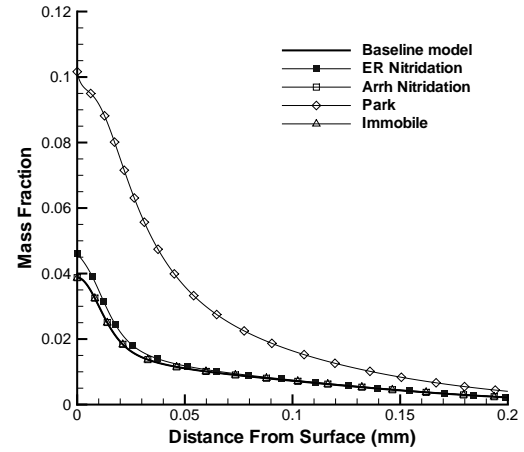
(a) C_3

(b) C_2

(c) C

(d) CN

Figure 31. Species mass fractions as a function of surface-normal distance at the stagnation point at 25 km conditions.

(a) CO_2

(b) CO

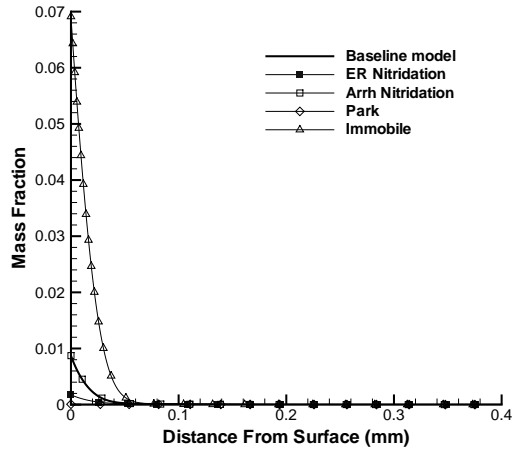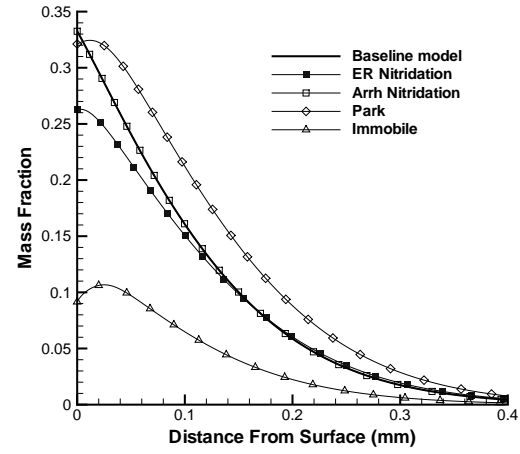(c) C

(d) CN
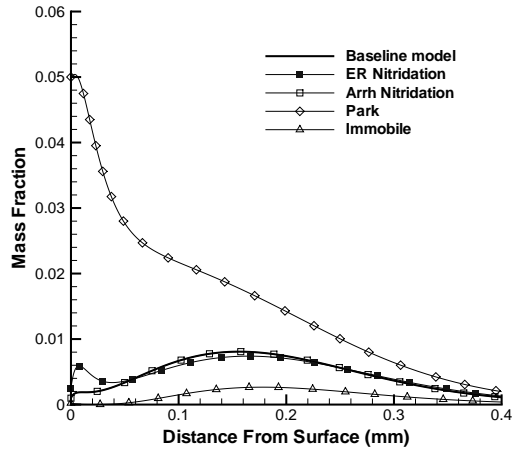
Figure 32. Species mass fractions as a function of surface-normal distance at the stagnation point at 30 km conditions.

(a) CO$_2$

(b) CO

(c) C

(d) CN

Figure 33. Species mass fractions as a function of surface-normal distance at the stagnation point at 40 km conditions.

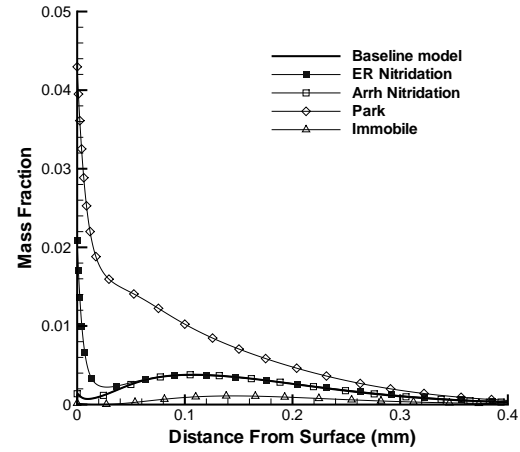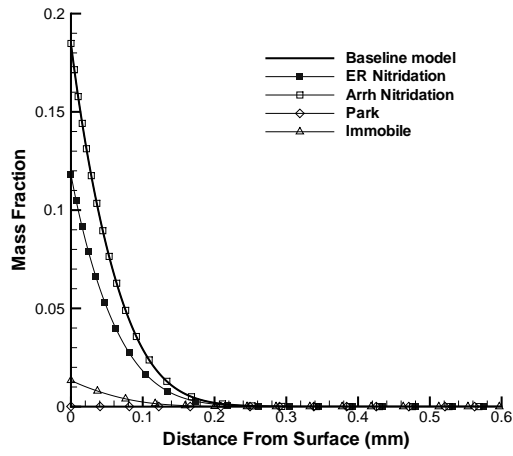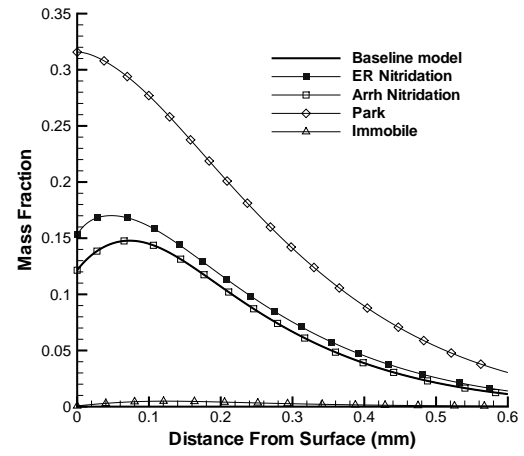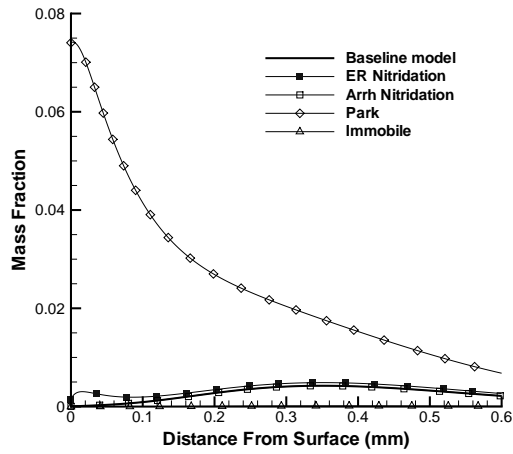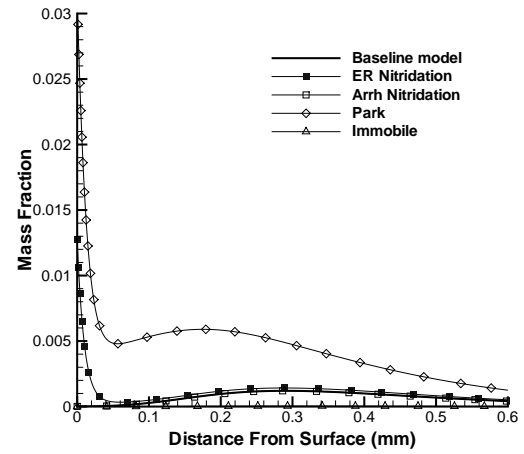by comparing the C mass fraction. The Park model predicts relatively more C in the boundary layer than the ZA model, which in turn produces more CN due to the gas-phase reaction $N_2 + C \leftrightarrow CN + N$. At these freestream conditions, only a small amount of N_2 dissociates across the shock, so it is readily available to react with C in the boundary layer. A similar conclusion can be drawn for the results at the 40 km condition shown in Figure 33. The Park model consistently predicts a higher CN mass fraction in the boundary layer than the modified ZA models. The larger C mass fraction is again a main contributor to this difference, but additionally, the CN surface mass flux at the stagnation point for the Park model is also higher than the direct nitridation ZA model. All of these results stem from the species that are allowed to react at the surface and the preferred direction of reactions, defined in the ablation models.

4.3.3 Nitridation Comparison.

The surface temperatures and pressures at which nitridation is or is not active for the direct nitridation ZA model are shown in Figure 34 to further differentiate the nitridation mechanisms from the Park model. By comparing all four plots, it is fair to say that the nitridation rate has a stronger temperature dependence than pressure dependence. Direct nitridation is most active between surface temperatures of approximately 2000-4000 K, with a consistent maximum around 3600 K. As the temperature approaches and goes below 2000 K, the nitridation rate goes to zero. The rate also appears to go to zero as the temperatures reach 4600 K. In contrast, the Park model nitridation rate remains relatively constant at very high wall temperatures above 4000 K. The rate does decrease as the temperature decreases but with a smaller slope than the direct nitridation ZA model. Even as temperatures decrease below 2000 K, the Park model predicts a CN mass flux greater than zero, whereas the

direct nitridation rate goes to zero.

4.4 Surface Adsorption Process

The effect of assuming the surface adsorption process as mobile or immobile is analyzed for each test condition. The baseline ZA model assumes mobile adsorption, but there is no direct experimental evidence that it dominates at all conditions. Therefore, the limiting case of immobile adsorption is studied to understand the sensitivity of the ablation process to the surface mobility. Figures 22-33 display the surface mass fluxes and species mass fractions under the assumption of immobile adsorption at each test condition.

At the lower altitude conditions, the immobile adsorption solution predicts a similar surface mass flux (total and species specific) as the solution predicted with a mobile adsorption assumption near the nose of the sphere-cone geometry. There is a significant reduction in the total surface mass flux for the higher altitude cases with the assumption of immobile adsorption. In fact, immobile adsorption reduces the mass loss rate to almost zero over the entire surface for the 40 km case. The inability of oxygen and nitrogen atoms to diffuse across the surface reduced reaction probabilities and, when combined with the much lower surface temperatures and pressures of the 40 km case, generated very little mass loss.

The oxidation reactions are affected the most under an immobile assumption for all test conditions, while the sublimation reactions are altered slightly for the 30 km test condition. When comparing the mobile and immobile CO_2 and CO mass fluxes, immobile adsorption has the tendency to increase CO_2 levels and causes CO to recombine at the surface. Mobile adsorption predicts the opposite and shows CO formation at similar surface locations as shown in Figures 23b, 25b, and 27b. The CO_2 and CO mass fractions along the stagnation streamline also highlight these differences.

105
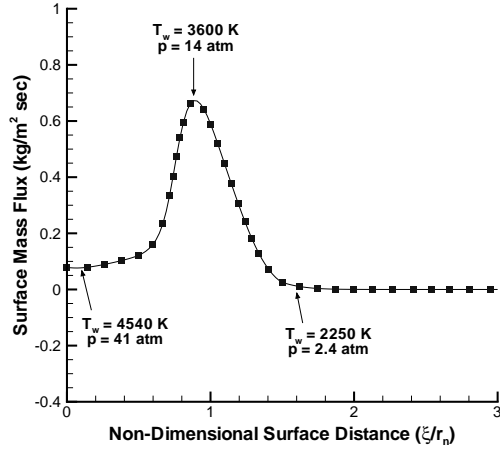
(a) 20 km
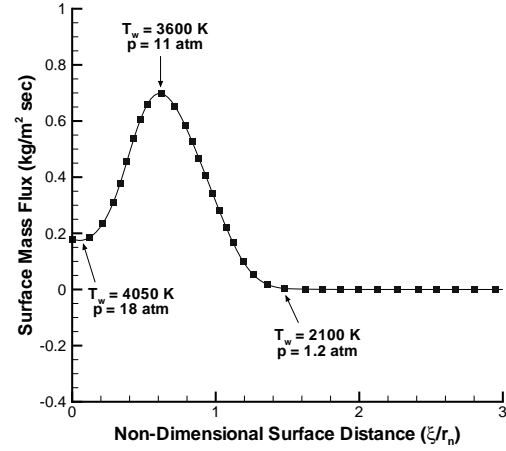
(b) 25 km
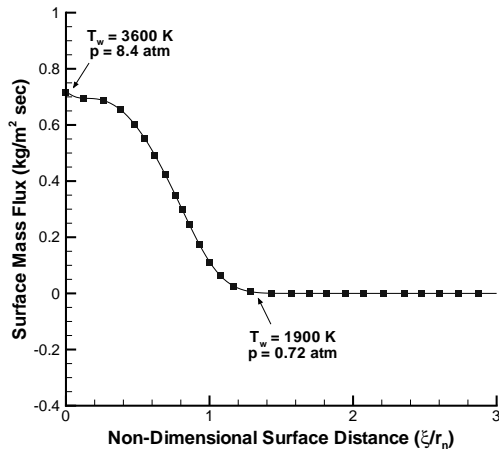
(c) 30 km

(d) 40 km

Figure 34. CN surface mass fluxes as a function of surface-normal distance at the stagnation point for each test case using the modified Zhluktov and Abe model with the Eley-Rideal nitridation mechanism. Displaying the surface temperatures and pressures at specific locations.
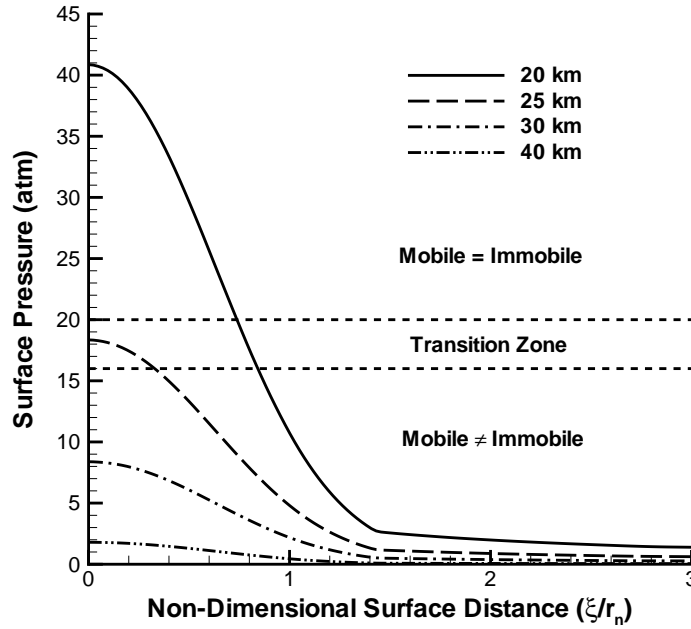
Figure 35. Surface pressure distributions for representative re-entry cases.

As expected, the sublimation dominated test conditions at 20 and 25 km have no changes to any of the predicted species mass fractions since the stagnation point mass loss rates are identical for mobile and immo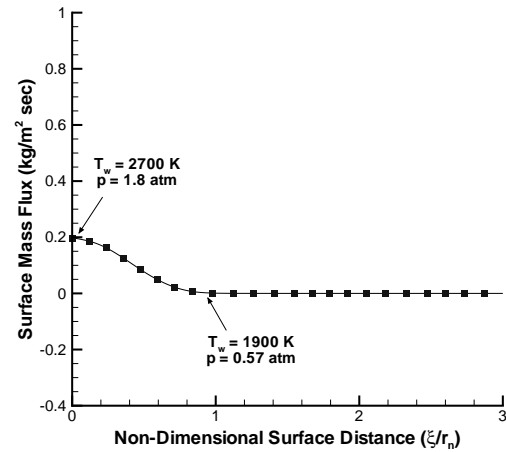bile adsorption. Since immobile adsorption predicts strong CO recombination at the stagnation point for the 30 km case, the CO mass fraction at the wall is reduced by 73% compared to the mobile adsorption prediction. The amount of CN is also reduced due to the lower concentrations of CO. For the 40 km case, there are significantly reduced levels of both CO_2 and CO for immobile adsorption, and the surface is essentially a non-reactive, as compared to the mobile adsorption predictions.

The conditions at which mobile and immobile adsorption would be expected to provide similar results are correlated with the surface pressure and possibly also with the surface temperature. Figure 35 plots the surface pressure distributions for each test condition. Comparing this plot with Figures 22-29, any surface pressure above

approximately 20 atm produces similar surface reaction processes independent of a mobile or immobile adsorption assumption. Conversely, any surface pressure below approximately 16 atm produces different oxidation mechanisms dependent on a mobile or immobile assumption. A transition zone occurs in between these pressures where the surface temperature may have an influence on the relevant oxidation processes. When the surface pressure is in this transition region and the surface temperature is at sublimation conditions, immobile adsorption tends to predict higher levels of CO_2 formation and CO recombination as compared to mobile adsorption. However, when the surface pressure is in this transition region and the surface temperature is near oxygen saturation conditions, the predicted species mass loss rates are similar for mobile and immobile adsorption. Hence, the differences in the species mass fluxes are correlated with the surface pressure and temperature, but the total surface mass flux appears to be directly correlated with the surface pressure, as seen in Figure 22.

4.5   Surface Site Concentration Sensitivity

One of the key attributes of the ZA model that differentiates it from other ablation models is the specification of a finite number of surface reaction sites. The surface reaction site concentration is also called the "active site density" and is usually defined with the parameter Φ. Different grades of graphite exhibit large property variations because of different impurity levels, grain sizes, grain boundaries, and structure (amorphous or highly-oriented), which complicate gas-surface interaction studies [134]. Determining the sensitivity of Φ, or characterizing an ablative surface in general, is essential to any surface reaction study because it could have a direct impact on the level of oxidation predicted by the ZA model. In fact, this is probably the most difficult parameter to determine for any system. The surface site concentration parameter could also serve as a means to control the reactivity of the graphite model.

108

The active site density of 3.5×10^{19} atoms m^{-2} (i.e. $\Phi = 5.8 \times 10^{-8}$ kmol m^{-2}) published by Zhluktov and Abe [136] was actually taken from a study performed by Blyholder and Eyring [17]. Blyholder and Eyring specified the active site density as the number of carbon atoms per cm^2 of graphite lattice. It is unknown how this value was determined, but it can be related to the physical locations where oxygen atoms tend to adsorb on a graphene sheet. Numerous studies have shown that adsorbed atomic oxygen mostly forms epoxide-like structures (C-O-C) meaning a majority of the reaction sites are located between C-C bonds [110, 11, 99].

As a simplification to this observation, several assumptions are made. First, assume a graphene sheet is arranged in a honeycomb lattice (hexagonal pattern) with a C-C atom separation distance of 0.142 nm. For this structure, the number of C-C bonds is equal to the number C-atoms for one cell. Therefore, it is assumed active sites are equivalent to C-atom locations to take advantage of known geometrical relationships. The average distance between active sites is given by Marschall et al. [67] as:

$$\Delta = \frac{1}{\sqrt{A_v \Phi}} \tag{124}$$

If the average distance is assumed to be 0.142 nm, the active site density equals 8.2×10^{-8} kmol m^{-2}. If the Blyholder and Eyring active site density is used, the average distance is equal to 0.169 nm. A more accurate average distance between active sites is found by calculating the distance between one C-atom and the other 12 C-atom nearest neighbors by considering a three-cell hexagonal structure. Using this method, the average distance is found to be 0.229 nm, which equates to an active site density of 3.2×10^{-8} kmol m^{-2}. Therefore, it has been shown that a range of active site densities could be considered depending on how reaction sites are defined.

A surface reaction site concentration sensitivity study was performed using the baseline ZA model for the 30 km test case. Five surface site concentrations were

Table 14. Surface site concentration sensitivity study parameters.

Φ $\left(\text{kmol m}^{-2}\right)$	B $\left(\text{m}^{-2}\right)$	A_{eq} $\left(\text{m}^2\ \text{kmol}^{-1}\right)$
1.0×10^{-8}	6.022×10^{18}	1.0×10^{8}
3.0×10^{-8}	1.807×10^{19}	3.33×10^{7}
5.0×10^{-8}	3.011×10^{19}	2.0×10^{7}
7.0×10^{-8}	4.215×10^{19}	1.43×10^{7}
9.0×10^{-8}	5.420×10^{19}	1.11×10^{7}

considered that encompass the range of densities derived above given in Table 14. The atomic oxygen and nitrogen adsorption equilibrium constant coefficients (A_{eq}) are also provided in Table 14 because the values change based on the value of Φ.

Figures 36-39 show the surface mass fluxes and mass fractions along the stagnation streamline. The ablation predictions are insensitive to the active site density. Even with wide variations in surface temperature and pressure, the predicted surface mass fluxes and mass fractions are essentially identical for each value of Φ. Therefore, Φ will be set to 5.8×10^{-8} kmol m^{-2} as originally published for the simulations of the X-2 experiments presented in the next chapter. In addition, the assumption of mobile adsorption will be used in the next chapter with the understanding that, in reality, some adsorbed atoms could behave as immobile. The inclusion of a direct nitridation reaction in the ZA model will also be considered in the next chapter as a means to improving the ablation predictions when compared to the X-2 experimental results.

Figure 36. Total surface mass flux as a function of normalized distance from stagnation point at different surface reaction site concentrations for the 30 km conditions.

(a) CO_2

(b) CO

(c) C_3

(d) C_2

Figure 37. CO_2, CO, C_3, and C_2 surface mass fluxes as a function of normalized distance from stagnation point at different surface reaction site concentrations for the 30 km conditions.
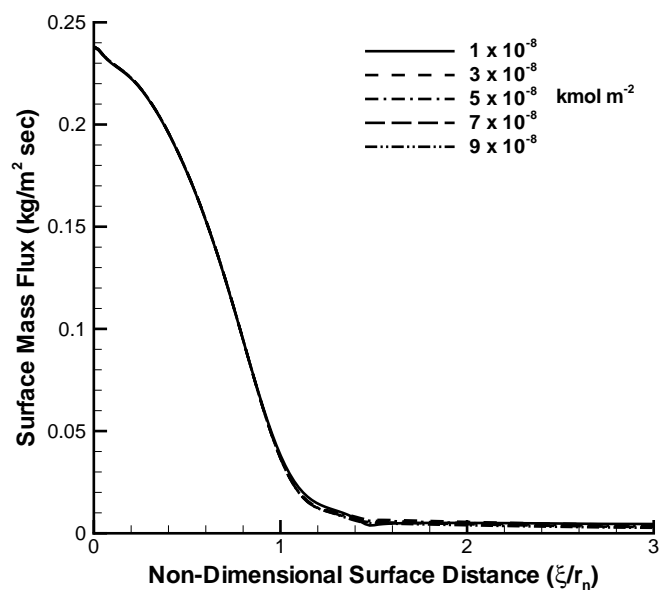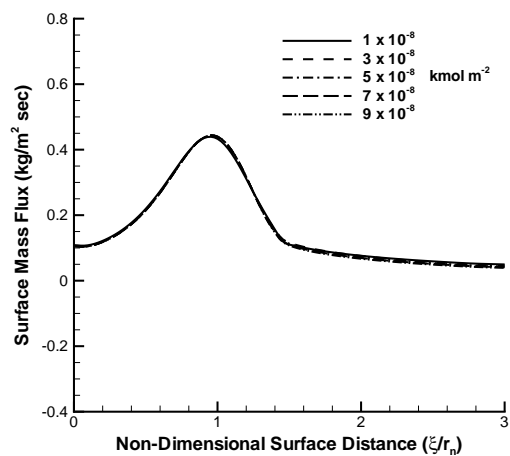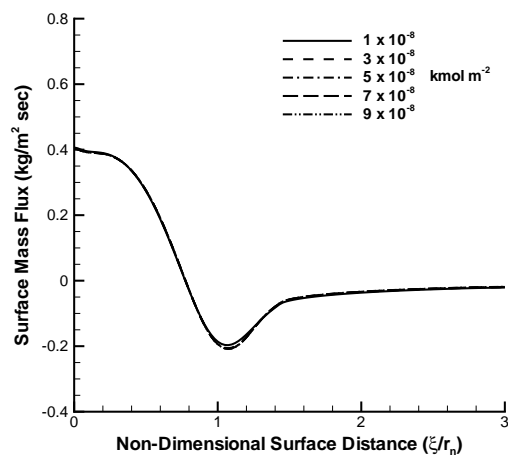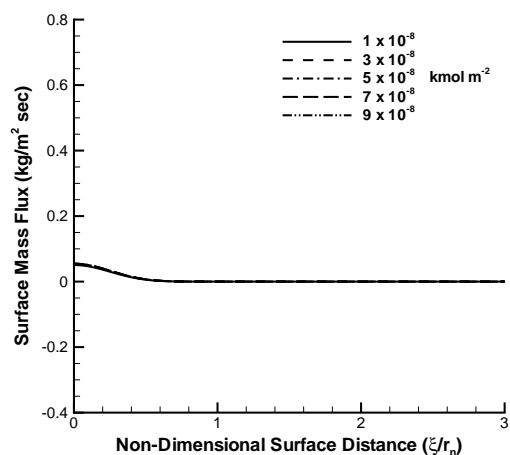
Figure 38. C surface mass fluxes as a function of normalized distance from stagnation point at different surface reaction site concentrations for the 30 km conditions.
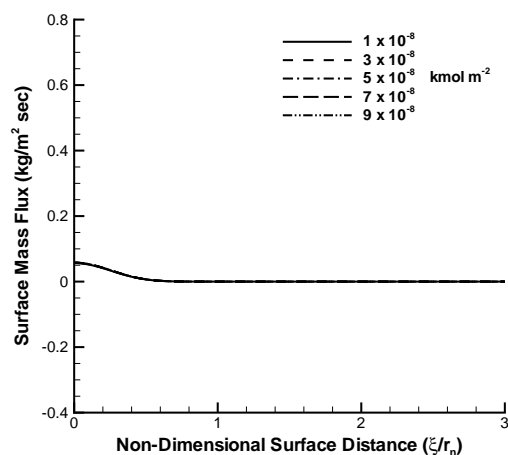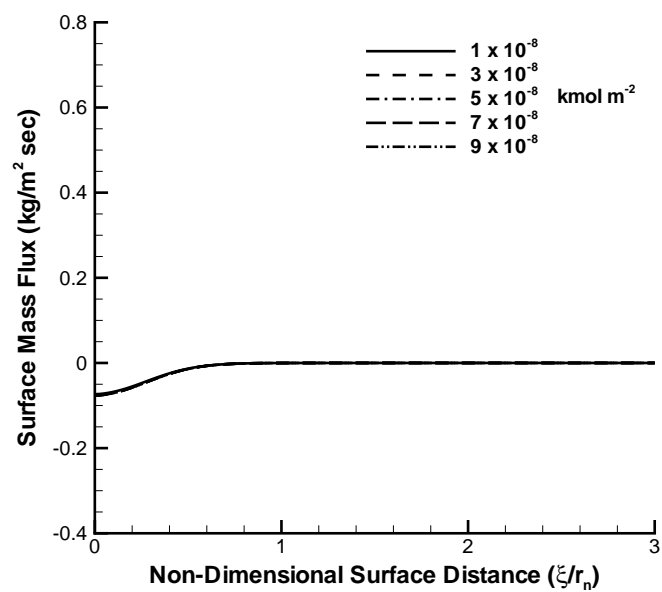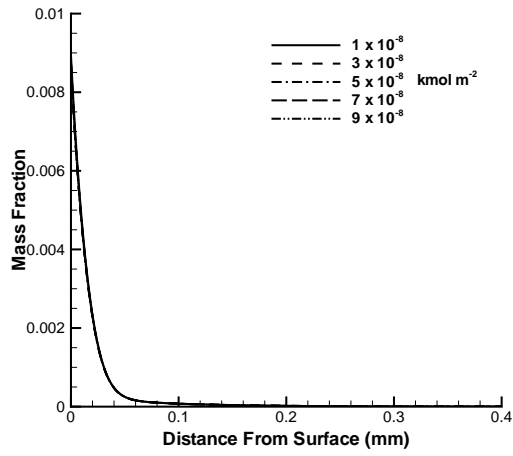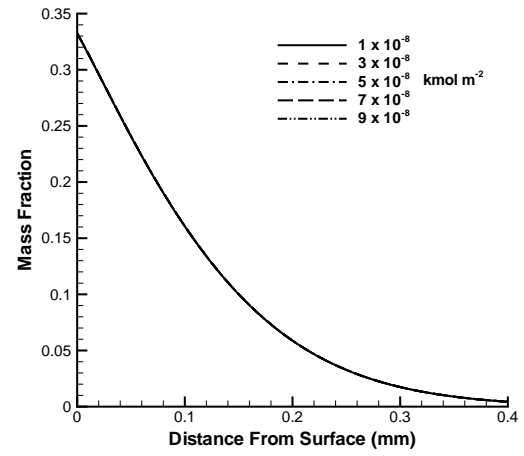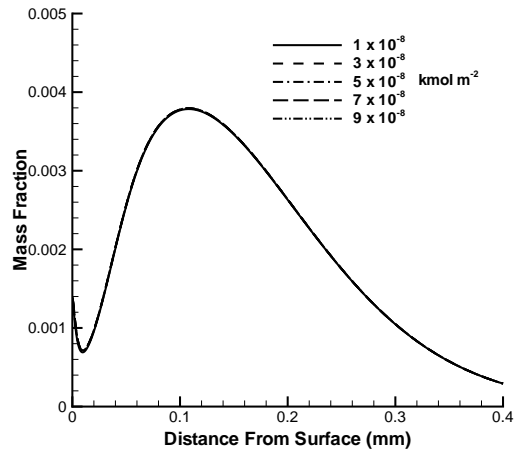
(a) CO_2

(b) CO

(c) CN

Figure 39. Species mass fraction as a function of surface-normal distance at the stagnation point at different surface reaction site concentrations for the 30 km conditions.

V. Results and Analysis

The results shown in this chapter are presented in a progressive order of the work performed. Simulations were first performed for the four wall temperature cases from the first X-2 campaign shown in Table 3 using the Park, ZA, and equilibrium (i.e. B') ablation models. The Johnston et al. [46] kinetics model was used with the equilibrium, ZA model, and the Park model modified with the nitridation efficiency proposed by Suzuki et al. [115]. Based on those results, modifications to the ZA model were proposed to improve CN radiance comparisons. The development and implementation of those modifications are presented below. Finally, simulations of the four wall temperature cases from the second X-2 campaign shown in Table 3 were completed and a discussion of those radiation comparisons is provided.

5.1 Grid Convergence

Initially, a grid convergence study was completed to ensure accurate, stable results that minimized the number of grid points and computational resources. High resolution of the mean flow was desired in the front surface of the model near the stagnation region. Hence, the number of wall normal grid points was increased in this region until mean flow parameters stabilized. Specifically the temperature, CN mass fraction, and total surface mass flux were observed with increasing grid resolution. The results of the grid convergence study are shown in Figure 40. The number of grid points in the wall normal direction was increased from 150 to 200 and 250 points corresponding to the total number of cells identified in the plots as 4.6, 5.5, and 6.4 million cells, respectively. Even though all of the grids generated similar temperature and CN mass fraction profiles, there were differences in the total surface mass flux near the stagnation point. The grid with 5.5 million cells provided similar mass fluxes

115
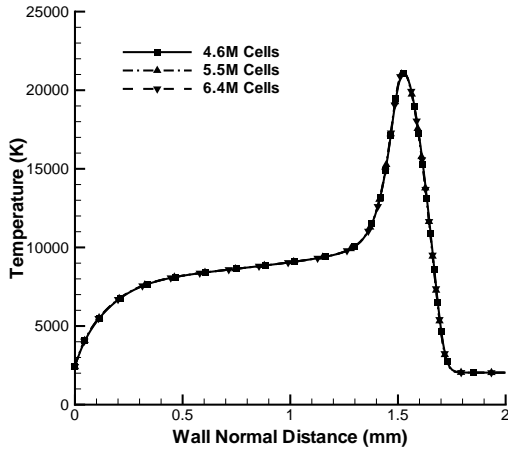
(a) Temperature
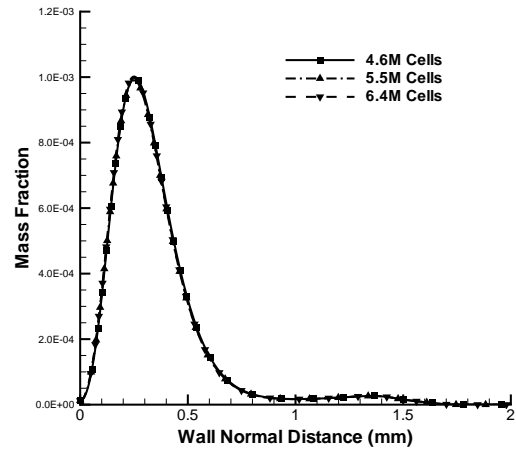
(b) CN mass fraction
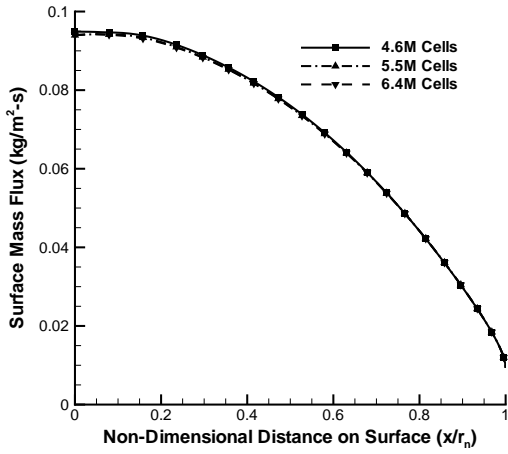
(c) Surface mass flux
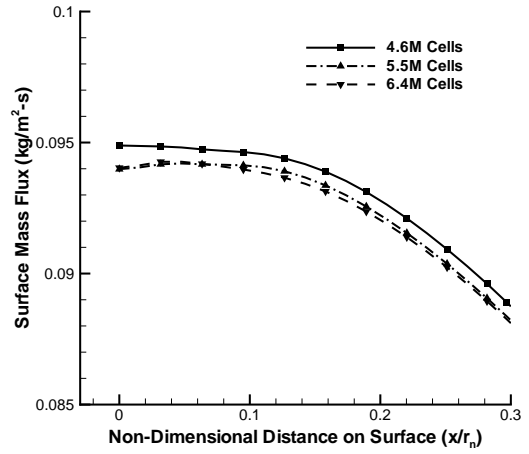
(d) Surface mass flux near stagnation point

Figure 40. Convergence of mean flow parameters with increasing grid resolution in the wall normal direction. Profiles are shown along the stagnation line.
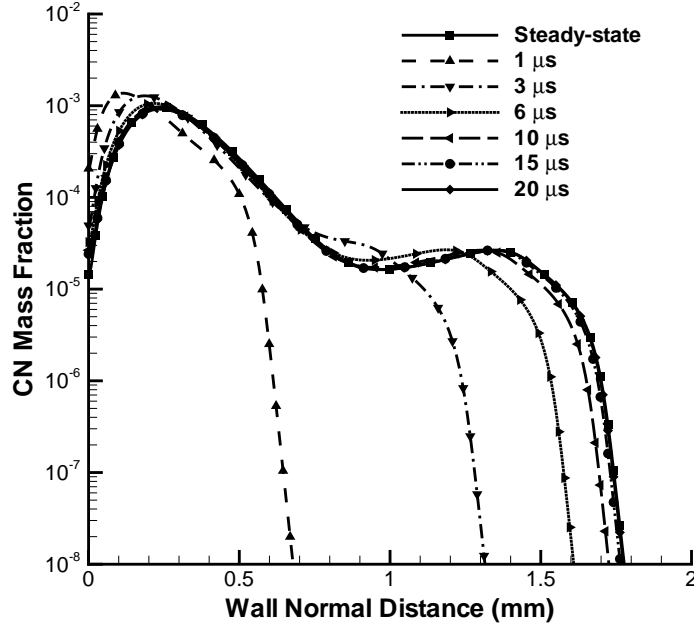
Figure 41. Unsteady CN mass fraction profiles along the stagnation line at different times after shock arrival for $T_w = 2410\,\mathrm{K}$.

as the grid with 6.4 million cells, so the following results used a grid with 5.5 million cells to conserve computational time.

Steady-state simulations were run because of the process in which the experimental data was captured. The spectrometer camera delayed for at least 20 μs after shock arrival before it started recording measurements, which allowed for the initial transient behavior to relax to steady-state. Confirmation of steady-state conditions was achieved by analyzing the high-speed video and by performing an unsteady, time-accurate simulation. Figure 41 displays the CN mass fraction profiles at multiple instances in time after shock arrival for the case with a wall temperature of 2410 K. The flow exhibits steady behavior after about 15 μs and advancing the solution further in time will only compute the same CN mass fraction profile. Therefore, calculation of steady-state solutions was deemed acceptable for these simulations.

117

5.2 First Campaign Results

5.2.1 Steady-State Flow Analysis.

The steady-state solution profiles for all wall temperatures are shown in Figure 42. The shock location is approximately 1.80 mm from the wall, and the thermal nonequilibrium region has a thickness of roughly 1 mm. Although thermal equilibrium is present within a distance of about 0.8 mm from the wall, the populations of internal energy states do not necessarily follow a Boltzmann distribution. Laux et al. [53] and Johnston [45] demonstrated that the excited electronic states of atoms are underpopulated by a factor of 10 in equilibrium regions. Due to these reasons, a non-Boltzmann distribution for the excited electronic states was assumed for all NEQAIR simulations.

The total surface mass flux at each wall temperature is plotted in Figure 43 as a function of the normalized surface distance measured from the stagnation point. The surface distance follows the model's horizontal centerline with zero corresponding to the stagnation point and is normalized by the outer diameter of the model. Overall, each respective ablation model predicted similar mass fluxes across this wall temperature range. For example, the ZA model predicted a 15% drop in the stagnation point total mass flux from $T_w = 2410$ K to 1770 K, while the Park model only predicted a 1% drop. Reducing the nitridation efficiency in the Park model had a significant effect on the total mass flux. The $T_w = 2410$ K case showed a 40% stagnation point mass flux reduction between the original and modified Park models, and similar results are seen at the other wall temperatures. As will be shown, the Park model predicts nitridation to be the dominant surface reaction at each wall temperature, which is why there is a significant reduction in surface mass flux with the modified Park model. Incorporating the Johnston gas-phase chemistry model had a minimal effect and had a tendency to slightly reduce the mass fluxes when using the ZA or
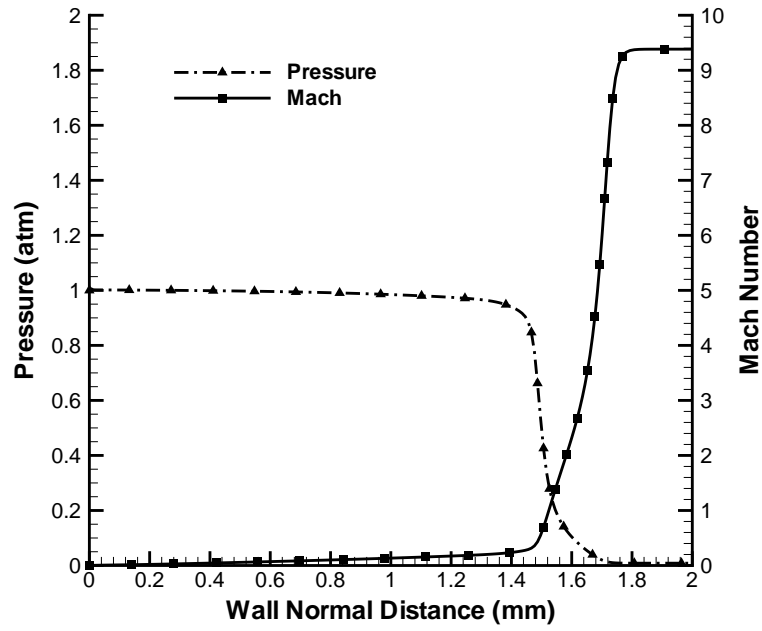
(a) Pressure and Mach Number
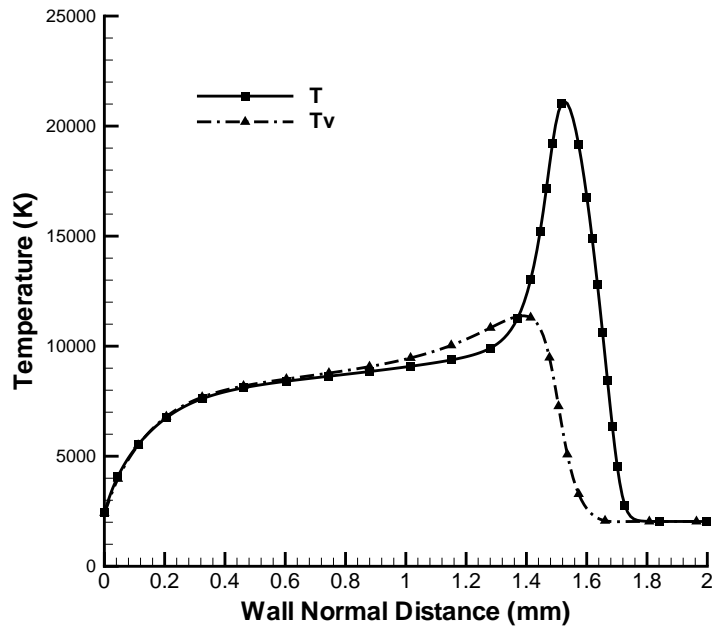
(b) Temperature

Figure 42. Steady-state solution profiles for the X-2 cases along the stagnation line.

(a) $T_w = 2410$ K

(b) $T_w = 2170$ K

(c) $T_w = 1920$ K
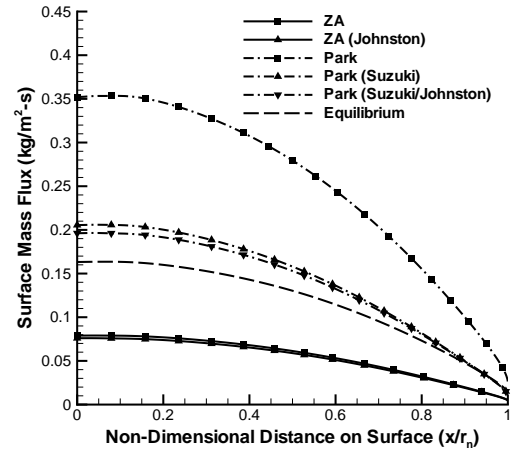
(d) $T_w = 1770$ K
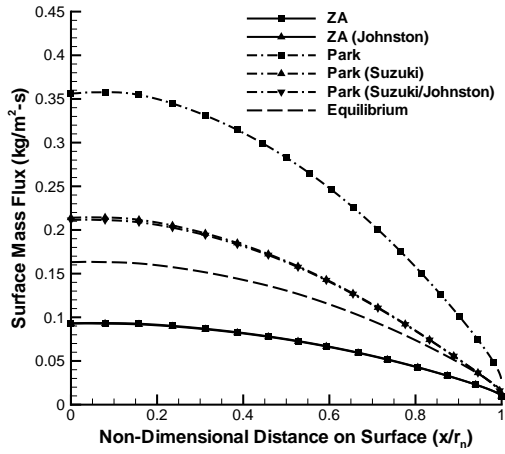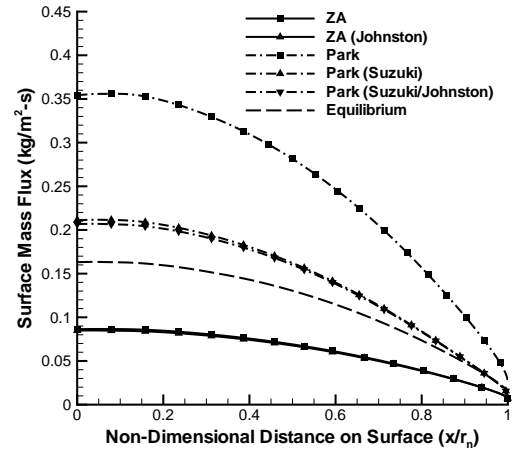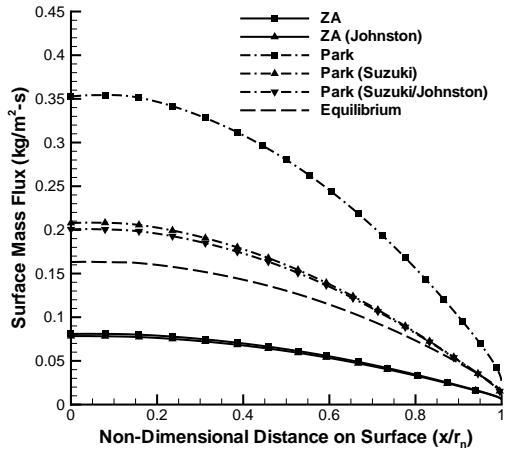
Figure 43. Predicted total surface mass flux as a function of normalized distance from the stagnation point that follows the model's horizontal centerline.

modified Park ablation model. Considering the equilibrium air-carbon mixture result shown in Figure 15b, the identical total surface mass flux profiles for the equilibrium ablation assumption was as expected for this wall temperature range. The equilibrium total surface mass fluxes fell between the ZA and modified Park ablation model predictions.

There are notable differences in the oxidation and nitridation mechanisms between the ablation models. The primary ablation products predicted by the surface models were CO_2, CO, and CN. Figures 44-47 plot the surface mass fluxes for these species. Within this wall temperature and pressure range, there was no predicted flux of C_3, C_2, and C for any model considered. A positive mass flux indicates that the species is being formed at the surface and diffuses away. A negative mass flux means the species is diffusing to the surface where it is adsorbed or reacts with the bulk carbon surface or other adsorbed surface species. For all wall temperatures considered, the ZA model predicted significant CO_2 production and had CO consumption at the surface. In contrast, the Park and equilibrium models predicted CO production as the only oxidation mechanism. The Park model predicted CN to be the primary species produced at the surface, while the ZA model has no nitridation mechanism, so it had zero CN mass flux. The equilibrium model also predicted zero CN mass flux at all surface temperatures. Applying the Suzuki nitridation efficiency to the Park model changes the relative importance of the nitridation and oxidation reactions. The modified Park model dropped the CN flux by 86% and more than doubled the CO production rate for the $T_w = 2410$ K case. The Johnston chemistry model had a negligible effect on the modified Park model results, but it did increase the CO_2 mass flux predicted by the ZA model at all wall temperatures.

The species mass fractions in the near wall boundary layer reflect the surface mass flux results and will have a direct impact on the predicted radiative heat fluxes.
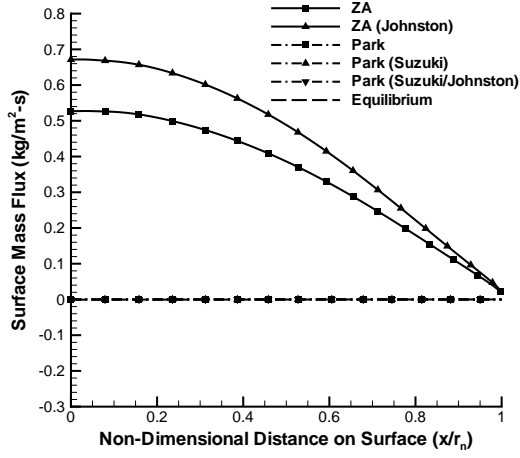
(a) CO_2
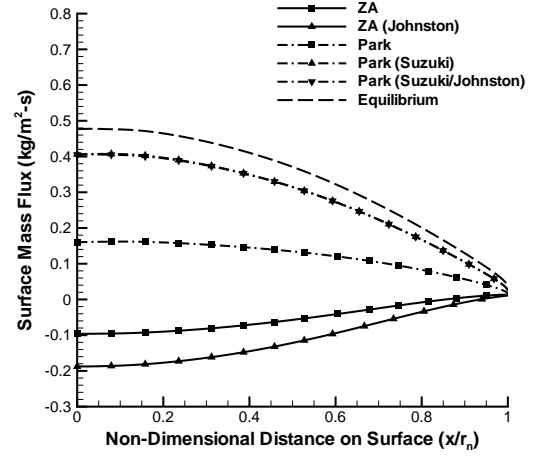
(b) CO
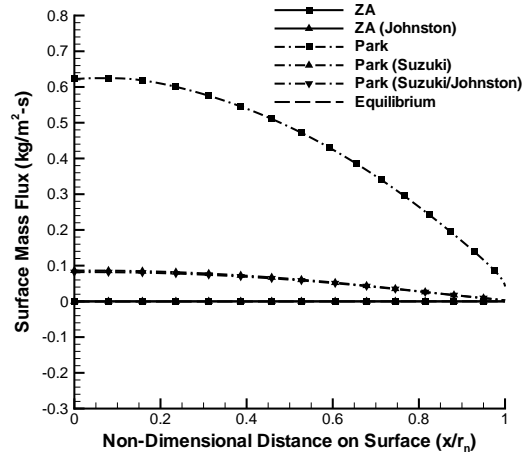
(c) CN

Figure 44. Predicted species surface mass fluxes as a function of normalized distance from the stagnation point for $T_w = 2410$ K.
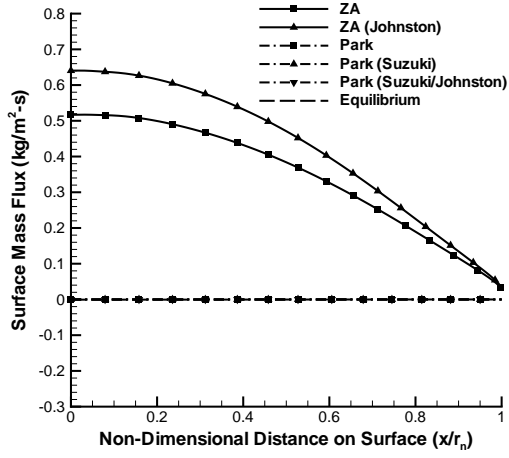
(a) CO_2
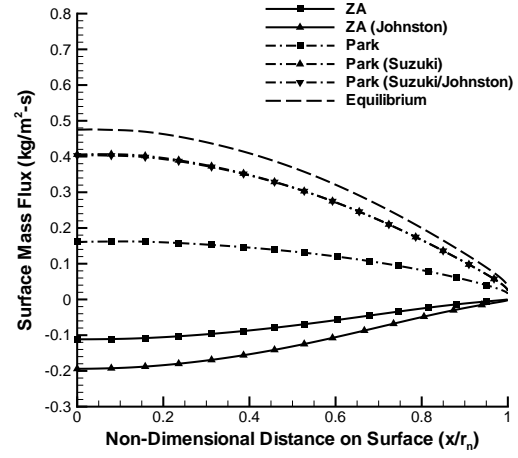
(b) CO
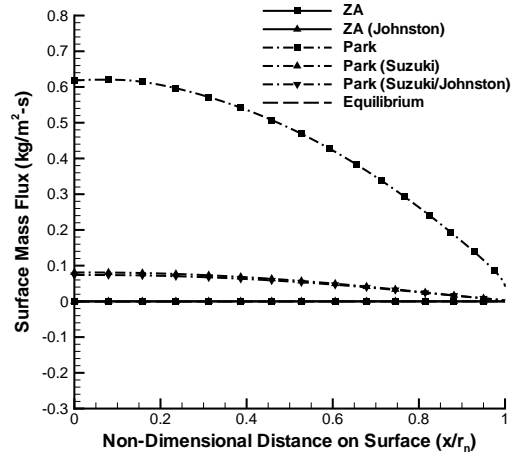
(c) CN

Figure 45. Predicted species surface mass fluxes as a function of normalized distance from the stagnation point for $T_w = 2170$ K.
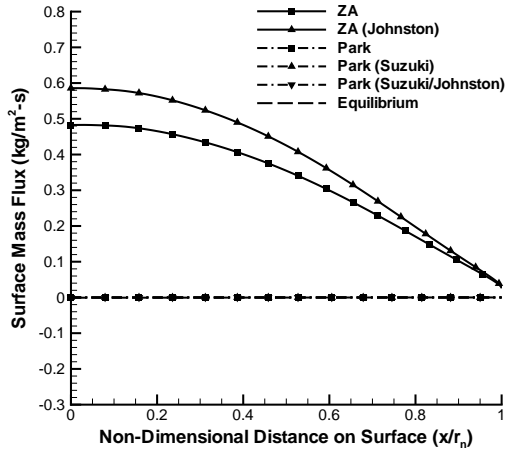
(a) CO_2
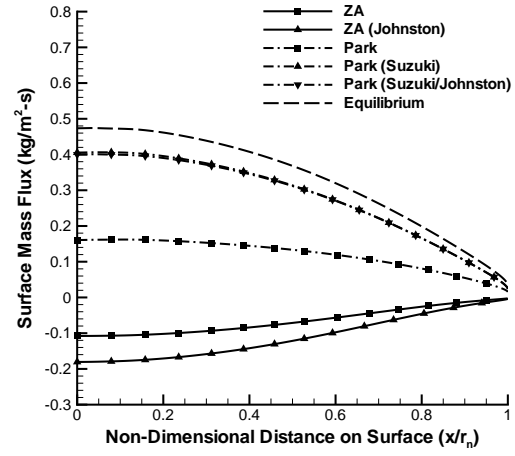
(b) CO
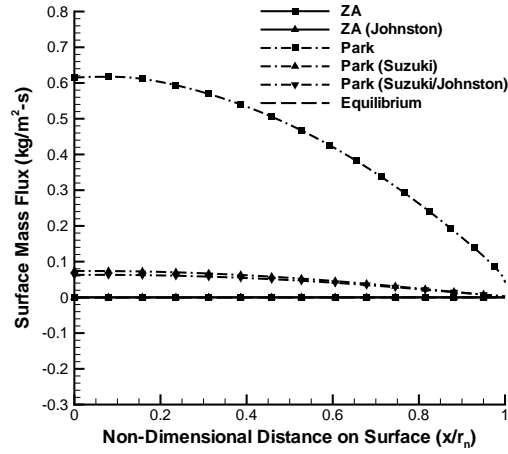
(c) CN

Figure 46. Predicted species surface mass fluxes as a function of normalized distance from the stagnation point for $T_w = 1920$ K.
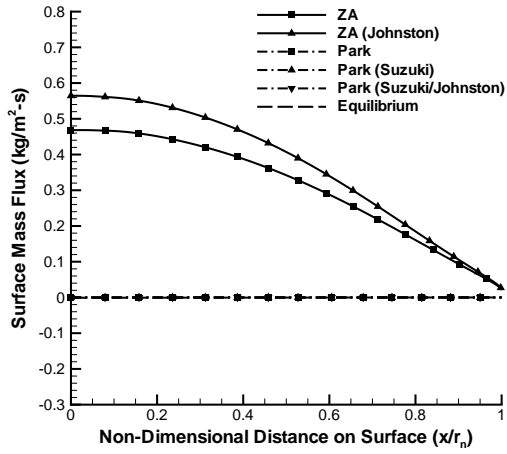
(a) CO_2
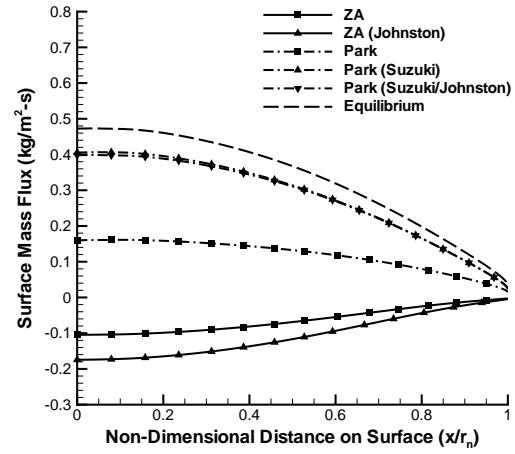
(b) CO
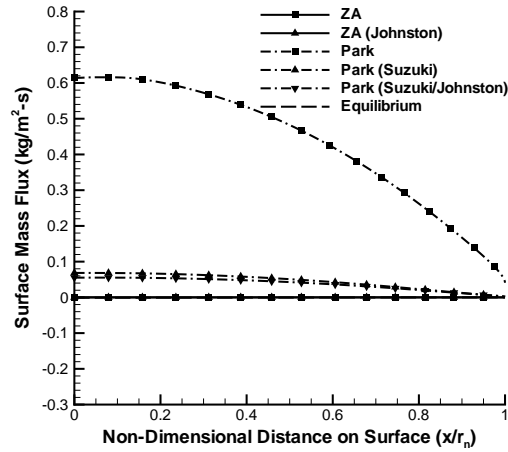
(c) CN

Figure 47. Predicted species surface mass fluxes as a function of normalized distance from the stagnation point for $T_w = 1770$ K.
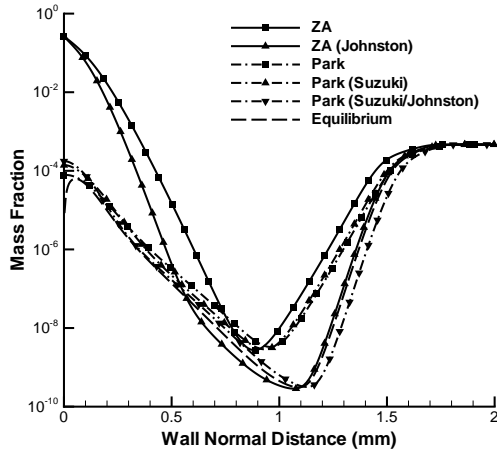
(a) CO_2
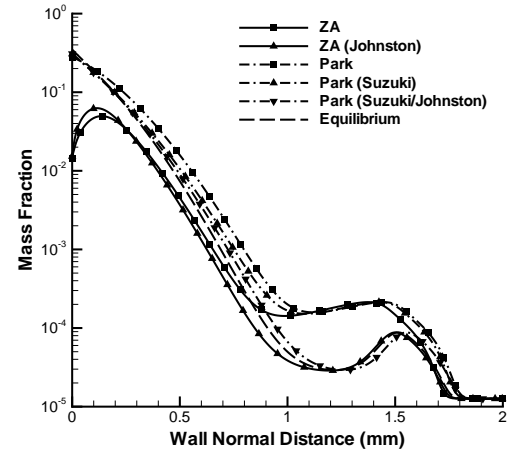
(b) CO
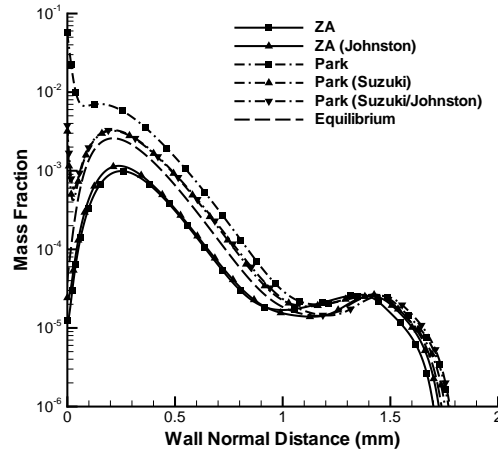
(c) CN

Figure 48. Predicted species mass fractions along the stagnation streamline for $T_w = 2410$ K.
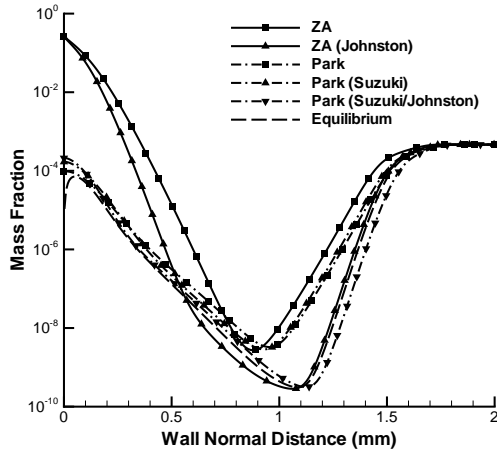
(a) CO_2
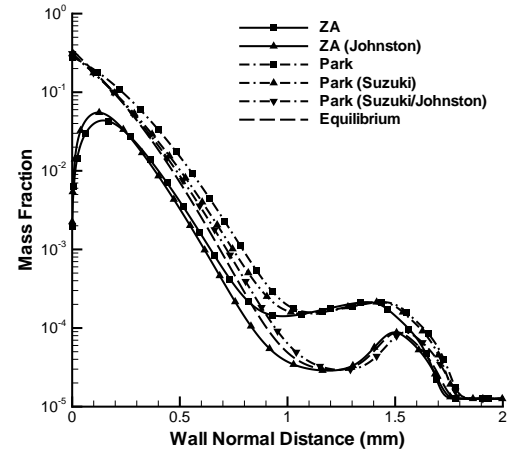
(b) CO
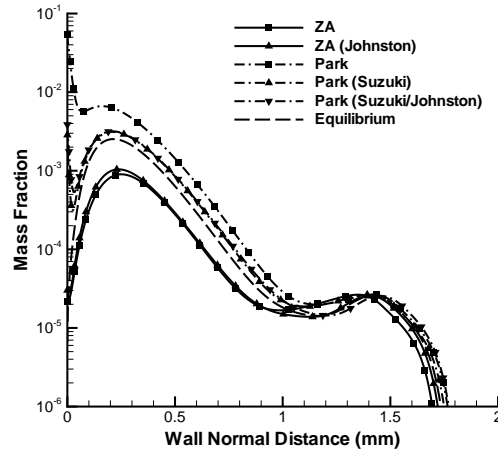
(c) CN

Figure 49. Predicted species mass fractions along the stagnation streamline for $T_w = 2170$ K.
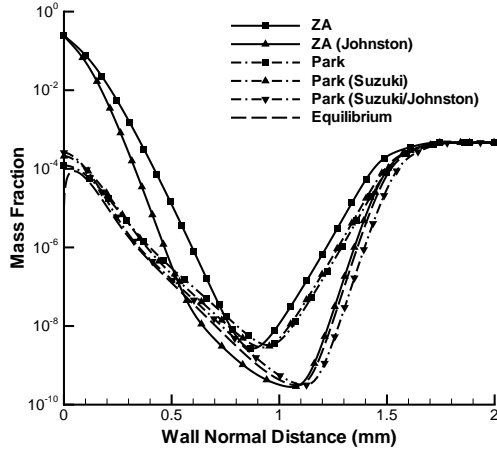
(a) CO_2
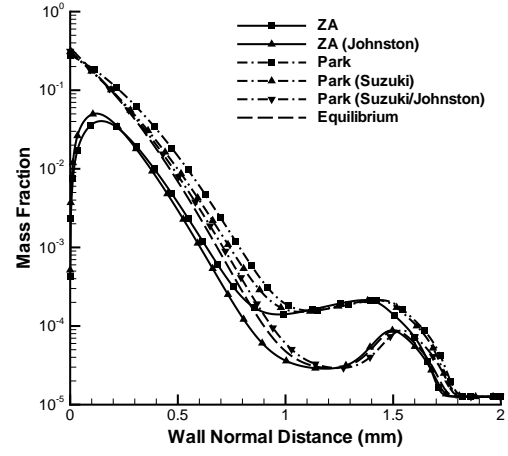
(b) CO
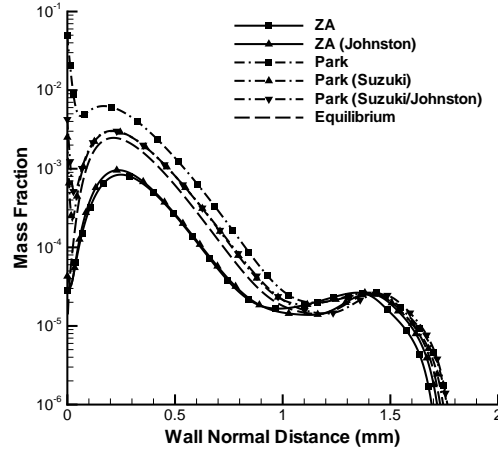
(c) CN

Figure 50. Predicted species mass fractions along the stagnation streamline for $T_w = 1920$ K.
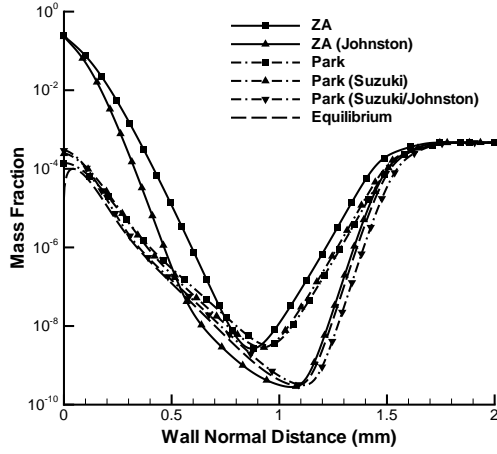
(a) CO_2
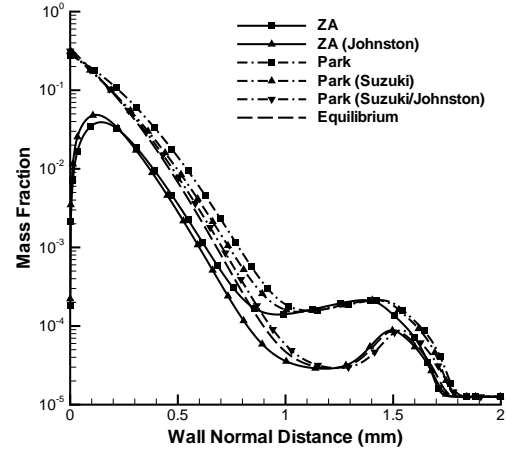
(b) CO
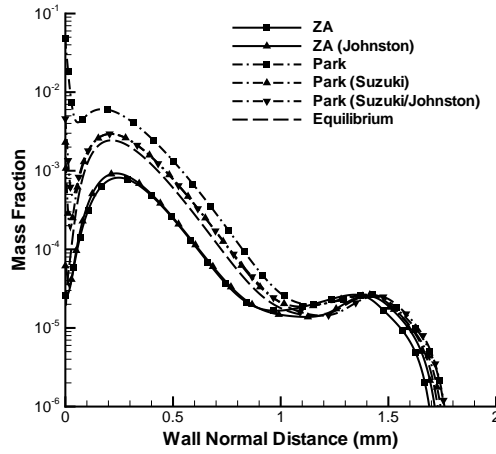
(c) CN

Figure 51. Predicted species mass fractions along the stagnation streamline for $T_w = 1770$ K.

Figures 48-51 plot the species mass fractions for CO_2, CO, and CN as a function of wall normal distance along the stagnation streamline. The modified Park and equilibrium models gave very similar mass fraction profiles at all surface temperatures. Within the considered surface temperature range where oxidation processes dominate, the modified Park and equilibrium models have comparable behavior. Both finite-rate surface models have mechanisms to produce CO but do so through different kinetic processes. The Park model produced CO and predicted it to diffuse away from the surface resulting in a larger mass fraction in the near-wall boundary layer. In comparison, the ZA model predicted CO to recombine at the surface resulting in lower CO boundary layer concentrations. Additionally, the predicted CO_2 mass fractions were substantially different in the near-wall boundary layer region between the finite-rate surface models. The ZA model predicted over three orders of magnitude more CO_2 at the stagnation point compared to the Park model for all wall temperatures. Interestingly, using the Johnston chemistry with the ZA model increased the rate at which CO_2 was destroyed along the stagnation streamline, but it actually increased the concentration of CO near the wall. The increase in gaseous CO concentration is non-intuitive because the Johnston chemistry model has a CO dissociation rate 13 times higher than the Park gas-phase chemistry model rate. Therefore, it would be expected the amount of CO in the boundary layer would decrease using the Johnston chemistry model. However, as noted in Section 3.3.7, the ZA surface reactions are non-linearly coupled to the gas chemistry model, so results displaying linear relationships should not be expected.

Similar CN mass fraction profiles were achieved for all cases at wall normal distances greater than approximately 1 mm, which coincided with the region of thermal nonequilibrium. The CN concentration for the Park model is strongly affected by the amount of CN produced at the wall. Consequently, the Park model predicted the

highest boundary layer CN concentration across the wall temperature range considered. Due to the much lower nitridation rate of the modified Park model, the peak CN concentration in the boundary layer was approximately cut in half compared to the original Park model for each wall temperature. The ZA model, which has no nitridation mechanism, predicted the lowest peak CN concentrations. The amount of CN in the boundary layer was entirely controlled by the gas-phase chemistry model for the ZA results. As the wall temperature was lowered, the peak boundary layer CN concentration predicted by the ZA model was reduced by 18% from $T_w = 2410$ K to 1770 K. Comparing the mass fraction profiles for all cases considered, there appears to be a correlation between the CO and CN boundary layer concentrations. In general, higher CO concentrations led to higher CN concentrations.

5.2.2 Radiation Comparisons.

Good agreement was found for the locations of peak radiation intensity measured in the experiment and the predicted maximum CN mass fraction in the boundary layer. Figure 52 demonstrates this agreement with a series of plots. The predicted CN mass fraction shown in this figure was computed using the ZA model. The spectrometer measured the strongest radiative intensity at the stagnation point to occur approximately between 0.10-0.30 mm from the wall. The spectral radiance was extracted along a line of constant wavelength at 388.4 nm and plotted with the CN mass fraction in Figure 52c. As will be shown below, the SRF has a tendency to broaden and shift the predicted radiance profile closer to the wall which further improves this comparison. There is also good agreement for the shock location, which is approximately located 1.80 mm away from the wall. Note that the predicted local maximum of CN in the boundary layer was also at a similar wall normal distance when computed using the Park and equilibrium models. Hence, all surface ablation models
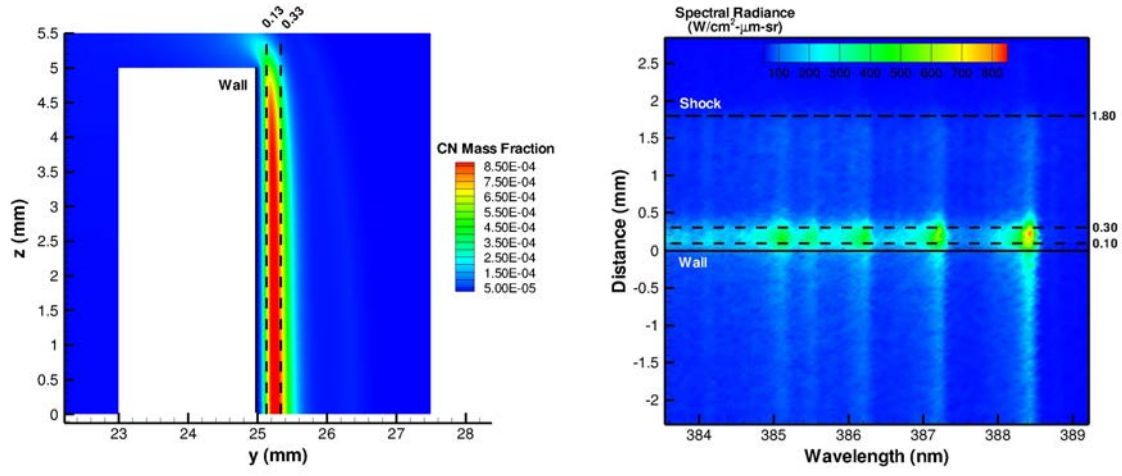
(a) Predicted CN mass fraction.

(b) Experimental spectral radiance.
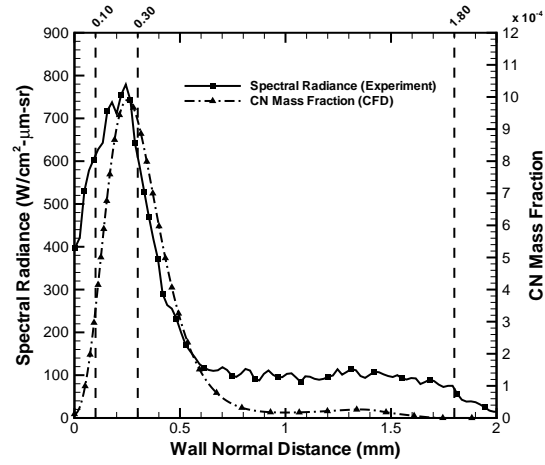
(c) Comparison of peak and shock locations.

Figure 52. Comparison of peak experimental spectral radiance and predicted maximum CN concentration using the ZA model for the $T_w = 2410\,\text{K}$ case.

are consistent with the experiment in this regard, but it is the actual concentration level that will have the most significant impact on the radiation results.

The radiance results as a function of wall normal distance along the stagnation streamline are compared in Figure 53. The X-2 radiance uncertainty shown in this figure varied between 31%-33% as defined by Lewis et al. [57]. Note that the same estimated SRF was applied to each predicted radiance profile calculated by NEQAIR, which broadened and slightly shifted the profiles toward the surface. The result was a much better agreement to the shape and location of the boundary layer peak value compared to the measured radiance profile.

Overall, the numerical simulations demonstrated a better ability to predict radiance values near the surface than in the shock layer. The experimental measurements displayed a more significant amount of CN violet radiation emitted from the shock layer than what the simulations indicated. The reasons for this are currently unknown, but there is likely some source of facility contamination present. It was peculiar that the shock layer CN radiation appeared to increase with surface temperature, and Lewis et al. [57] speculated that this could be due to spallation. The high-speed video from the $T_w = 2410$ K case possibly displayed a small amount of carbon particles ejected from the surface. The theory is that spalled carbon particles entered the inviscid, high temperature shock layer and vaporized allowing carbonaceous gas species, such as CN, to form and radiate. These simulations can not predict the mechanical breakdown of the bulk carbon, nor track spalled particles as they diffuse through the shock layer. Another consideration may be that there are trace amounts of CN in the freestream that emits as soon as it passes through the shock. Possible sources could be from the facility's vacuum pump system or diaphragm materials. More investigation into this phenomenon is required to determine the discrepancy between the experiments and simulations. Therefore, the following comparison discussion will
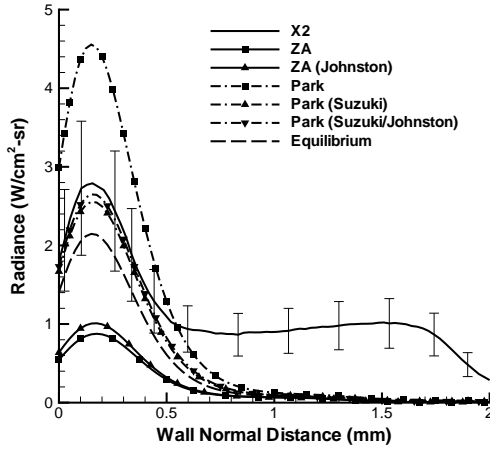
(a) $T_w = 2410\,\mathrm{K}$
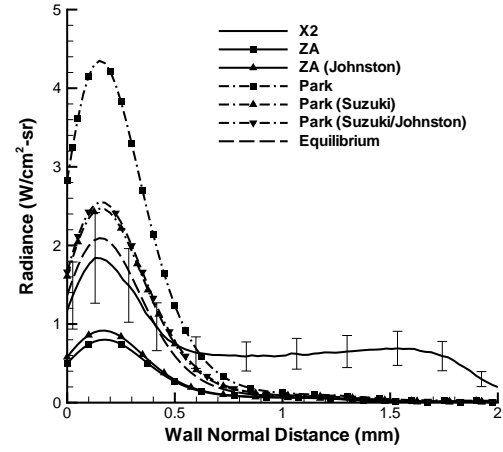
(b) $T_w = 2170\,\mathrm{K}$
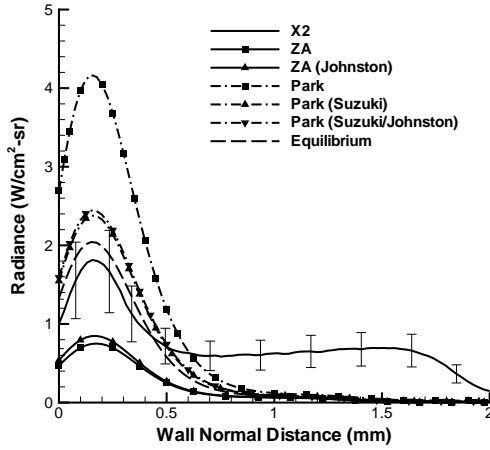
(c) $T_w = 1920\,\mathrm{K}$
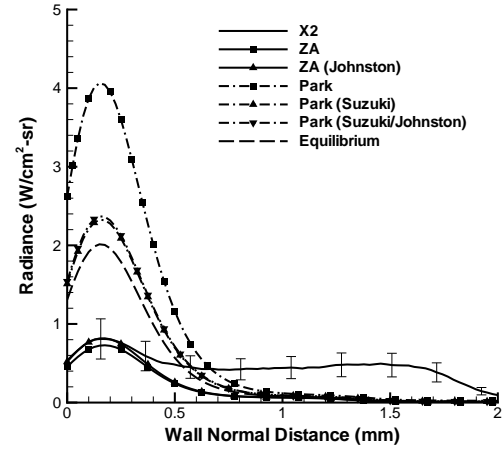
(d) $T_w = 1770\,\mathrm{K}$

Figure 53. Comparison of radiance values as a function of wall normal distance along the stagnation streamline.

focus on the radiance profiles near the model surface.

The following trends observed between the two ablation models indicate that nitridation may be an important surface reaction to consider in these flows. In accordance with the relatively higher CN concentrations in the boundary layer, the Park model predicted radiance values above those measured in the experiment for all considered surface temperatures. However, the conclusion is not that nitridation was an insignificant surface reaction. The modified Park model displayed reasonably good agreement at $T_w = 2410$ K with marginal improvement when combined with the Johnston chemistry model. The ablation of CN into the boundary layer increased the CN mass fraction to concentrations found in the experiment for the $T_w = 2410$ K case. Unfortunately, the comparison got worse for the modified Park model as the wall temperature was lowered, which does lead to the conclusion that nitridation becomes less significant. The ZA model was shown to exhibit the opposite trend and had the best agreement at the lowest wall temperature considered. Although the applied SRF is more or less arbitrary for this X-2 data set, the ZA model with Johnston chemistry had excellent agreement for the near surface radiance profile at $T_w = 1770$ K. The ZA model then began to under predict the radiance values at the higher wall temperatures. Based off these observations, the nitridation reaction appears to be activated above a surface temperature of approximately 1800 K.

The equilibrium result gave the same radiance profile for each surface temperature. Clearly, the radiation emitted from CN was sensitive to a varying surface temperature as measured in the experiment. Therefore, the use of an equilibrium ablation model is not appropriate to simulate these specific flows even though there is the appearance of good agreement at a few of the surface temperatures. At $T_w = 2170$ K, for example, the equilibrium model provided the best prediction compared to the experiment, but it would be presumptuous to conclude that the surface and gas were indeed in chemical

equilibrium.

To quantify these differences, the normalized absolute error with respect to the experimental values was calculated for each predicted result. The error is only shown out to a wall normal distance of 0.4 mm due to the uncertainties in the shock layer. The Park model results are not shown at a wall temperature of 1770 K because its error was around 400%. These error results reinforce the observed trends. At $T_w = 2410$ K, the modified Park model with Johnston chemistry had a maximum error of approximately 8%, while the ZA and original Park models hovered around an error between 60-70%. The ZA and modified Park models both had comparable error estimates with a mean around 50% for wall temperatures of 2170 K and 1920 K. At the lowest wall temperature of 1770 K, the ZA model with the Johnston chemistry had errors of 1-2% that coincided with the location of peak intensity. The modified Park models began to significantly diverge from the experimental results with errors above 180%.

From this analysis, it is concluded that the ZA model is preferred over the original or modified Park model because it is a mechanism-based approach with a physically meaningful methodology. The Park models are too simplistic with highly empirical rate parameters that only include a few of the relevant ablative species for an air-carbon system. The ZA model makes use of gas-kinetic theory and accounts for physical mechanisms such as the flux of atoms impinging on the surface and adsorption processes. Furthermore, many more reaction pathways are defined with the ZA model that includes more of the relevant ablative species. However, parameterizing the ZA model remains an issue because the predicted species mass fluxes were nearly constant between surface temperatures of 1770-2410 K, which contradicted the trends observed in the experiment. Additionally, there may be a deficiency in the baseline ZA model because it does not include any CN surface reactions. The following sections describe
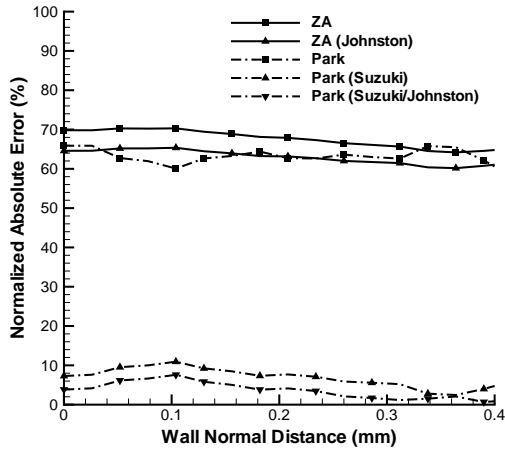
(a) $T_w = 2410\,\text{K}$
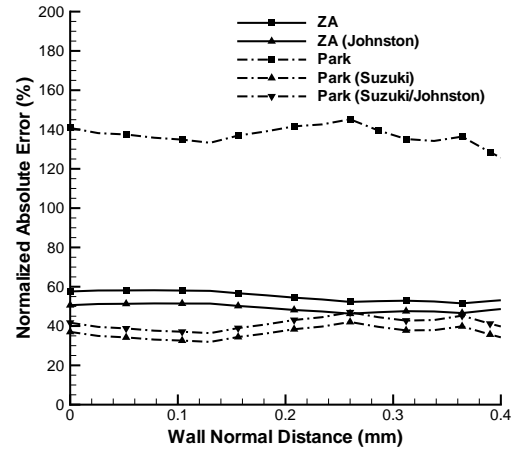
(b) $T_w = 2170\,\text{K}$
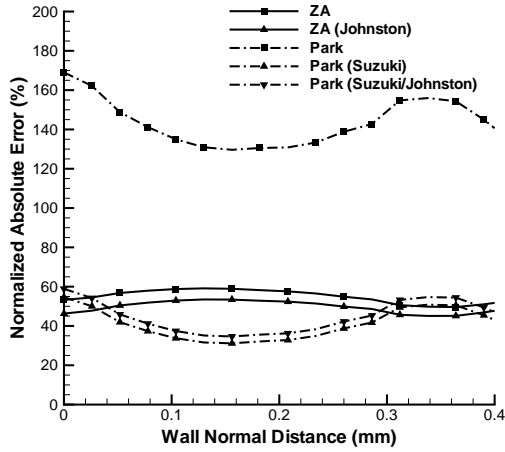
(c) $T_w = 1920\,\text{K}$
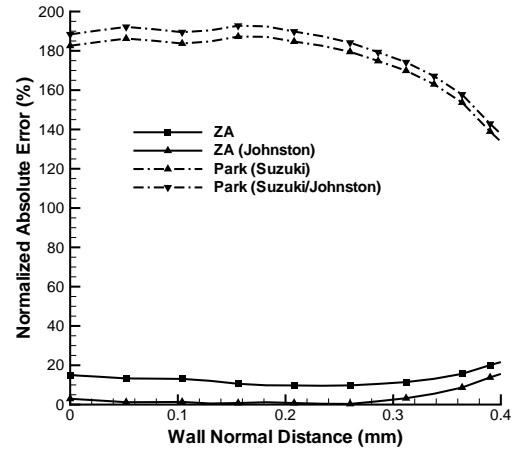
(d) $T_w = 1770\,\text{K}$

Figure 54. Normalized absolute error of predicted radiance values with respect to the experimental results.

how a new model derived from the baseline ZA model is developed to further improve the CN radiance comparisons.

5.3 Screening Design Results

5.3.1 Statistical Correlations.

The ZA model rate coefficients screening design described in Section 3.7 was executed using the 30 km condition from Section 4.1 because that condition was shown to include all three ablation mechanisms of oxidation, nitridation, and sublimation. For a more complete screening design, the direct nitridation reaction was included in the ZA model because it was shown in Section 4.3 that the surface participating nitridation reaction had a negligible effect on the results. The baseline ZA rate coefficient values were shown in Tables 8 and 10. To compute the CN radiative heat fluxes, the NEQAIR code was used again. For the purposes of this screening design, the populations of the excited CN electronic states were found using a Boltzmann distribution. The radiance was calculated by integrating the spectral radiance between the wavelength range of 353-391 nm. The post-shock flow quantities were extracted from the volumetric solution corresponding to a line-of-sight that was normal to the stagnation streamline. Multiple slice extractions were performed along the stagnation streamline that provided radiance predictions as a function of wall normal distance. To obtain a single total CN radiance value, the radiance along the stagnation streamline was integrated from the surface out to a wall normal distance of 0.4 mm.

There were 13 screening design factors that represented each pre-exponential reaction rate coefficient of the ZA model including nitridation. Table 15 shows the screening design matrix and resulting metrics. Again, the quantitative metric was the absolute percent difference of the CN radiance from the baseline case (Run 1). For simplicity, the 13 factor levels were denoted by the symbol $\triangle_i$ with the subscript

Table 15. The Zhluktov and Abe rate coefficient screening design and CN radiance metrics.

Run	$\triangle_1$	$\triangle_2$	$\triangle_3$	$\triangle_4$	$\triangle_5$	$\triangle_6$	$\triangle_7$	$\triangle_8$	$\triangle_9$	$\triangle_{10}$	$\triangle_{11}$	$\triangle_{12}$	$\triangle_{13}$	CN Radiance	Difference
1	1.0	1.0	3.58×10^{13}	1.0	0.90	2.08×10^{9}	0.80	3.58×10^{17}	0.240	0.50	0.0230	1.0	0.360	0.84667	0.0000
2	1.0	1.1	3.58×10^{14}	1.1	0.99	2.08×10^{10}	0.88	3.58×10^{18}	0.264	0.55	0.0253	1.1	0.396	0.85440	0.0091
3	1.0	0.9	3.58×10^{12}	0.9	0.81	2.08×10^{8}	0.72	3.58×10^{16}	0.216	0.45	0.0207	0.9	0.324	0.82614	-0.0242
4	1.1	1.0	3.58×10^{12}	1.1	0.81	2.08×10^{8}	0.88	3.58×10^{18}	0.264	0.55	0.0207	0.9	0.396	0.83630	-0.0122
5	0.9	1.0	3.58×10^{14}	0.9	0.99	2.08×10^{10}	0.72	3.58×10^{16}	0.216	0.45	0.0253	1.1	0.324	0.85355	0.0081
6	1.1	0.9	3.58×10^{13}	0.9	0.99	2.08×10^{8}	0.72	3.58×10^{18}	0.264	0.55	0.0253	0.9	0.324	0.83324	-0.0159
7	0.9	1.1	3.58×10^{13}	1.1	0.81	2.08×10^{10}	0.88	3.58×10^{16}	0.216	0.45	0.0207	1.1	0.396	0.85495	0.0098
8	1.1	1.1	3.58×10^{12}	1.0	0.81	2.08×10^{10}	0.72	3.58×10^{16}	0.264	0.55	0.0253	1.1	0.324	0.85013	0.0041
9	0.9	0.9	3.58×10^{14}	1.0	0.99	2.08×10^{8}	0.88	3.58×10^{18}	0.216	0.45	0.0207	0.9	0.396	0.84084	-0.0069
10	1.1	0.9	3.58×10^{14}	0.9	0.90	2.08×10^{8}	0.88	3.58×10^{16}	0.216	0.55	0.0253	1.1	0.396	0.84017	-0.0077
11	0.9	1.1	3.58×10^{12}	1.1	0.90	2.08×10^{10}	0.72	3.58×10^{18}	0.264	0.45	0.0207	0.9	0.324	0.84595	-0.0009
12	1.1	0.9	3.58×10^{12}	1.1	0.81	2.08×10^{9}	0.72	3.58×10^{18}	0.216	0.45	0.0253	1.1	0.396	0.85367	0.0083
13	0.9	1.1	3.58×10^{14}	0.9	0.99	2.08×10^{9}	0.88	3.58×10^{16}	0.264	0.55	0.0207	0.9	0.324	0.84037	-0.0074
14	1.1	1.1	3.58×10^{12}	0.9	0.99	2.08×10^{8}	0.80	3.58×10^{16}	0.264	0.45	0.0207	1.1	0.396	0.82980	-0.0199
15	0.9	0.9	3.58×10^{14}	1.1	0.81	2.08×10^{10}	0.80	3.58×10^{18}	0.216	0.55	0.0253	0.9	0.324	0.85431	0.0090
16	1.1	1.1	3.58×10^{14}	0.9	0.81	2.08×10^{10}	0.72	3.58×10^{17}	0.216	0.55	0.0207	0.9	0.396	0.85592	0.0109
17	0.9	0.9	3.58×10^{12}	1.1	0.99	2.08×10^{8}	0.88	3.58×10^{17}	0.264	0.45	0.0253	1.1	0.324	0.82584	-0.0246
18	1.1	1.1	3.58×10^{14}	1.1	0.81	2.08×10^{8}	0.88	3.58×10^{16}	0.240	0.45	0.0253	0.9	0.324	0.82702	-0.0232
19	0.9	0.9	3.58×10^{12}	0.9	0.99	2.08×10^{8}	0.72	3.58×10^{18}	0.240	0.55	0.0207	1.1	0.396	0.85303	0.0075
20	1.1	1.1	3.58×10^{14}	1.1	0.99	2.08×10^{8}	0.72	3.58×10^{18}	0.216	0.50	0.0207	1.1	0.324	0.83419	-0.0147
21	0.9	0.9	3.58×10^{12}	0.9	0.81	2.08×10^{10}	0.88	3.58×10^{16}	0.264	0.50	0.0253	0.9	0.396	0.85400	0.0087
22	1.1	0.9	3.58×10^{14}	1.1	0.99	2.08×10^{10}	0.72	3.58×10^{16}	0.264	0.45	0.0230	0.9	0.396	0.85227	0.0066
23	0.9	1.1	3.58×10^{12}	0.9	0.81	2.08×10^{8}	0.88	3.58×10^{18}	0.216	0.55	0.0230	1.1	0.324	0.83626	-0.0123
24	1.1	0.9	3.58×10^{12}	1.1	0.99	2.08×10^{10}	0.88	3.58×10^{16}	0.216	0.55	0.0207	1.0	0.324	0.85130	0.0055
25	0.9	1.1	3.58×10^{14}	0.9	0.81	2.08×10^{8}	0.72	3.58×10^{18}	0.264	0.45	0.0253	1.0	0.396	0.83912	-0.0089
26	1.1	1.1	3.58×10^{12}	0.9	0.99	2.08×10^{10}	0.88	3.58×10^{18}	0.216	0.45	0.0253	0.9	0.360	0.85622	0.0113
27	0.9	0.9	3.58×10^{14}	1.1	0.81	2.08×10^{8}	0.72	3.58×10^{16}	0.264	0.55	0.0207	1.1	0.360	0.82612	-0.0243
28	1.1	0.9	3.58×10^{14}	0.9	0.81	2.08×10^{10}	0.88	3.58×10^{18}	0.264	0.45	0.0207	1.1	0.324	0.84619	-0.0006
29	0.9	1.1	3.58×10^{12}	1.1	0.99	2.08×10^{8}	0.72	3.58×10^{16}	0.216	0.55	0.0253	0.9	0.396	0.84026	-0.0076

Table 16. Correlations for Zhluktov and Abe rate coefficient screening. Significant correlations are highlighted.

	$\triangle_1$	$\triangle_2$	$\triangle_3$	$\triangle_4$	$\triangle_5$	$\triangle_6$	$\triangle_7$	$\triangle_8$	$\triangle_9$	$\triangle_{10}$	$\triangle_{11}$	$\triangle_{12}$	$\triangle_{13}$
CN Radiance	0.0065	0.0267	0.0060	-0.0265	0.0185	0.8222	0.0010	0.1348	-0.2285	0.0722	0.1457	-0.0162	0.2863
Difference	0.0070	0.0269	0.0052	-0.0266	0.0181	0.8219	0.0015	0.1344	-0.2287	0.0719	0.1453	-0.0163	0.2865

i referring to the reaction number. The metrics were evaluated in a JMP® [104] multivariate analysis report. The report provided independent correlation values for each factor and response, which are shown in Table 16. The pairwise correlations gave an estimate of factor significance. Lehman et al. [55] proposed that correlations between 0.2 and 0.5 are weakly significant, correlations between 0.5 and 0.8 are moderately significant, and correlations greater than 0.8 are strongly significant. These correlations are also applicable for negative values where they would be defined as an inverse relationship.

The only statistically significant factor that had an impact on the CN radiance was $\triangle_6$, the Arrhenius coefficient for the oxidation reaction $O(s) + C(b) \leftrightarrow CO + (s)$.

The nitridation efficiency and atomic carbon condensation efficiency, factors $\triangle_{13}$ and $\triangle_9$, were the only other parameters that could possibly be identified as somewhat significant. However, the correlations indicate that any changes to these coefficients would only have minor impacts. Note that the atomic carbon condensation efficiency is negatively correlated meaning a decrease in efficiency would result in an increase in CN radiance values. Furthermore, these results show that more CO needs to be produced at the surface if the goal is to increase CN radiance values.

5.3.2 Surface Reaction Rate Modifications.

Based on the rate coefficient screening results, rate modifications should consider the surface reactions that had the most influence on increasing CN radiance predictions. The initial set of modifications applied to the ZA model are:

- Increase the Arrhenius coefficient by at least one order of magnitude for the oxidation reaction $O(s) + C(b) \leftrightarrow CO + (s)$.

- Increase the ER nitridation efficiency by no more than 10% because there is still uncertainty about extrapolating the derived rate parameters to higher surface temperatures.

- Decrease the atomic carbon condensation efficiency by 10%.

The influence of CO_2 should also be considered because it could indirectly effect CN concentrations. The stagnation point reaction fluxes from Run 1 of the screening design (baseline case) are shown in Table 17 to highlight preferred reaction directions. The surface temperature was approximately 3600 K. Under these conditions, reaction 5 produces CO_2 because it proceeds in the backward direction. Additionally, Figures 44-47 showed that CO_2 was the dominant ablative species for each surface temperature considered. Therefore, a modification to the surface reaction

140

Table 17. Stagnation point reaction fluxes from Run 1 of the Zhluktov and Abe rate coefficient screening design ($T_w \approx 3600$ K).

	Reaction	r (kmol m^{-2} s^{-1})
(1)	$O + (s) \leftrightarrow O(s)$	4.53×10^{-3}
(2)	$N + (s) \leftrightarrow N(s)$	1.16×10^{-4}
(3)	$2O(s) \leftrightarrow O_2 + 2(s)$	2.16×10^{-8}
(4)	$O_2 + (s) \leftrightarrow O + O(s)$	-2.17×10^{-6}
(5)	$CO_2 + (s) \leftrightarrow CO + O(s)$	-3.47×10^{-4}
(6)	$O(s) + C(b) \leftrightarrow CO + (s)$	4.12×10^{-3}
(7)	$O + O(s) + C(b) \leftrightarrow CO_2 + (s)$	4.29×10^{-6}
(8)	$2O(s) + C(b) \leftrightarrow CO_2 + 2(s)$	2.59×10^{-5}
(9)	$C + (s) \leftrightarrow (s) + C(b)$	2.10×10^{-2}
(10)	$C_2 + 2(s) \leftrightarrow 2(s) + 2C(b)$	-1.77×10^{-3}
(11)	$C_3 + 3(s) \leftrightarrow 3(s) + 3C(b)$	-1.42×10^{-3}
(12)	$N_2 + (s) \leftrightarrow N + N(s)$	-1.16×10^{-4}
(13)	$N + (s) + C(b) \leftrightarrow CN + (s)$	2.76×10^{-2}

$CO_2 + (s) \leftrightarrow CO + O(s)$ is recommended because it appears to have a tendency to generate CO_2 rather than CO. The screening design results showed that the forward rate ER efficiency for this reaction had no correlation to predicted CN radiance values. However, this reaction prefers to proceed in the reverse direction at a surface temperature of approximately 3600 K, so a $\pm 10\%$ forward rate perturbation is not going to change the reaction direction. Hence, the statistical insignificance of this reaction makes sense because any slight increase or decrease in CO_2 mass flux is not going to alter CN levels.

For the following reasons, and without additional detailed reaction rate data, it is proposed to remove the $CO_2 + (s) \leftrightarrow CO + O(s)$ reaction from the ZA model in hopes of increasing CN radiance values. A review of the ZA model revealed that the incorporated oxidation reactions were influenced by the work found in References [123, 111, 85, 50, 79]. References [50] and [79] only describe oxygen and nitrogen surface recombination processes and have no reactions to produce CO or CO_2. References [123, 111, 85] discuss several possible mechanisms for CO and CO_2
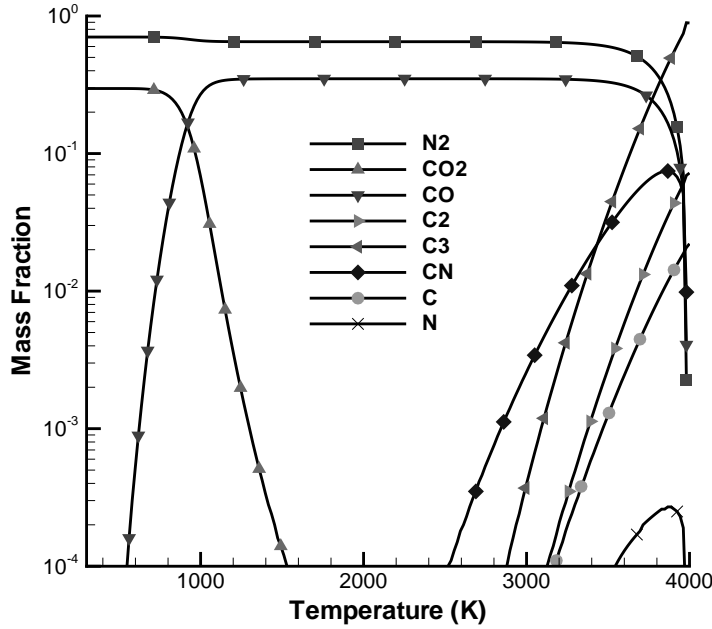
Figure 55. Species mass fractions of an equilibrium carbon-air mixture as a function of temperature at 1 atm pressure.

production, but show it as only possible through reactions of adsorbed O or O_2 with the bulk carbon. In fact, Zhluktov and Abe [136] identify the work of Walker et al. [123] as the preferred mechanism for CO_2 formation, of which the reaction $2O(s) + C(b) \leftrightarrow CO_2 + 2(s)$ is primarily responsible. Walker et al. [123] does list the $CO + O(s) \leftrightarrow CO_2 + (s)$ reaction as a possible CO_2 mechanism but concluded that it was not likely to occur based on their experiments. None of the other references list any possible path similar to this reaction. Expanding the review to other experimental work analyzing carbon oxidation discovered that CO was consistently found as the principal reaction product across a range of surface pressures and temperatures [78, 124, 83, 82, 58, 100, 77]. Additionally, MacLean [63] developed a tool to compute the composition of an equilibrium saturated air-carbon mixture at selected pressures and temperatures. The species mass fractions of an equilibrium air-carbon mixture as a function of temperature at 1 atm pressure is plotted in Figure 55, which was the

stagnation pressure in the X-2 experiments shown in Figure 42. Note that the gas is a simple mixture of primarily N_2 and CO within an approximate temperature range of 1500-2500 K.

The proposed modifications were implemented into the ZA model and applied to the 30 km case. A comparison of the species mass fluxes with the Park and modified ZA models is shown in Figure 56. The C_2 and C_3 mass flux profiles were unchanged because none of the proposed modifications affected those sublimation reactions. Additionally, the C and CN mass fluxes remained relatively the same. The major improvement with this proposed model compared to the other model variations is that CO is now the main oxidation product instead of CO_2 over a majority of the surface. However, despite increased CO surface production, the calculated total CN radiance was not that much higher compared to the baseline case with only a 0.001 difference. The small difference is likely related to the gas-phase chemistry model, which has a strong influence on species production rates in the boundary layer. The Johnston gas chemistry model used in the X-2 simulations increases the CO dissociation rate by a factor of 13 compared to the model used for the screening design study. Combining these ZA model modifications with the Johnston gas chemistry model may now produce drastically different results.

5.4   ZA Model Modifications Applied to X-2 Experiments

The four wall temperature cases from the first X-2 campaign were rerun with the proposed modifications described in the previous section. Figures 57 and 58 plot the predicted species surface mass fluxes and stagnation streamline mass fractions at $T_w = 2410$ K. The ZA model with nitridation now has a CN mass flux that is approximately three times larger than the modified Park model. However, CN dissociates immediately away from the surface, and there is only a slight increase in
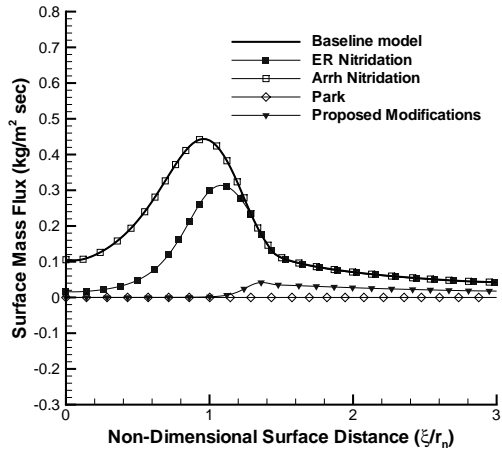
(a) CO_2
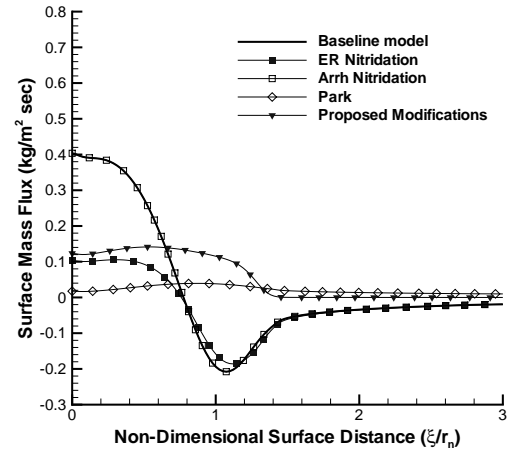
(b) CO
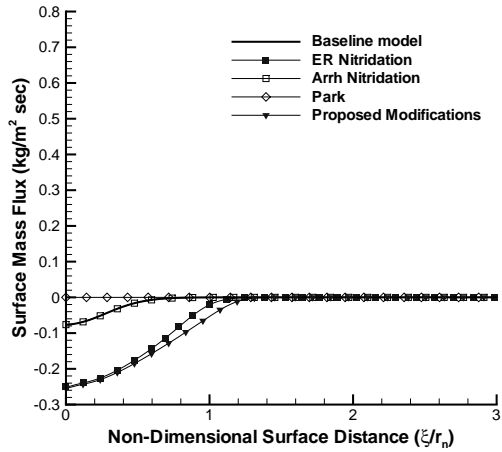
(c) C
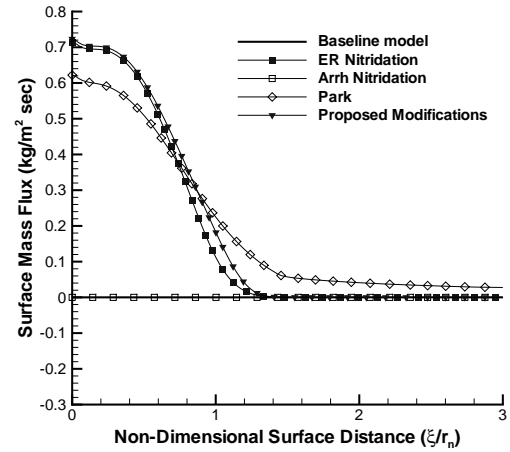
(d) CN

Figure 56. Species surface mass fluxes as a function of normalized distance from stagnation point at 30 km conditions with proposed ZA model modifications.

144

the peak boundary layer concentration compared to the ZA model without nitridation as shown in Figure 58. The inclusion of a nitridation reaction does not significantly alter the oxidation reactions, and CO_2 is still the main product.

There was a significant change when all of the proposed nitridation and oxidation reaction modifications were implemented. The main oxidation product becomes CO, and very little CO_2 was produced at the surface. The CO mass fractions at the surface were an order of magnitude higher and were similar to the modified Park model predictions. It was previously noted that higher CO concentrations led to higher CN concentrations, which is again reflected in Figure 58. The peak CN boundary layer concentration was twice as high with the ZA model with all proposed modifications compared to the baseline ZA model. The increase in CN levels is likely due to a combination of these three gas-phase reactions:

$$CO + M \;\rightleftharpoons\; C + O + M$$
$$N_2 + C \;\rightleftharpoons\; CN + N$$
$$CO + N \;\rightleftharpoons\; CN + O$$
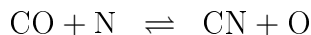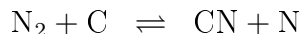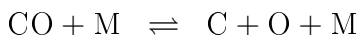
The Johnston [46] gas chemistry model dissociates CO at a much higher rate than the traditional Park [96] model, which will make C more readily available to react with N_2. Any leftover CO can react with N to also form CN.

The ZA model augmented with direct nitridation only provided a minimal improvement in radiance predictions at the higher considered surface temperatures. Updated CN radiance predictions are presented in Figure 59 with the implemented direct nitridation reaction and the rate modifications proposed in the previous section. Note that all surface model predictions shown used the Johnston gas chemistry model. At surface temperatures of 1920 K and 1770 K, the ZA model with direct
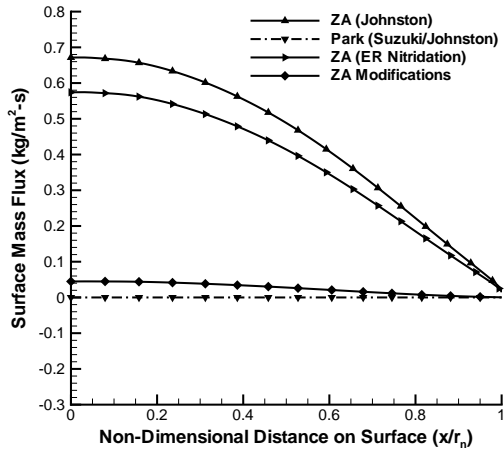
(a) CO_2
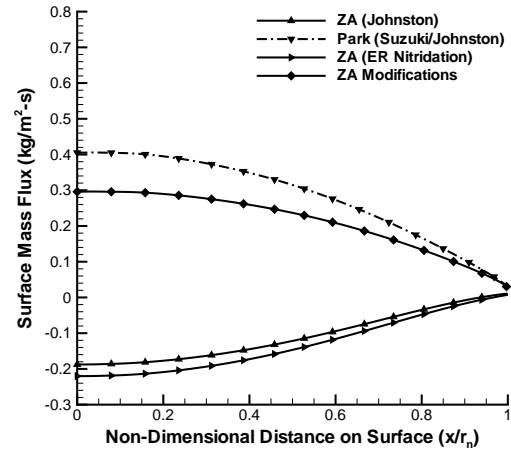
(b) CO
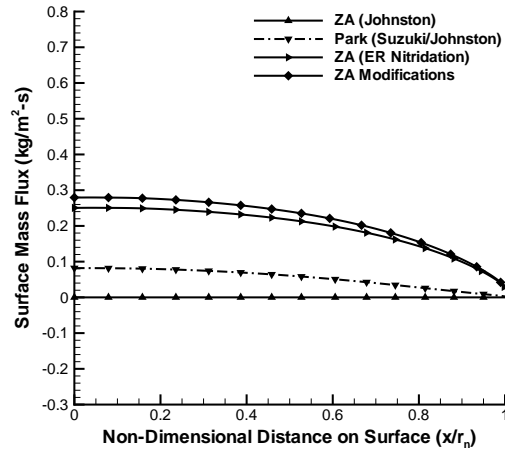
(c) CN

Figure 57. Predicted species surface mass fluxes as a function of normalized distance from the stagnation point for the $T_w = 2410$ K case.
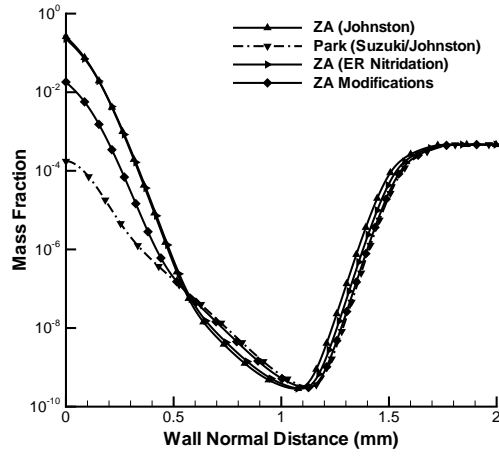
(a) CO_2
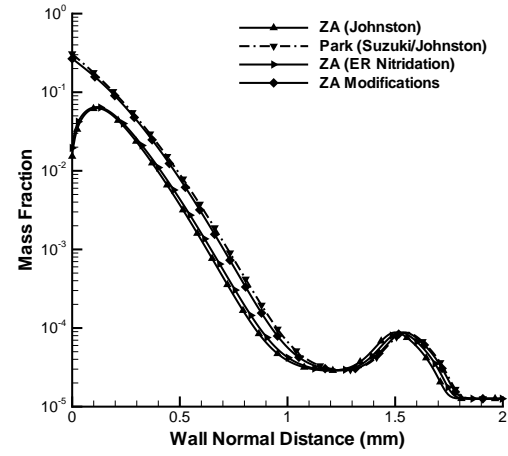
(b) CO
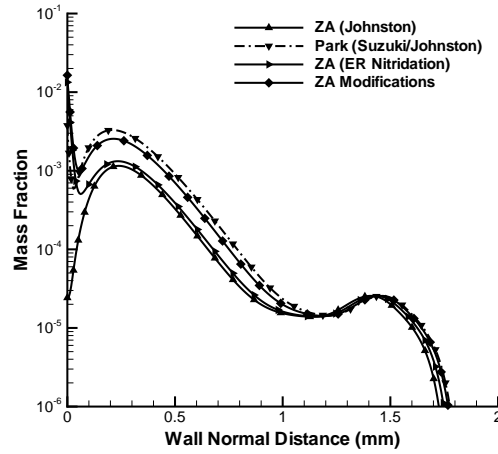
(c) CN

Figure 58. Predicted species mass fractions along the stagnation streamline for $T_w = 2410$ K case.
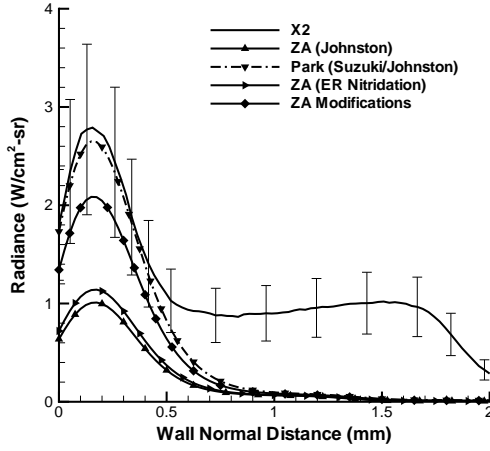
(a) $T_w = 2410\,\mathrm{K}$
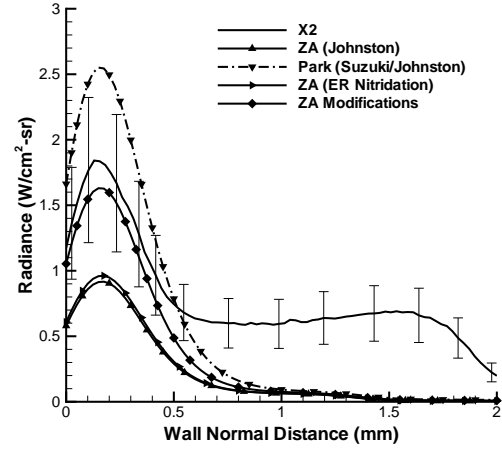
(b) $T_w = 2170\,\mathrm{K}$
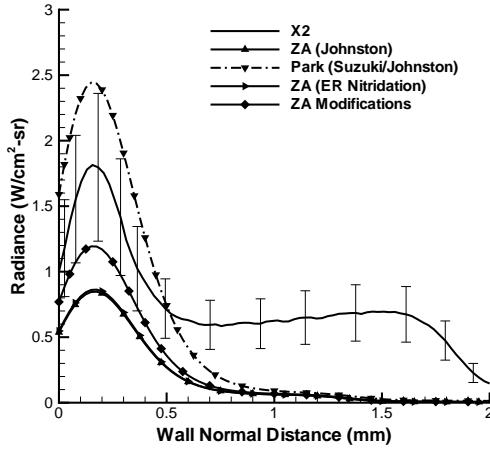
(c) $T_w = 1920\,\mathrm{K}$
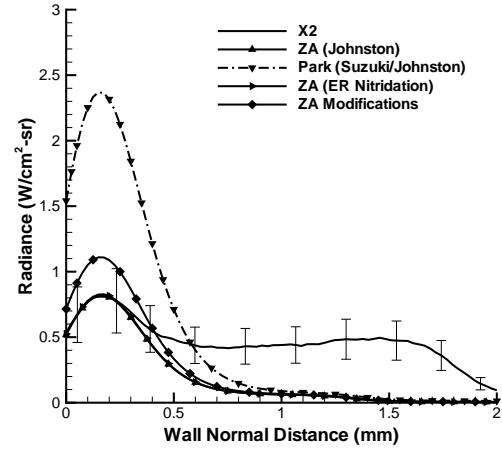
(d) $T_w = 1770\,\mathrm{K}$

Figure 59. Updated comparison of CN radiance values as a function of wall normal distance along the stagnation streamline for lower four wall temperature cases from the X-2 experiments. The ZA model has been modified to include direct nitridation and other rate coefficient adjustments.

nitridation gave the same result as the baseline ZA model, which is consistent with the observations from Section 4.3 that nitridation was only active above surface temperatures of about 2000 K. The ZA model with all proposed modifications improved the predictions for all surface temperatures except at $T_w = 1770$ K. Although not shown, the primary oxidation product again becomes CO_2 for the modified ZA model at the lowest surface temperatures. Better agreement is obtained with the baseline ZA model at $T_w = 1770$ K and is correlated to the fact that CO recombines at the surface causing lower CN mass fractions than those predicted by the modified ZA model.

The CN radiance error estimates at a wall normal distance of 0.15 mm are compared in Table 18. The ZA model with nitridation only provided a 5% improvement compared to the baseline model at $T_w = 2410$ K, whereas with all proposed modifications, the prediction was improved by 39%. It is also important to point out that the radiance predictions for the ZA model with all proposed modifications now fall within experimental uncertainty estimates for all surface temperatures considered.

Furthermore, the radiance predictions with all proposed modifications now display a sensitivity to a varying surface temperature as was observed in the experimental measurements. It was originally postulated that a nitridation mechanism would produce this sensitivity to surface temperature, but it has now been shown to be due to oxidation mechanisms. Specifically, controlling the ratio of CO to CO_2 produced at the surface has caused the improved predictions and surface temperature sensitivity. Increasing the amount of CO in the boundary layer for the higher surface temperature cases has increased the CN concentrations and thereby increased the CN radiance predictions. Note that the choice of gas-phase chemistry model is also going to heavily influence the species produced at the surface and within the gas itself.

Table 18. CN radiance error estimates at a wall normal distance of 0.15 mm.

Surface Model	Absolute Error
$T_w = 2410$ K	
ZA (Johnston)	64%
ZA (ER Nitridation)	59%
ZA Modifications	25%
$T_w = 2170$ K	
ZA (Johnston)	50%
ZA (ER Nitridation)	48%
ZA Modifications	11%
$T_w = 1920$ K	
ZA (Johnston)	53%
ZA (ER Nitridation)	52%
ZA Modifications	34%
$T_w = 1770$ K	
ZA (Johnston)	1%
ZA (ER Nitridation)	2%
ZA Modifications	37%

5.5   Heuristic Modeling Approach

Instead of recommending to remove a reaction from the original ZA model, an investigation was performed following a heuristic approach that attempted to synthesize the oxidation rates to more closely match the X-2 experimental results. Figure 59 illustrated that the baseline ZA model, which also included a nitridation mechanism, had excellent agreement with the experiment at the lowest wall temperature of 1770 K. The three higher wall temperatures all needed more CO to be produced at the surface, which was adequately supplied with a modified ZA model that removed the $CO_2 + (s) \leftrightarrow CO + O(s)$ reaction. The goal of the investigation was to take advantage of this surface reaction by controlling its efficiency at different temperatures.

The study was executed using the 30 km condition again from Section 4.1 because there was a portion of the surface on the sphere-cone geometry that passed through the temperature range considered in the X-2 experiments. The surface pressures

over this surface section were also around 1 atm. The equilibrium constant for the $CO_2 + (s) \leftrightarrow CO + O(s)$ reaction was less than one within the temperature range of 1770-2410 K, so from a pure kinetic standpoint, this reaction prefers to proceed in the backwards direction as similarly noted in Table 17. The forward rate was expressed as an ER reaction type with parameters $\gamma_{er} = 0.9$, $\beta = 0$, and $E = 0$. It is unclear why Zhluktov and Abe [136] had originally defined the reaction in this manner because other work has defined it in its preferred direction of $CO+O(s) \leftrightarrow CO_2+(s)$ [119, 123]. Hence for the purposes of this study, the CO-CO$_2$ oxidation reaction is recast as $CO + O(s) \leftrightarrow CO_2 + (s)$ defined with similar ER rate parameters but allowing for adjustment of the reaction efficiency, γ_{er}. The surface equilibrium constant expression now changes to:

$$K_5 = \frac{X_{CO_2}}{X_{CO}X_O} \frac{1}{K_1} \tag{125}$$

where the gas-phase equilibrium constant for $CO + O \rightarrow CO_2$ was re-computed using the CEA database. The corresponding surface species production rate and species mass balance equations were updated to reflect the change in reaction direction.

The only other surface reaction that produces CO is $O(s) + C(b) \leftrightarrow CO + (s)$, which is defined with an Arrhenius rate expression. The pre-exponential Arrhenius coefficient for this reaction was also adjusted as part of this study. Lastly, the two additional rate modifications proposed in Section 5.3, which were the increase in nitridation efficiency and decrease in carbon condensation efficiency, were also retained.

The results of the study are presented in Figure 60 where the predicted CO surface mass flux is compared to the baseline ZA model with nitridation, the proposed ZA model from Section 5.3, and the heuristically-determined model. The temperature range considered in the X-2 experiments is denoted by the solid vertical bars. The new model now exhibits the desired behavior of CO production at high surface
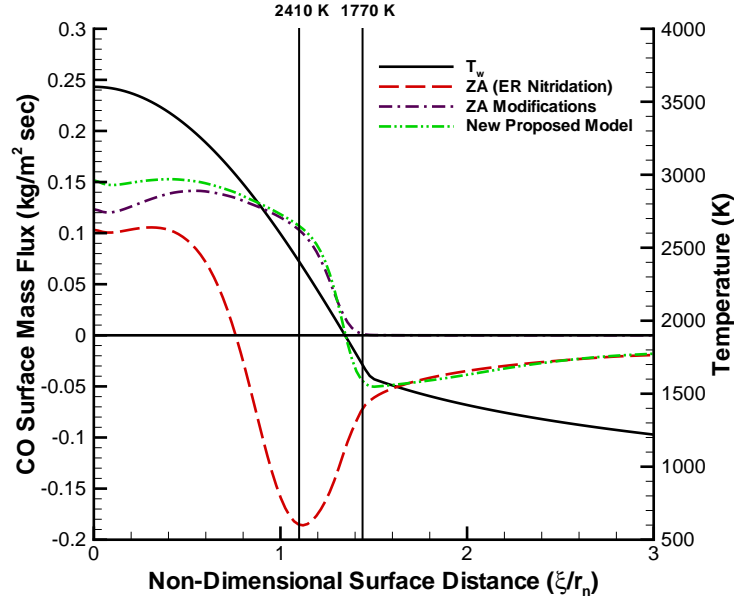
Figure 60. Comparison of the CO surface mass flux computed by different ZA model modifications for the 30 km re-entry condition.

temperatures and CO destruction at low surface temperatures. Furthermore, the behavior of the baseline ZA model is recovered at surface temperatures below 1770 K. The new model with all proposed modifications is presented in Table 19.

The four wall temperature cases from the first X-2 campaign were again rerun with this new model to determine if the CN radiance comparisons were further improved. A comparison of the CO_2 and CO species surface mass fluxes is provided in Figures 61-64 using modified forms of the ZA model and the new proposed model. Clearly, the new model has significantly altered the dominant oxidation processes at the higher surface temperatures. Production of CO_2 has become negligible at the two higher surface temperatures and begins to increase in appreciable quantities at the two lower surface temperatures. The CO oxidation mechanism has completely reversed at the higher surface temperatures. The baseline model has CO recombining at the surface, whereas the new model has CO as the primary ablative product. As the temperature drops below 2000 K, the new model predicts CO production to reduce and eventually

Table 19. New proposed gas-surface chemistry model.

Reaction	Type	S_0 / γ_{er} / A	β	E (kJ mol^{-1})
1.) $O + (s) \leftrightarrow O(s)$	Ads	1	0	0
2.) $N + (s) \leftrightarrow N(s)$	Ads	1	0	0
3.) $2O(s) \leftrightarrow O_2 + 2(s)$	Arrh	3.58×10^{13}	1	256.07
4.) $O_2 + (s) \leftrightarrow O + O(s)$	ER	1	0	118.06
5.) $CO + O(s) \leftrightarrow CO_2 + (s)$	ER	1	0	0
6.) $O(s) + C(b) \leftrightarrow CO + (s)$	Arrh	4.0×10^{12}	1	332.56
7.) $O + O(s) + C(b) \leftrightarrow CO_2 + (s)$	ER	0.8	0	16.63
8.) $2O(s) + C(b) \leftrightarrow CO_2 + 2(s)$	Arrh	3.58×10^{17}	0	332.56
9.) $C + (s) \leftrightarrow (s) + C(b)$	ER	0.216	0	0
10.) $C_2 + 2(s) \leftrightarrow 2(s) + 2C(b)$	ER	0.5	0	0
11.) $C_3 + 3(s) \leftrightarrow 3(s) + 3C(b)$	ER	0.023	0	0
12.) $N_2 + (s) \leftrightarrow N + N(s)$	ER	1	0	636.85
13.) $N + (s) + C(b) \leftrightarrow CN + (s)$	ER	0.396	0	36.86
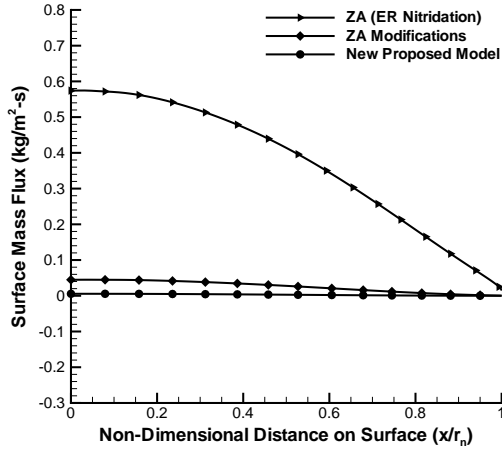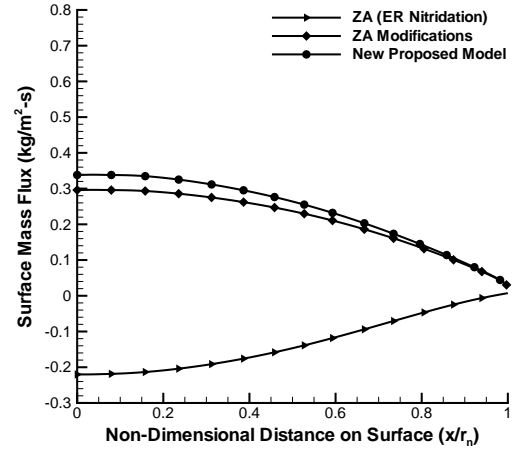
(a) CO_2 (b) CO

Figure 61. Predicted CO and CO_2 surface mass fluxes as a function of normalized distance from the stagnation point for $T_w = 2410$ K using modified ZA models.
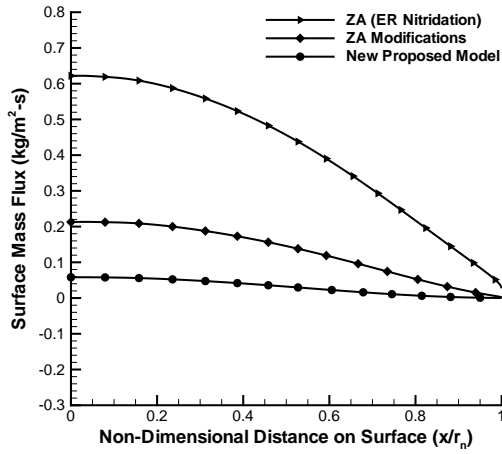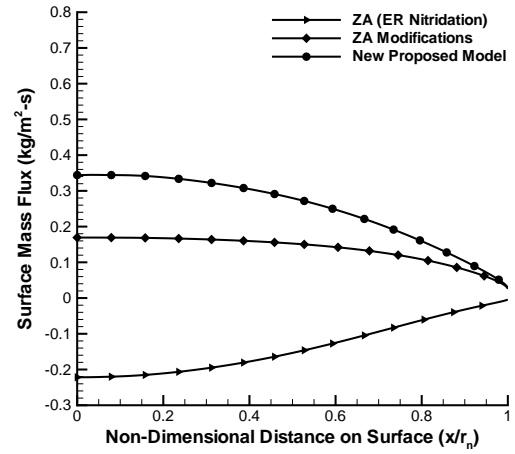
(a) CO_2 (b) CO

Figure 62. Predicted CO and CO_2 surface mass fluxes as a function of normalized distance from the stagnation point for $T_w = 2170$ K using modified ZA models.
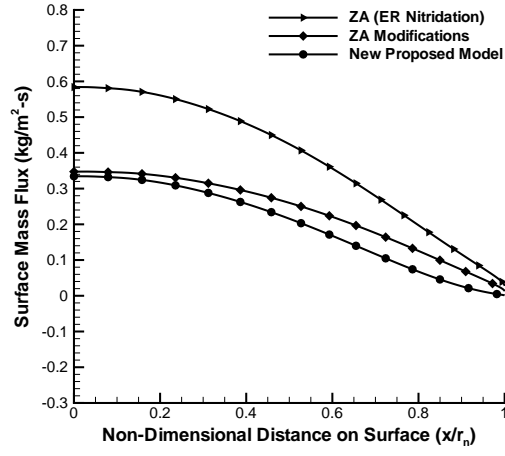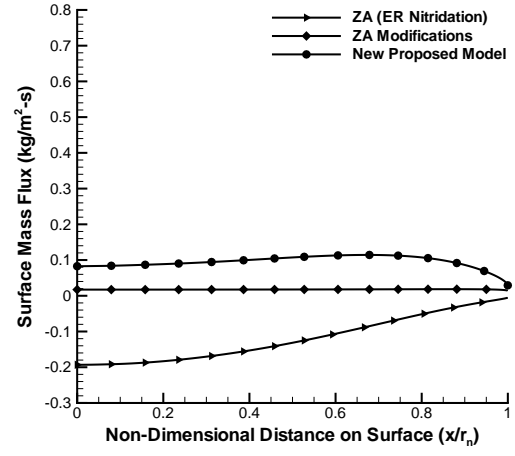
(a) CO_2 (b) CO

Figure 63. Predicted CO and CO_2 surface mass fluxes as a function of normalized distance from the stagnation point for $T_w = 1920$ **K using modified ZA models.**
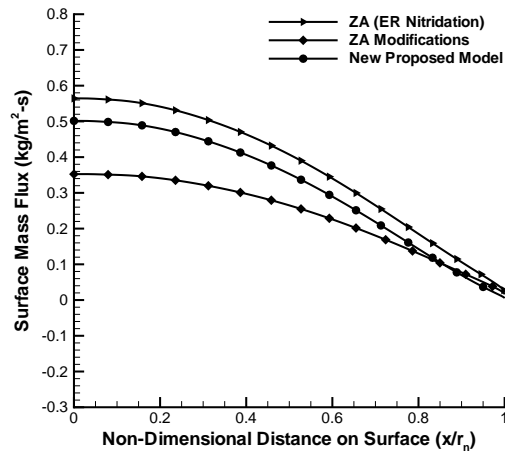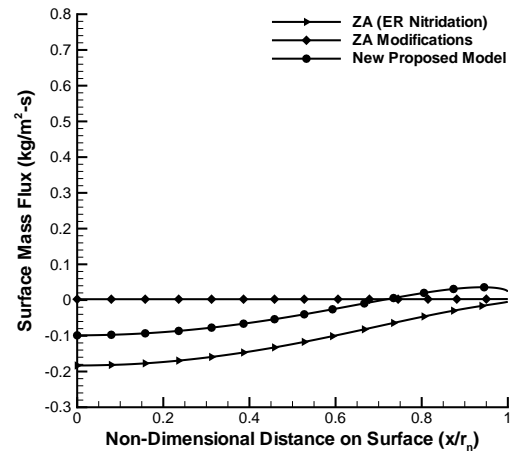
(a) CO_2 (b) CO

Figure 64. Predicted CO and CO_2 surface mass fluxes as a function of normalized distance from the stagnation point for $T_w = 1770$ **K using modified ZA models.**

has CO reacting at the surface similar to the behavior predicted by the baseline model. The solution computed with the new ablation model has met the desired objectives of this investigation by displaying the appropriate oxidation processes that should improve the radiation comparisons.

The CN radiances computed with the new ablation model are compared against the prior considered ZA models in Figure 65. The new ablation model has the overall best agreement with the experiment at each considered surface temperature. The agreement is not perfect, but by appropriately controlling the oxidation ratio of CO to CO_2, the ablation predictions are trending in the right direction. The CN radiance error estimates at a wall normal distance of 0.15 mm for the new model now fall within a range of 7-25% to the experiments as shown in Table 20. The error range for the baseline ZA model was 1-64%, so the new model has significantly reduced the error probability. The new model represents a substantial improvement over the baseline ZA model and should be considered one of the most advanced finite-rate models for further quantification.

5.6   Second Campaign Results

The measured radiance values displayed a non-monotonic behavior as the surface temperatures were increased for the second campaign. As mentioned in Chapter II, initial UV spectrometer measurements imaging a broader spectral range failed to measure any signal from the C_3 Swings and C_2 Swan bands. Therefore, the experimental results and numerical comparisons are focused on the CN violet band. The measured radiance values from the previous four lower surface temperature cases and the four higher surface temperature cases are shown in Figure 66. The peak radiance consistently occurs in the near-wall boundary layer, but the peak value drops significantly going from a surface temperature of 2410 K to 2610 K. In fact, the four higher surface

156
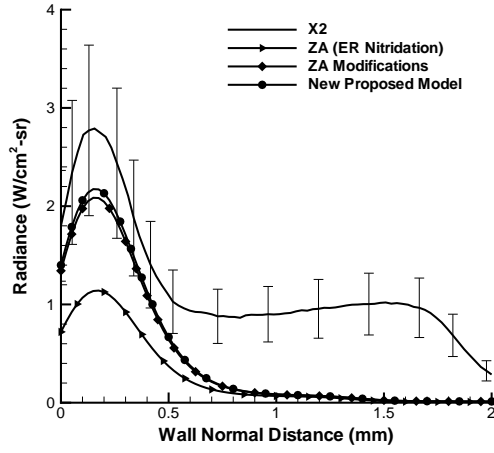
(a) $T_w = 2410\,\mathrm{K}$
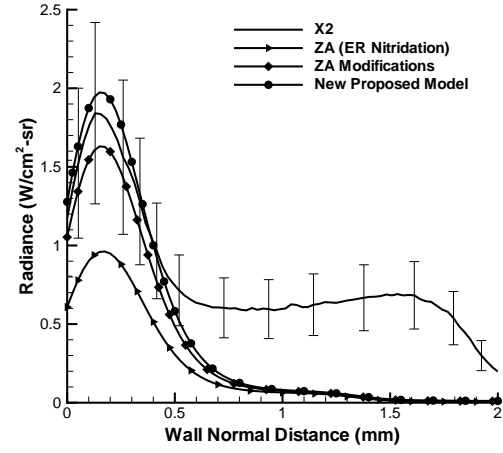
(b) $T_w = 2170\,\mathrm{K}$
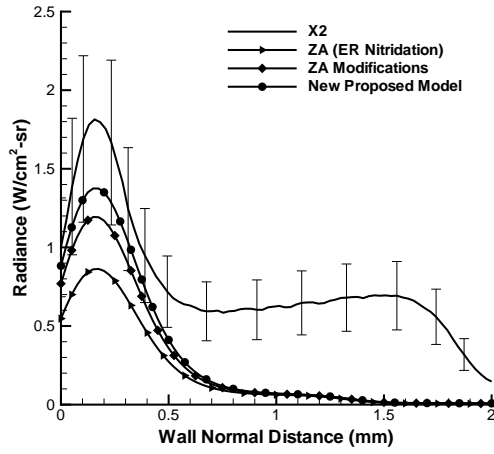
(c) $T_w = 1920\,\mathrm{K}$
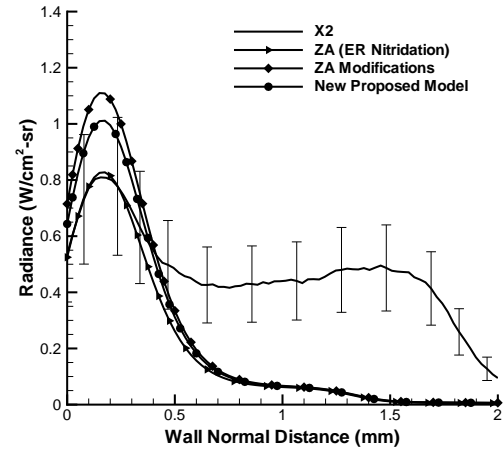
(d) $T_w = 1770\,\mathrm{K}$

Figure 65. Comparison of CN radiance values as a function of wall normal distance along the stagnation streamline for the lower four wall temperature cases from the X-2 experiments using the new proposed model.

Table 20. CN radiance error estimates at a wall normal distance of 0.15 mm with the new ablation model.

Surface Model	Absolute Error
$T_w = 2410$ K	
ZA (Johnston)	64%
ZA (ER Nitridation)	59%
ZA Modifications	25%
New Model	22%
$T_w = 2170$ K	
ZA (Johnston)	50%
ZA (ER Nitridation)	48%
ZA Modifications	11%
New Model	7%
$T_w = 1920$ K	
ZA (Johnston)	53%
ZA (ER Nitridation)	52%
ZA Modifications	34%
New Model	24%
$T_w = 1770$ K	
ZA (Johnston)	1%
ZA (ER Nitridation)	2%
ZA Modifications	37%
New Model	25%
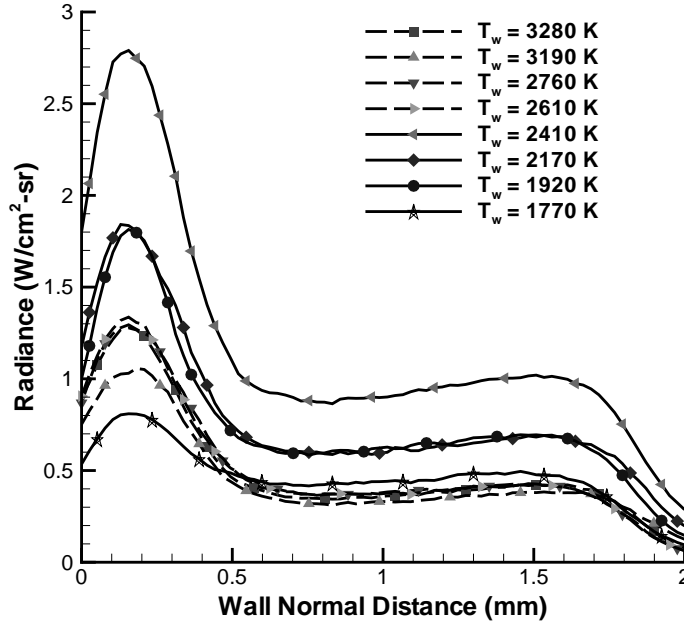
Figure 66. Comparison of experimental radiance values as a function of wall normal distance along the stagnation streamline for surface temperatures from the first and second experimental campaigns.

temperature cases all have similar radiance profiles except for the 3190 K case, which roughly has a 20% lower peak value compared to the other three cases.

The unexpected drop in measured radiances make it challenging to compare the experimental data to the numerical predictions. Each ablation model, including the proposed model developed in Section 5.5, displays monotonic behavior by predicting an increase in radiance with an increase in surface temperature as shown in Figure 67. The original Park ablation model is not shown because the predicted radiances were nearly twice as high as the modified Park ablation model. All predictions shown used the Johnston gas-phase chemistry model. It would be naive to make a fair comparison between the measurements and predictions because there is some phenomena occurring in the experiments that has yet to be quantified. Therefore, it would be illogical to conclude that there is good agreement at surface temperatures of 2760 K

159
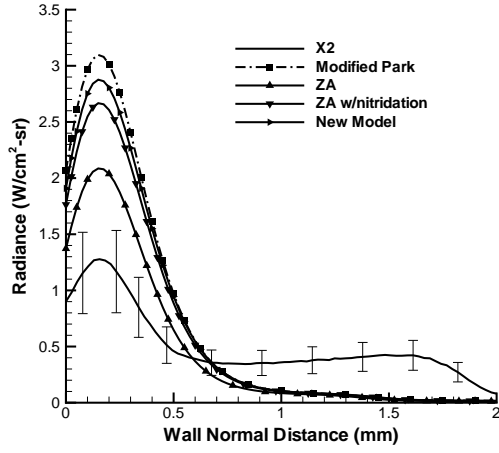
(a) $T_w = 3280\,\mathrm{K}$
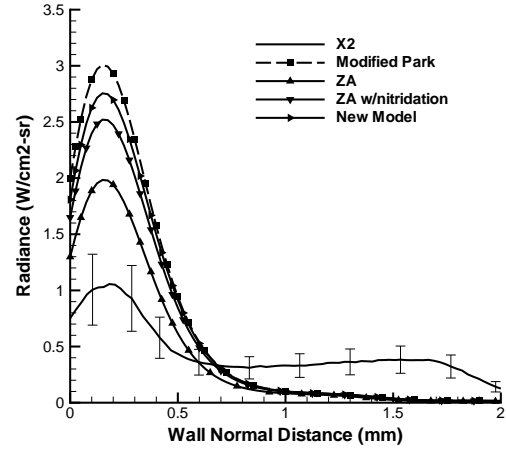
(b) $T_w = 3190\,\mathrm{K}$
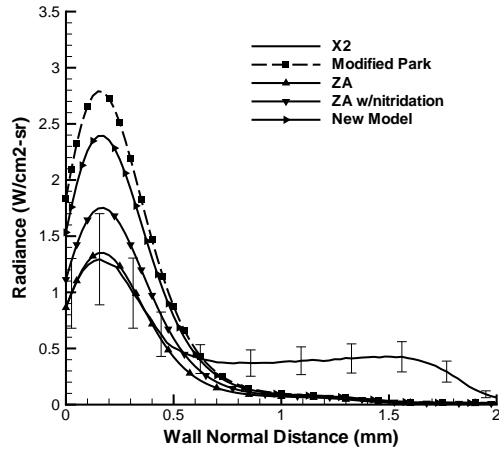
(c) $T_w = 2760\,\mathrm{K}$
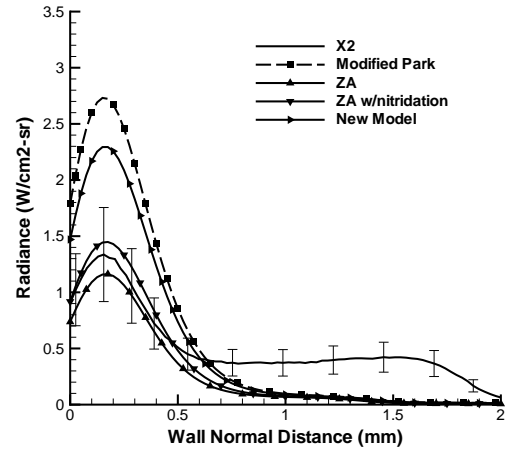
(d) $T_w = 2610\,\mathrm{K}$

Figure 67. Comparison of CN radiance values as a function of wall normal distance along the stagnation streamline for the four high wall temperature cases from the X-2 experiments.

and 2610 K using the ZA model with and without nitridation. A proper comparison is not possible, so the analysis is limited to the differences between the model predictions.

When comparing the predicted radiances, the new ablation model is consistently between the modified Park and ZA with nitridation models. The predicted results are as expected due to the ratios of CO_2, CO, and CN that are generated at the surface. The new model primarily has CN and CO production whereas the ZA model with nitridation has CO_2, CO, and CN production. The modified Park model also has CN and CO production but does not allow for C to recombine at the surface. Recalling the analyses from the previous chapters, these combinations of species yield the expected results in Figure 67.

An interesting discovery was found when analyzing the high speed video from each test case. For the cases with a surface temperature above 3000 K, there appear to be carbon particles spallating off of the surface. The particles appear after the flow has reached a "steady-state" and gradually become numerous with time. Figure 68 shows the difference in the high speed camera imagery at a surface temperature of 2610 K and 3280 K. At 3280 K, an immense amount of tiny carbon particles can be seen coming off the model surface. For ablating environments, both shock layer thermodynamics and composition may be altered by the presence of spalled particles. As was shown in the SEM images in Chapter II, the initial carbon model surface is amorphous with many defects.

It is postulated that the hot gases are occupying these defects and mechanically breaking down the bulk carbon. The effect of spallation could be a reason why the measured radiances were lower at the higher surface temperatures, which is a theory supported by the work of Raiche and Driver [101]. Raiche and Driver experimentally verified the presence of solid particles by measuring the optical attenuation of a laser

through an ablating arcjet flow [101]. Upon removal of the ablating model, the laser transmission reached normal levels. They also found that the attenuation increased quadratically with heating rate. Therefore, it is proposed that spallation is likely causing the reduction in CN emission intensities at the higher surface temperatures due to line-of-sight blockage effects. However, to-date, no direct measurements have been made to determine spalled particle size and/or velocity distributions.
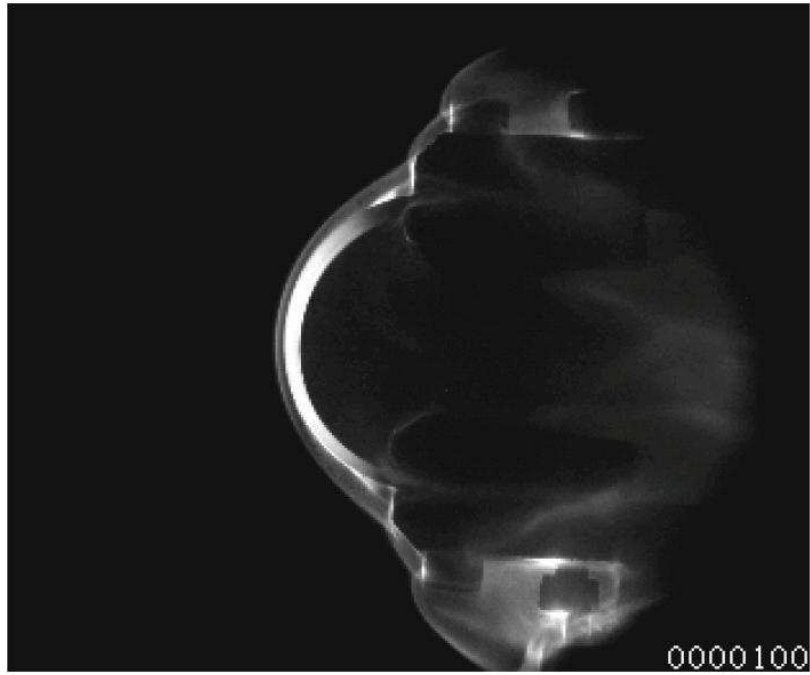
(a) $T_w = 2610$ K
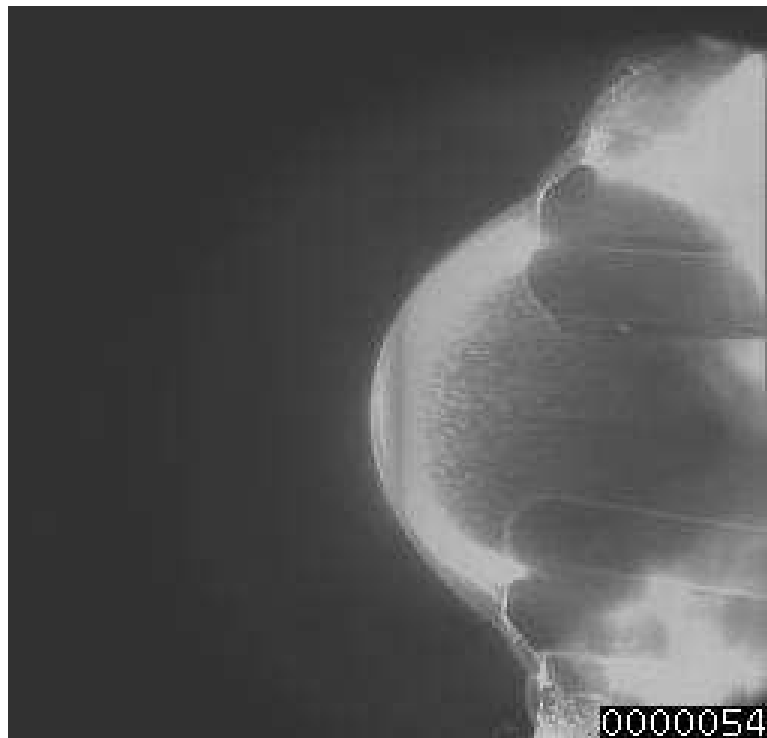
(b) $T_w = 3280$ K

Figure 68. Comparison of high speed camera images showing effect of spallation. These images have been enhanced to improve visibility.

VI. Conclusions

Despite the prominence of carbon-based materials for use in thermal protection systems, much uncertainty remains in predicting thermochemical ablation rates at high surface temperatures. To address this uncertainty, a series of experiments using pre-heated graphite models with surface temperatures up to 3280 K were conducted in the X-2 expansion tunnel at The University of Queensland. Calibrated shock-layer emission measurements in the wavelength region 353 to 391 nm were taken to observe the effect of surface temperature on radiation from the CN violet bands. Attempts were also made to observe emissions from the C_3 Swings and C_2 Swan bands, however, no measurable signal was found. Most of the analysis focused on a surface temperature range from 1770-2410 K because the higher surface temperature cases displayed non-monotonic behavior with ablative phenomena that current CFD codes cannot model.

Numerical simulations were performed using US3D with the Park and Zhluktov and Abe finite-rate surface kinetic models. The gas-phase chemistry model used legacy Park et al. [92, 93, 96, 97] rates and updated rates from Johnston et al. [46]. It was found that the Johnston rates mostly influenced the mass fluxes and concentrations of CO and CO_2 but did not significantly affect the CN radiation spectra. Results were also analyzed using a modified nitridation rate proposed by Suzuki et al. [115] in the Park ablation model, which significantly reduced the amount of CN formed at the surface. The simulation results were applied in NEQAIR to reproduce the experimental radiance profiles.

The ablation products were quite different between the surface kinetic models. For the oxidation mechanisms, the Park model only produced CO whereas the ZA model produced CO_2 and had CO recombining at the surface. The Park model includes a nitridation reaction with an efficiency that does not replicate experimental

164

results, including the results presented in this work. By reducing the Park nitridation efficiency, good agreement was obtained in comparing measured CN violet radiance values at a surface temperature of 2410 K. The ZA model did not show good agreement at this surface temperature, and it was first assumed to be due to a lack of a nitridation reaction.

As the surface temperature was decreased, the ZA model radiance predictions improved greatly. In fact, the measured near surface radiance at $T_w = 1770$ K was accurately predicted by the ZA model with the Johnston gas chemistry model. The two intermediate surface temperatures of 1920 and 2170 K had measured radiance profiles that were in between the predictions of the Park and ZA models. Logically, this led to the assumption that nitridation became a relevant surface reaction at wall temperatures above 1800 K.

Modifications to the ZA model were proposed based on experimental and theoretical results with the goal of improving the CN radiance predictions. Two approaches for modeling carbon nitridation were developed with rate parameters derived from experimental measurements and theory. One approach assumed that atomic nitrogen could react directly with the bulk carbon to form gaseous CN. The other approach followed a more traditional gas-surface interaction process and required atomic nitrogen to be in an adsorbed surface state before reacting with the bulk carbon. The experimental test conditions from which the rate parameters were deduced had relatively low wall temperatures as compared to those that may be experienced during a re-entry flight. Therefore, additional measurements at higher surface temperatures are needed to improve the nitridation rate parameters derived in this study.

The nitridation reaction should be included in any air-carbon system because it will have an effect on surface and radiative heating. Yet, its importance varies with surface temperature. It was concluded that a direct nitridation mechanism

165

has the most significant impact on predicted surface mass fluxes and species mass fractions. Direct nitridation was active between surface temperatures ranging between approximately 2000-4000 K, and the CN production rate dropped or approached zero outside of this range. The surface participating nitridation reaction was shown not to influence any of the mass fluxes or the composition of the boundary layer at the stagnation point.

The large differences between these nitridation mechanisms are due to many factors in combination. Under conditions where desorption rates are high, such as at high surface temperatures, surface coverage would be low. Hence, the surface participating nitridation reaction would be much less likely to occur compared to direct nitridation. Furthermore, direct nitridation would be uninhibited because the surface would be entirely empty. Then as the wall temperature cools, there is a competition between the adsorbed atomic oxygen and nitrogen sites. However, if the wall temperature cools too rapidly, it may result in the nitridation rate becoming inactive. There is a balance occurring between the active sites with adsorbed atomic nitrogen and wall temperature that will ultimately determine the nitridation rate. Note that there is nothing to prevent implementing both nitridation mechanisms into a kinetics model because both are plausible surface reaction processes. Direct nitridation was chosen for implementation into the new ablation model because it predicted substantial CN production at high surface temperatures that agreed with equilibrium ablation modeling.

Additionally, a sensitivity analysis of the ZA model was performed to determine which surface reactions had the most impact on CN radiance predictions. It was found that increasing the amount of CO formed at the surface increased CN concentrations. Examining the surface reaction fluxes showed that CO_2 was the dominant oxidation product, contrary to existing experimental evidence that measured primarily CO at

166

high surface temperatures. Additionally, an equilibrium air-carbon mixture indicated that a gas would be composed of only N_2 and CO within a temperature range of 1500-2500 K. A series of rate modifications were proposed, along with the initial recommendation to remove the $CO_2 + (s) \leftrightarrow CO + O(s)$ surface reaction, and then applied to the X-2 experiments. The CN radiance predictions improved by about 19-39% at surface temperatures of 1920, 2170, and 2410 K compared to the baseline ZA model. At a surface temperature of 1770 K, the modified ZA model over predicted the radiance by about 37%. Overall, the proposed modifications vastly improved the predictions and exhibited a sensitivity to a varying surface temperature, which was lacking with the baseline model.

The $CO_2 + (s) \leftrightarrow CO + O(s)$ reaction included in the baseline ZA model is a valid surface reaction, so instead of completely removing it, an attempt was made to take advantage of this reaction by controlling its efficiency at different temperatures. It was proposed to specify this reaction in the reverse order because it preferred to proceed in the backwards direction under these simulated conditions. Prior experimental work had also defined this reaction as $CO + O(s) \leftrightarrow CO_2 + (s)$. Therefore, if the forward rate for this reaction is quantified in future ablation experiments, it would be advantageous to have the numerical forward rate specified in the same manner for an apt comparison. The Arrhenius rate for the other oxidation reaction that produced CO, $O(s) + C(b) \leftrightarrow CO + (s)$, was also modified as part of the modeling effort. The developed ablation model that included these oxidation modifications, and those from the sensitivity analysis, further improved the CN radiation comparisons. The primary oxidation product became CO at the higher surface temperatures and then switched to CO_2 at the lower surface temperatures. All radiation predictions fell within the experimental error, and the error probability range dropped from 1-64% for the baseline ZA model to 7-25% for the new model.

167

The experimental results from the second campaign were not as anticipated because there was a significant drop in CN radiative intensities. It was speculated that the decrease in measured radiance was due to an attenuation of the optical signal caused by spalled carbon particles. Evidence from the high speed video supported this hypothesis, but it has yet to be quantified. Unfortunately, a comparison of the numerical predictions with the measured radiances was practically impossible. However, the predictions behaved as expected and showed an increase in CN radiance with an increase in surface temperature.

It also must be acknowledged that the error in the experimental data could come from multiple sources. An attempt to quantify this error was made by approximating an uncertainty range on the measured radiances. However, these were truly unprecedented experiments and some measurement techniques had to be adjusted due to unanticipated difficulties. These techniques will be improved upon as testing at these extreme conditions becomes more frequent.

Clearly, much work remains in understanding the surface kinetic mechanisms of an air-carbon system. The work presented in this dissertation has made a substantial leap forward in determining some of the proper mechanisms at relevant hypersonic re-entry conditions. The current state-of-the-art ablation models were shown to be inadequate to accurately predict species mass fluxes that correlated to experimental radiation measurements. Furthermore, the models did not even match experimental trends when surface temperatures were increased. The Park model was found to be too simple in that it only specified one-step kinetic processes and could not capture non-linear oxidation processes. The ZA model had competing surface kinetic processes and attempted to account for non-linear Arrhenius behavior. However, the ZA model had major deficiencies. A majority of the novel research presented in this dissertation was driven by improving the surface kinetic processes, starting with the ZA model as

a baseline, to better match experimental results. The new model that was developed has been shown to vastly improve the comparison with experimental results. The new model now follows the trend in the experimental data where the primary oxidation product appears to switch from CO_2 to CO as the surface temperature rises above approximately 1800 K. Moving forward with this research, it is recommended to use the new model for future carbon ablation simulations instead of either the Park or ZA models.

As research into carbon ablation proceeds, it would be constructive to consider the use of higher fidelity mass diffusion models because Fick's law typically provides conservative heating rate predictions at hypersonic re-entry conditions. Using Fick's law with a constant Lewis number does not strictly enforce that the sum of the mass diffusion fluxes is zero. There is a modified form of Fick's law that ensures total diffusion flux of zero, and this form has been shown to predict flowfield properties that are in good agreement with multi-component diffusion models. The current US3D code does not have a version with modified Fick's law implemented. Additionally, implementing the modified form of Fick's law would require a re-derivation of the surface mass balance equation for each gas species. With more time and computational resources, the incorporation of a higher fidelity diffusion model would be the next step in the research process.

It was shown that the $CO_2 + (s) \leftrightarrow CO + O(s)$ reaction had a significant effect on the resulting radiation predictions. At high surface temperatures (greater than 1800 K), CO is the primary oxidized species. At relatively low surface temperatures (less than 1800 K), CO_2 may be the primary oxidized species. Therefore, it is desired to have future carbon ablation experiments analyze the oxidation processes more closely to further quantify the newly developed ablation model.

Further investigation is warranted to understand why much more CN radiation

was measured in the shock layer than what was predicted by the simulations. It is recommended that the X-2 nozzle exit conditions be calculated as an axisymmetric simulation including nonequilibrium gas chemistry effects. The shock layer radiation discrepancies could be quantified with higher fidelity nozzle exit conditions. An initial understanding could be achieved by artificially adding more carbon to the freestream mass fractions until shock layer CN concentrations reach those observed in the X-2 experiments.

Lastly, future experiments need to quantify the influence of spallation on measured radiances. It is only speculation that spalled carbon particles are attenuating the optical path to the spectrometer camera, thereby reducing the CN violet radiative intensities. If discovered to be true, then a change in model material should be considered to lessen the chance for spallation to occur. For example, instead of using an amorphous graphite, a carbon fiber material may be more functional. A uniform grain structure may make it more resistant to breaking apart under extreme heating conditions.

The improved ablation modeling capability presented in this dissertation may one day aid in the development of innovative TPS design to ensure the survivability and lethality of high speed strike weapons or penetrating cruise missiles. Alternatively, these modeling capabilities may serve to mature heat shield materials for reusable space access vehicles. At a minimum, the methods used to characterize shock layer radiation can be implemented immediately into the IC for the purpose of identifying hostile threats. In that case, the fidelity of these methods could mean the difference between a successful interception or a Pearl Harbor type of event.

Bibliography

1. *JANAF Thermochemical Tables*. Second edition, National Bureau of Standards, Washington D.C., June 1971.

2. "Technology Horizons, A Vision for Air Force Science and Technology During 2010-2030". 15 May 2010. Volume 1, AF/ST-TR-10-01-PR.

3. "Air Force Science and Technology Plan". 3 Jun 2011. 2011-0354.

4. Ackleh, A. S., E. J. Allen, R. B. Hearfott, and P. Seshaiyer. *Classical and Modern Numerical Analysis: Theory, Methods and Practice*. Chapman and Hall/CRC Press, 2010.

5. Alkandry, H., I. D. Boyd, and A. Martin. "Comparison of Transport Properties Models for Flowfield Simulations of Ablative Heat Shields". *Journal of Thermophysics and Heat Transfer*, 28(4):569–582, 2014.

6. Anna, A., H. Alkandry, and I. D. Boyd. *Computational Modeling of Gas-Surface Interactions for High-Enthalpy Reacting Flows*. AIAA Paper 2013-0187, 2013.

7. Appleton, J. P. and K. N. C. Bray. "The Conservation Equations for a Non-Equilibrium Plasma". *Journal of Fluid Mechanics*, 20(4):659–672, 1964.

8. Baker, R. L. "Graphite Sublimation Chemistry Nonequilibrium Effects". *AIAA Journal*, 15(10):1391–1397, 1977.

9. Balat-Pichelin, M., J. M. Badie, R. Berjoan, and P. Boubert. "Recombination Coefficient of Atomic Oxygen on Ceramic Materials Under Earth Re-Entry Conditions by Optical Emission Spectroscopy". *Chemical Physics*, 291:181–194, 2003.

10. Balat-Pichelin, M., J. F. Robert, and J. L. Sans. "Emissivity Measurements on Carbon-Carbon Composites at High Temperature Under High Vacuum". *Applied Surface Science*, 253(2):778–783, 2006.

11. Barinov, A., O. B. Malcioglu, S. Fabris, T. Sun, L. Gregoratti, M. Dalmiglio, and M. Kiskinova. "Initial Stages of Oxidation on Graphitic Surfaces: Photoemission Study and Density Functional Theory Calculations". *The Journal of Physical Chemistry C*, 113:9009–9013, 2009.

12. Beerman, A. F., M. J. Lewis, R. P. Starkey, and B. Z. Cybyk. *Nonequilibrium Surface Interactions Ablation Modeling with the Fully Implicit Ablation and Thermal Response Program*. AIAA Paper 2008-1224, January 2008.

13. Beerman, A. F., M. J. Lewis, R. P. Starkey, and B. Z. Cybyk. "Significance of Nonequilibrium Surface Interactions in Stardust Return Capsule Ablation Modeling". *Journal of Thermophysics and Heat Transfer*, 23(3):425–432, July-September 2009.

14. Bianchi, D., F. Nasuti, and E. Martelli. "Navier-Stokes Simulations of Hypersonic Flows with Coupled Graphite Ablation". *Journal of Spacecraft and Rockets*, 47(4), July-August 2010.

15. Blottner, F. G. *Prediction of Electron Density in the Boundary Layer on Entry Vehicles with Ablation*. NASA SP-252, October 1970.

16. Blyholder, G., J. S. Binford, and H. Eyring. "A Kinetic Theory for the Oxidation of Carbonized Filaments". *Journal of Physical Chemistry*, 62:263–267, March 1958.

17. Blyholder, G. and H. Eyring. "Kinetics of Graphite Oxidation". *The Journal of Physical Chemistry*, 61:682–688, 1957.

18. Bose, D., T. White, J. A. Santos, J. Feldman, M. Mahzari, M. Olson, and B. Laub. *Initial Assessment of Mars Science Laboratory Heatshield Instrumentation and Flight Data*. AIAA Paper 2013-0908, 2013.

19. Bose, D., M. J. Wright, G. A. Raiche, D. Bogdanoff, and G. A. Allen. *Modeling and Experimental Validation of CN Radiation Behind a Strong Shock Wave*. AIAA Paper 2005-0768, 2005.

20. Brandis, A. M., C. O. Johnston, B. A. Cruden, and D. K. Prabhu. *Investigation of Nonequilibrium Radiation for Mars Entry*. AIAA Paper 2013-1055, 2013.

21. Brandis, A. M., R. G. Morgan, T. J. McIntyre, and P. A. Jacobs. "Nonequilibrium Radiation Intensity Measurements in Simulated Titan Atmospheres". *Journal of Thermophysics and Heat Transfer*, 24(2):291–300, April 2010.

22. Candler, G. V. *The Computation of Weakly Ionized Hypersonic Flows in Thermo-Chemical Nonequilibrium*. Ph.D. thesis, Stanford University, June 1988.

23. Candler, G. V. *Nonequilibrium Process in Hypervelocity Flow: An Analysis of Carbon Ablation Models*. AIAA Paper 2012-0724, 2012.

24. Chen, Y. and T. Gokcen. "Effect of Nonequilibrium Surface Thermochemistry in Simulation of Carbon-Based Ablators". *Journal of Spacecraft and Rockets*, 50(5):917–926, September-October 2013.

25. Chen, Y. and F. S. Milos. *Finite-Rate Ablation Boundary Conditions for a Carbon-Phenolic Heat-Shield*. AIAA Paper 2004-2270, 2004.

26. Chen, Y. K. and F. S. Milos. "Ablation and Thermal Analysis Program for Spacecraft Heatshield Analysis". *Journal of Spacecraft and Rockets*, 36(3):475–483, 1999.

27. Chen, Y. K. and F. S. Milos. "Navier-Stokes Solutions with Finite Rate Ablation for Planetary Mission Earth Reentries". *Journal of Spacecraft and Rockets*, 42(6):961–970, 2005.

28. Driver, D. M. and M. MacLean. *Improved Predictions of PICA Recession in Arc Jet Shear Tests*. AIAA Paper 2011-141, 2011.

29. Eichmann, T. N. *Radiation Measurements in a Simulated Mars Atmosphere*. Ph.D. thesis, The University of Queensland, 2012.

30. Glass, D. E., R. Dirling, H. Croop, T. J. Fry, and G. J. Frank. *Materials Development for Hypersonic Flight Vehicles*. AIAA Paper 2006-8122, 2006.

31. Gnoffo, P. A., R. N. Gupta, and J. L. Shinn. *Conservation Equations and Physical Models for Hypersonic Air Flows in Thermal and Chemical Nonequilibrium*. NASA-TP 2867, NASA Langley, Hampton, Virginia, 1989.

32. Gnoffo, P. A., K. J. Weilmuenster, H. H. Hamilton, D. R. Olynick, and E. V. Venkatapathy. "Computational Aerothermodynamic Design Issues for Hypersonic Vehicles". *Journal of Spacecraft and Rockets*, 36(1):21–43, 1999.

33. Goldstein, H. W. "The Reaction of Active Nitrogen with Graphite". *The Journal of Physical Chemistry*, 68(1):39–42, January 1964.

34. Gordon, S. and B. J. McBride. *Computer Program for Calculation of Complex Chemical Equilibrium Compositions and Applications*. Reference Publication 1311, NASA, October 1994.

35. Gosse, R. and G. Candler. *Diffusion Flux Modeling: Application to Direct Entry Problems*. AIAA Paper 2005-389, 2005.

36. Gosse, R., S. Gogineni, and S. Roy. *Graphite Ablation Experiments in the LH-MEL Laser Facility*. AIAA Paper 2012-2745, 2012.

37. Greaves, J. C. and J. W. Linnett. "Recombination of Atoms at Surfaces, Part 6 - Recombination of Oxygen Atoms on Silica from 20°C to 600°C". *Transitions of the Faraday Society*, 55:1355–1361, 1959.

38. Greendyke, R. and L. C. Hartung. *A Convective and Radiative Heat Transfer Analysis for the FIRE II Forebody*. AIAA Paper 93-3194, July 1993.

39. Grinstead, J. H., M. C. Wilder, M. J. Wright, D. W. Bogdanoff, G. A. Allen, K. Dang, and M. J. Forrest. *Shock Radiation Measurements for Mars Aerocapture Radiative Heating Analysis*. AIAA Paper 2008-1272, 2008.

40. Gupta, R. N., J. M. Yos, R. A. Thompson, and K. P. Lee. *A Review of Reaction Rates and Thermodynamic and Transport Properties for an 11-Species Air Model for Chemical and Thermal Nonequilibrium Calculations to 30,000 K*. Reference Publication 1232, NASA, 1990.

41. Hammerling, P., J. D. Teare, and B. Kivel. "Theory of Radiation from Luminous Shock Waves in Nitrogen". *Physics of Fluids*, 2:422–426, July-August 1959.

42. Hartung, L. C. *Nonequilibrium Radiative Heating Prediction Method for Aeroassist Flowfields with Coupling to Flowfield Solvers*. Ph.D. thesis, North Carolina State University, Raleigh, NC, 1991.

43. Hash, D., J. Olejniczak, M. Wright, D. P. M. Pulsonetti, B. Hollis, P. Gnoffo, M. Barnhardt, I. Nompelis, and G. Candler. *FIRE II Calculations for Hypersonic Nonequilibrium Aerothermodynamics Code Verification: DPLR, LAURA, and US3D*. AIAA Paper 2007-605, 2007.

44. Havstad, M. A. and R. M. Ferencz. "Comparison of Surface Chemical Kinetic Models for Ablative Reentry of Graphite". *Journal of Thermophysics and Heat Transfer*, 16(4), October-December 2002.

45. Johnston, C. O. *Nonequilibrium Shock-Layer Radiative Heating for Earth and Titan Entry*. Ph.D. thesis, Virginia Polytechnic Institute and State University, Virginia, 2006.

46. Johnston, C. O., A. M. Brandis, and K. Sutton. *Shock Layer Radiation Modeling and Uncertainty for Mars Entry*. AIAA Paper 2012-2866, 2012.

47. Jones, B. and C. J. Nachtsheim. "A Class of Three-Level Designs for Definitive Screening in the Presence of Second-Order Effects". *Journal of Quality Technology*, 43:1–15, 2011.

48. Keenan, J. A. and G. V. Candler. *Simulation of Graphite Sublimation and Oxidation under Re-entry Conditions*. AIAA Paper 94-2083, 1994.

49. Kontinos, D. and M. Stackpoole. *Post-Flight Analysis of the Stardust Sample Return Capsule Earth Entry*. AIAA Paper 2008-1197, 2008.

50. Kovalev, V. L., O. N. Suslov, and G. A. Tirskiy. "Phenomenological Theory for Heterogeneous Recombination of Partially Dissociated Air on High-Temperature Surfaces". M. Capitelli (editor), *Molecular Physics and Hypersonic Flows*, volume 482 of *NATO ASI Series, Series C: Mathematical and Physical Sciences*, 193–202. Kluwer Academic Publishers, Boston, MA, 1996.

51. Langmuir, I. "The Adsorption of Gases on Plane Surfaces of Glass, Mica and Platinum". *Journal of the American Chemical Society*, 40(9):1361–1403, September 1918.

52. Laux, C. O. *Optical Diagnostics and Radiative Emission of Air Plasmas*. Ph.D. thesis, Stanford University, 1993.

53. Laux, C. O., M. Winter, J. Merrifield, A. Smith, and P. Tran. *Influence of Ablation Products on the Radiation at the Surface of a Blunt Hypersonic Vehicle at 10 km/s*. AIAA Paper 2009-3925, 2009.

54. Lee, J. H. *Basic Governing Equations for the Flight Regimes of Aeroassited Orbital Transfer Vehicles*. AIAA Paper 84-1729, 1984.

55. Lehman, A., N. O'Rourke, L. Hatcher, and E. J. Stepanski. *JMP® for Basic Univariate and Multivariate Statistics: A Step-by-Step Guide*. SAS Institute Inc., Cary, NC, 2005.

56. Lewis, S. W., R. G. Morgan, and T. J. McIntyre. "Shock Layer Radiation Measurements with Subliming Graphite Models in an Expansion Tunnel". *Proceedings of 6th International Workshop on Radiation of High Temperature Gases in Atmospheric Entry*. European Space Agency, St. Andrews, UK, November 2014.

57. Lewis, S. W., R. G. Morgan, T. J. McIntyre, C. R. Alba, and R. G. Greendyke. "Expansion Tunnel Experiments of Earth Re-entry Flow with Surface Ablation". *Journal of Spacecraft and Rockets*. Accepted for publication.

58. Liu, G. N. K. *High Temperature Oxidation of Graphite by a Dissociated Oxygen Beam*. Technical Report AD-799949, Massachusetts Institute of Technology, August 1973.

59. Lu, F. and D. Marren. "Advanced Hypersonic Test Facilities". *Progress in Astronautics and Aeronautics*, 2002. AIAA.

60. Lutz, A., J. Meyers, W. Owens, S. Smith, and D. G. Fletcher. *Experimental Analysis of Carbon Nitridation and Oxidation Efficiency with Laser-Induced Fluorescence*. AIAA Paper 2013-0924, 2013.

61. Ma, Y., A. S. Foster, A. V. Krasheninnikov, and R. M. Nieminen. "Nitrogen in graphite and carbon nanotubes: Magnetism and mobility". *Phys. Rev. B*, 72:205416, Nov 2005.

62. Maahs, H. G. *Oxidation of Carbon at High Temperatures: Reaction-Rate Control or Transport Control*. NASA TN D-6310, June 1971.

63. MacLean, M. *An Equilibrium Ablation Boundary Condition for the Data-Parallel Line-Relaxation Code*. AIAA Paper 2013-0304, 2013.

64. MacLean, M., J. Marschall, and D. M. Driver. *Finite-Rate Surface Chemistry Model, II: Coupling to Viscous Navier-Stokes Code*. AIAA Paper 2011-3784, 2011.

65. Marrone, P. V. and C. E. Treanor. "Chemical Relaxation with Preferential Dissociation from Excited Vibrational Levels". *Physics of Fluids*, 6(9):1215–1221, 1963.

66. Marschall, J. *Experimental Determination of Oxygen and Nitrogen Recombination Coefficients at Elevated Temperature Using Laser-Induced Fluorescence.* AIAA Paper 97-3879, 1997.

67. Marschall, J. and M. MacLean. *Finite-Rate Surface Chemistry Model, I: Formulation and Reaction System Examples.* AIAA Paper 2011-3783, 2011.

68. Martin, A. and I. D. Boyd. *CFD Implementation of a novel carbon-phenolic-in-ar chemistry model for atmospheric re-entry.* AIAA Paper 2011-143, 2011.

69. Martin, C. L. *Coupled Radiation-Gasdynamic Solution Method for Hypersonic Shock Layers in Thermochemical Nonequilibrium.* Ph.D. thesis, Air Force Institute of Technology, Wright-Patterson Air Force Base, Ohio, 2011.

70. McBride, B. J., M. J. Zehe, and S. Gordon. *NASA Glenn Coefficients for Calculating Thermodynamic Properties of Individual Species.* NASA-TP 2002-211556, September 2002.

71. McIntyre, T. J., T. N. Eichmann, C. Jacobs, D. Potter, M. McGilvray, P. Jacobs, and R. Morgan. "Shock Tube and Expansion Tunnel Measurements of High Temperature Radiating Flows". *Proceedings of the 4th International Workshop of Radiation of High Temperature Gases in Atmospheric Entry.* Lausanne, Switzerland, October 2010.

72. Millikan, R. C. and D. R. White. "Systematics of Vibrational Relaxation". *J. of Chem. Phys.*, 39:3209–3213, 1963.

73. Milos, F. S. and Y. K. Chen. *Ablation Predictions for Carbonaceous Materials Using CEA and JANNAF-Based Species Thermodynamics.* AIAA Paper 2011-3123, 2011.

74. Morgan, R. G. *Radiation Measurements in Simulated Ablation Layers.* AOARD -09-4144, 2010.

75. Morgan, R. G., T. J. McIntyre, D. R. Buttsworth, P. A. Jacobs, D. F. Potter, A. M. Brandis, R. J. Gollan, C. M. Jacobs, B. R. Capra, M. McGilvray, and T. Eichmann. *Impulse facilities for the simulation of hypersonic radiating flows.* AIAA Paper 2008-4270, 2008.

76. Moyer, C. B. and R. A. Rindal. *Finite Difference Solution for the In-Depth Response of Charring Materials Considering Surface Chemical and Energy Balances.* NASA CR-1061, 1968.

77. Murray, V. J., B. C. Marshall, P. J. Woodburn, and T. K. Minton. "Inelastic and Reactive Scattering Dynamics of Hyperthermal O and O on Hot Vitreous Carbon Surfaces". *The Journal of Physical Chemistry C*. Accepted for web publication on March 26, 2015.

78. Nagle, J. and R. F. Strickland-Constable. "Oxidation of Carbon Between 1000-2000°C". *Proceedings of the Fifth Conference on Carbon*, 1:154–164, 1962.

79. Nasuti, F., M. Barbato, and C. Bruno. "Material-Dependent Catalytic Recombination Modeling for Hypersonic Flows". *Journal of Thermophysics and Heat Transfer*, 10(1):131–136, January-March 1996.

80. Nompelis, I., T. W. Drayna, and G. V. Candler. *Development of a Hybrid Unstructured Implicit Solver for the Simulation of Reacting Flows Over Complex Geometries*. AIAA Paper 2004-2227, 2004.

81. Nompelis, I., T. W. Drayna, and G. V. Candler. *A Parallel Unstructured Implicit Solver for Hypersonic Reacting Flow Simulation*. AIAA Paper 2005-4867, June 2005.

82. Olander, D. R., R. H. Jones, J. A. Schwarz, and W. J. Siekhaus. "Reactions of Modulated Molecular Beams with Pyrolytic Graphite. II. Oxidation of the Prism Plane". *The Journal of Chemical Physics*, 57(1):421–433, 1972.

83. Olander, D. R., W. Siekhaus, R. Jones, and J. A. Schwarz. "Reactions of Modulated Molecular Beams with Pyrolytic Graphite. I. Oxidation of the Basal Plane". *The Journal of Chemical Physics*, 57(1):408–420, 1972.

84. Olejniczak, J. and G. V. Candler. "Vibrational Energy Conservation with Vibration-Dissociation Coupling: General Theory and Numerical Studies". *Physics of Fluids*, 7:1764–1776, 1995.

85. Ong, Jr., J. N. "On the Kinetics of Oxidation of Graphite". *Carbon*, 2(3):281–297, December 1964.

86. Pagoda, C. J. and D. H. Hecht. *Development and Fabrication of the Falcon HTV-2 External Thermal Protection System*. Paper, AIAA Missile Sciences Conference, October 2008.

87. Palmer, G., D. Prabhu, A. Brandis, and T. J. McIntyre. *Numerical Simulation of Radiation Measurements taken in the X2 Facility for Mars and Titan Gas Mixtures*. AIAA Paper 2011-3768, 2011.

88. Palmer, G., D. Prabhu, and B. A. Cruden. *Uncertainty Determination for Aeroheating in Uranus and Saturn Probe Entries by the Monte Carlo Method*. AIAA Paper 2013-2776, 2013.

89. Park, C. "Effects of Atomic Oxygen on Graphite Ablation". *AIAA Journal*, 14(11):1640–1642, 1976.

90. Park, C. "Stagnation-Point Ablation of Carbonaceous Flat Disks - Part I: Theory". *AIAA Journal*, 21(11):1588–1594, 1983.

91. Park, C. "Assessment of Two-Temperature Kinetic Model for Ionizing Air". *Journal of Thermophysics and Heat Transfer*, 3(3):233–244, July 1989.

92. Park, C. *Nonequilibrium Hypersonic Aerothermodynamics*. John Wiley and Sons, Inc., New York, 1990.

93. Park, C. "Review of Chemical Kinetic Problems of Future NASA Missions, I: Earth Entries". *Journal of Thermophysics and Heat Transfer*, 7(3):385–398, 1993.

94. Park, C. and D. W. Bogdanoff. *Shock Tube Measurement of Coefficient of Reaction of Nitrogen Atoms with Solid Carbon: Preliminary Results*. AIAA Paper 2003-158, 2003.

95. Park, C. and D. W. Bogdanoff. "Shock-Tube Measurement of Nitridation Coefficient of Solid Carbon". *Journal of Thermophysics and Heat Transfer*, 20(3), July-September 2006.

96. Park, C., J. T. Howe, and R. L. Jaffe. "Review of Chemical Kinetic Problems of Future NASA Missions, II: Mars Entries". *Journal of Thermophysics and Heat Transfer*, 8(1):9–23, 1994.

97. Park, C., R. L. Jaffe, and H. Partridge. *Chemical-Kinetic Paramters of Hyperbolic Earth Entry*. AIAA Paper 00-0210, 2000.

98. Park, C. and M. E. Tauber. *Heatshielding Problems of Planetary Entry, A Review*. AIAA Paper 99-3415, 1999.

99. Poovathingal, S. and T. E. Schwartzentruber. *Computational Chemistry Modelling of the Oxidation of Highly Oriented Pyrolytic Graphite*. AIAA Paper 2012-3099, 2012.

100. Poovathingal, S., T. E. Schwartzentruber, V. Murray, and T. K. Minton. *Molecular Simulations of Surface Ablation Using Reaction Probabilities From Molecular Beam Experiments and Realistic Microstructure*. AIAA Paper 2015-1449, 2015.

101. Raiche, G. A. and D. M. Driver. *Shock Layer Optical Attenuation and Emission Spectroscopy Measurements During Arc Jet Testing with Ablating Models*. AIAA Paper 2004-825, 2004.

102. Rosner, D. E. and H. D. Allendorf. "High-Temperature Kinetics of Graphite Oxidation by Dissociated Oxygen". *AIAA Journal*, 3(8):1522–1523, 1965.

103. Rosner, D. E. and H. D. Allendorf. "Comparative Studies of the Attack of Pyrolytic and Isotropic Graphite by Atomic and Molecular Oxygen at High Temperatures". *AIAA Journal*, 6(4):650–654, 1968.

104. SAS Institute Inc., Cary, NC. *JMP$^{®}$, Version 10*, 1989-2007.

105. Scala, S. M. *The Ablation of Graphite in Dissociated Air, Part I: Theory*. Technical Information Series R62SD72, Missile and Space Division, General Electric, September 1962.

106. Scala, S. M. and L. M. Gilbert. "Sublimation of Graphite at Hypersonic Speeds". *AIAA Journal*, 3(9):1635–1644, 1965.

107. Scalabrin, L. C. *Numerical Simulation of Weakly Ionized Hypersonic Flow over Reentry Capsules*. Ph.D. thesis, The University of Michigan, 2007.

108. Shang, J. S. and S. T. Surzhikov. "Nonequilibrium radiative hypersonic flow simulation". *Progress in Aerospace Sciences*, (53):46–65, 2012.

109. Sharma, S. P., W. M. Huo, and C. Park. *The Rate Parameters for Coupled Vibration-Dissociation in a Generalized SSH Approximation*. AIAA Paper 88-2174, 1988.

110. Sorescu, D. C., K. D. Jordan, and P. Avouris. "Theoretical Study of Oxygen Adsorption on Graphite and the (8,0) Single-walled Carbon Nanotube". *Journal of Physical Chemistry B*, 105:11227–11232, 2001.

111. Spokes, G. N. and S. W. Benson. "Oxidation of a Thin Film of a Carbonaceous Char at Pressures Below 10^{-4} Torr". H. Saltsburg, J. N. Smith, Jr., and M. Rogers (editors), *Fundamentals of Gas-Surface Interactions*, 318–328. Academic Press, New York, 1967.

112. Stackpoole, M., S. Sepka, I. Cozmuta, and D. Kontinos. *Post-Flight Evaluation of Stardust Sample Return Capsule Forebody Heatshield Material*. AIAA Paper 2008-1202, 2008.

113. Stewart, D. A. *Surface Catalysis and Characterization of Proposed Candidate TPS for Access-to-Space Vehicles*. NASA-TM 12206, July 1997.

114. Suzuki, T., K. Fujita, K. Ando, and T. Sakai. "Experimental Study of Graphite Ablation in Nitrogen Flow". *Journal of Thermophysics and Heat Transfer*, 22(3):382–389, 2008.

115. Suzuki, T., K. Fujita, and T. Sakai. *Graphite Nitridation in Lower Surface Temperature Regime*. AIAA Paper 2009-260, 2009.

116. Suzuki, T., K. Fujita, and T. Sakai. "Graphite Nitridation in Lower Surface Temperature Regime". *Journal of Thermophysics and Heat Transfer*, 24(1):212–215, 2010.

117. Treanor, C. E. and P. V. Marrone. "The Effect of Dissociation on the Rate of Vibrational Relaxation". *Physics of Fluids*, 5(8):1022–1026, 1962.

118. Vancrayenest, B. and D. G. Flectcher. *Emission Spectroscopy Survey of Graphite Ablation in the VKI Plasmatron*. AIAA Paper 2006-2907, 2006.

119. Vastola, F. J., P. L. Walker, Jr., and J. P. Wightman. "The Reaction Between Carbon and the Products of Hydrogen, Oxygen and Water Microwave Discharges". *Carbon*, 1:11–16, 1963.

120. Vincenti, W. G. and C. H. Kruger. *Introduction to Physical Gas Dynamics*. Krieger Publishing Company, Florida, 1965.

121. Walker, S. H. and F. Rodgers. *Falcon Hypersonic Technology Overview*. AIAA Paper 2005-3253, 2005.

122. Walker, S. H., J. Sherk, D. Shell, R. Schena, J. F. Bergmann, and J. Gladbach. *The DARPA/AF Falcon Program: The Hypersonic Technology Vehicle 2 (HTV-2) Flight Demonstration Phase*. AIAA Paper 2008-2539, 2008.

123. Walker, Jr., P. L., F. J. Vastola, and P. J. Hart. "Oxygen-18 Tracer Studies on the Carbon-Oxygen Reaction". H. Saltsburg, J. N. Smith, Jr., and M. Rogers (editors), *Fundamentals of Gas-Surface Interactions*, 307–317. Academic Press, New York, 1967.

124. Walls, J. R. and R. F. Strickland-Constable. "Oxidation of Carbon Between 1000-2400°C". *Carbon*, 1:333–338, 1964.

125. Whiting, E. E., C. Park, Y. Liu, J. O. Arnold, and J. A. Paterson. *NEQAIR96, Nonequilibrium and Equilibrium Radiative Transport and Spectra Program: User's Manual*. NASA RP 1389, December 1996.

126. Wright, M. J., D. Bose, G. E. Palmer, and E. Levin. "Recommended Collision Integrals for Transport Property Computations, Part 1: Air Species". *AIAA Journal*, 43(12):2558–2564, December 2005.

127. Wright, M. J., G. V. Candler, and D. Bose. *A Data-Parallel Line-Relaxation Method for Navier-Stokes Equations*. AIAA Paper 97-2046, 1997.

128. Wright, M. J., G. V. Candler, and D. Bose. "Data-Parallel Line Relaxation Method for the Navier-Stokes Equations". *AIAA Journal*, 36(9), September 1998.

129. Wright, M. J., M. A. Loomis, and P. E. Papadopoulos. "Aerothermal Analysis of the Project Fire II Afterbody Flow". *Journal of Thermophysics and Heat Transfer*, 17(2):240–249, 2003.

130. Wright, M. J., J. Olejniczak, L. Walpot, E. Raynaud, T. Magin, L. Caillaut, and B. R. Hollis. *A Code Calibration Study for Huygens Entry Aeroheating*. AIAA Paper 2006-0382, June 2006.

131. Zander, F. *Hot Wall Testing in Hypersonic Impulse Facilities*. Ph.D. thesis, School of Mechanical and Mining Engineering, The University of Queensland, 2013.

132. Zander, F., R. G. Morgan, U. Sheikh, D. R. Buttsworth, and P. R. Teakle. *Hot Wall Testing Methodology for Impluse Facilities*. AIAA Paper 2012-5953, 2012.

133. Zander, F., R. G. Morgan, U. Sheikh, D. R. Buttsworth, and P. R. Teakle. "Hot-Wall Reentry Testing in Hypersonic Impluse Facilities". *AIAA Journal*, 51(2):476–484, February 2013.

134. Zhang, L., D. A. Pejakovic, B. Geng, and J. Marschall. "Surface modification of highly oriented pyrolytic graphite by reaction with atomic nitrogen at high temperatures". *Applied Surface Science*, 257:5647–5656, 2011.

135. Zhang, L., D. A. Pejakovic, J. Marschall, M. Dougherty, and D. G. Fletcher. "Laboratory Investigation of the Active Nitridation of Graphite by Atomic Nitrogen". *Journal of Thermophysics and Heat Transfer*, 26(1):10–21, January-March 2012.

136. Zhluktov, S. V. and T. Abe. "Viscous Shock-Layer Simulation of Airflow past Ablating Blunt Body with Carbon Surface". *Journal of Thermophysics and Heat Transfer*, 13(1), January-March 1999.

Vita

Captain Christopher Alba was born in West Allis, Wisconsin. After graduating in the top 6% of his class from Whitnall High School in 2001, he studied Aerospace Engineering at the University of Minnesota. He graduated with distinction with a Bachelor of Science degree in Aerospace Engineering and Mechanics in May 2006. At the same time, he commissioned into the United States Air Force as a distinguished graduate through the Reserve Officer Training Corps, Detachment 415, at the University of Minnesota.

Captain Alba was selected for an educational delay opportunity and earned his Master's of Science degree in Aerospace Engineering and Mechanics from the University of Minnesota in May 2008. His first active duty assignment was to the Air Vehicles Directorate in the Air Force Research Laboratory at Wright-Patterson, AFB OH. In August 2012, he entered the Aeronautical Engineering PhD program in the School of Engineering and Management, Air Force Institute of Technology.

REPORT DOCUMENTATION PAGE

Form Approved
OMB No. 0704–0188

1. REPORT DATE *(DD–MM–YYYY)*	2. REPORT TYPE	3. DATES COVERED *(From — To)*
17–09–2015	Dissertation	Oct 2012 — Sep 2015

4. TITLE AND SUBTITLE

A Nonequilibrium Finite-Rate Carbon Ablation Model for Radiating Earth Re-entry Flows

5a. CONTRACT NUMBER

5b. GRANT NUMBER

5c. PROGRAM ELEMENT NUMBER

6. AUTHOR(S)

Alba, Christopher, R., Captain, USAF

5d. PROJECT NUMBER

5e. TASK NUMBER

5f. WORK UNIT NUMBER

7. PERFORMING ORGANIZATION NAME(S) AND ADDRESS(ES)

Air Force Institute of Technology
Graduate School of Engineering and Management (AFIT/EN)
2950 Hobson Way
WPAFB OH 45433-8865

8. PERFORMING ORGANIZATION REPORT NUMBER

AFIT-ENY-DS-15-S-053

9. SPONSORING / MONITORING AGENCY NAME(S) AND ADDRESS(ES)

Air Force Office of Scientific Research
875 N. Randolph Street Suite 325, Room 3112
Arlington, Virginia 22203
Dr. John D. Schmisseur
(703) 696-6962; John.Schmisseur@afosr.af.mil

10. SPONSOR/MONITOR'S ACRONYM(S)

AFOSR

11. SPONSOR/MONITOR'S REPORT NUMBER(S)

N/A

12. DISTRIBUTION / AVAILABILITY STATEMENT

Distribution Statement A. Approved for Public Release; Distribution Unlimited

13. SUPPLEMENTARY NOTES

This material is declared a work of the U.S. Government and is not subject to copyright protection in the United States.

14. ABSTRACT

Vehicles entering planetary atmospheres at high speed require an ablative heat shield in order to withstand the high thermal energy flux to the body. Numerical simulations were conducted to investigate the influence of carbon ablation on shock layer radiation. Data collected from experiments performed in the X-2 expansion tunnel at the University of Queensland was used to compare to the simulations. The model was made of isomolded graphite and was tested in 8.5 km/s Earth entry flow. The model surface was heated within a temperature range of 1770-3280 K. The radiation emitted from the CN violet bands was measured by ultraviolet spectrometry in a spectral range from 353-391 nm. This research develops a novel finite-rate surface kinetic model for determining the chemical state of an ablating boundary layer. The ablative gas species predicted by this new model improves agreement with experimental measurements than predictions provided by legacy ablation models, and represents a significant improvement in current modeling capabilities for hypersonic nonequilibrium ablating re-entry flows.

15. SUBJECT TERMS

Hypersonics, Re-entry, Ablation, Radiation, Emission Spectroscopy, Nonequilibrium Aerodynamics

16. SECURITY CLASSIFICATION OF:			17. LIMITATION OF ABSTRACT	18. NUMBER OF PAGES	19a. NAME OF RESPONSIBLE PERSON
a. REPORT	b. ABSTRACT	c. THIS PAGE			Dr. Robert B. Greendyke, AFIT/ENY
U	U	U	UU	204	19b. TELEPHONE NUMBER *(include area code)* (937) 255-3636 x4567 robert.greendyke@afit.edu

Standard Form 298 (Rev. 8–98)
Prescribed by ANSI Std. Z39.18